Nature of serration behavior in high-Mn austenitic steel

2021

SUK YOUNG HWANG

Table of contents

Chapter 1   Background and objective

1.1 High-Mn austenitic steel

Over several decades, high-Mn austenitic steels have been the most promising materials for structural applications in the automobile industry field because of their outstanding mechanical properties combining both high strength and large ductility, as illustrated in **Figure 1.1**.   As the high-Mn austenitic steels are deformed, deformation twinning is activated as an extra deformation mechanism beside dislocation glide.   It has been known that relevant parameter for the deformation twinning is stacking fault energy (SFE), and the deformation twinning is prevalent within low SFE ranging from 18 to 40 mJ/m^2, which can be attained by the addition of high Mn contents (generally 18 to 31 wt.%) [1].   When the deformation twinning is activated in the material having the low SFE, the deformation twins subdivide the grains and act as obstacles for mobile dislocations.   As a result, the grain is significantly hardened and plastic instability is postponed, leading to large ductility as well as high strength.   Such a phenomenon was known as twinning induced plasticity (TWIP) effect or dynamic Hall-Petch effect [2–6], and it is schematically illustrated in **Figure 1.2**.
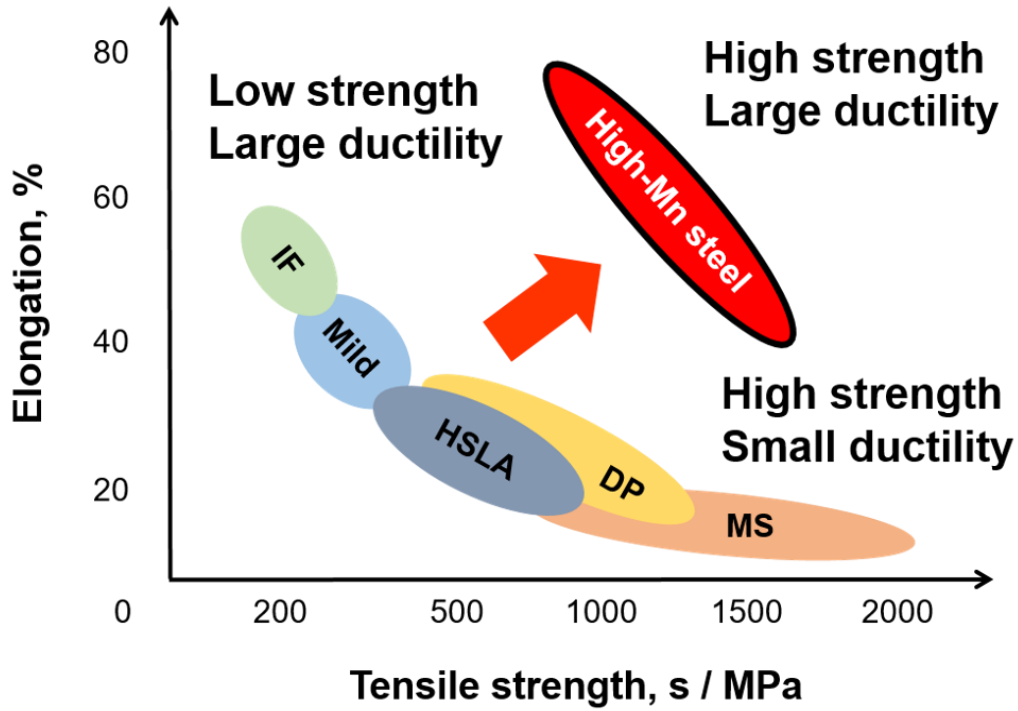
Fig. 1.1 Schematic illustration showing the tensile properties of various steels. High-Mn steels possess both high strength and large ductility.
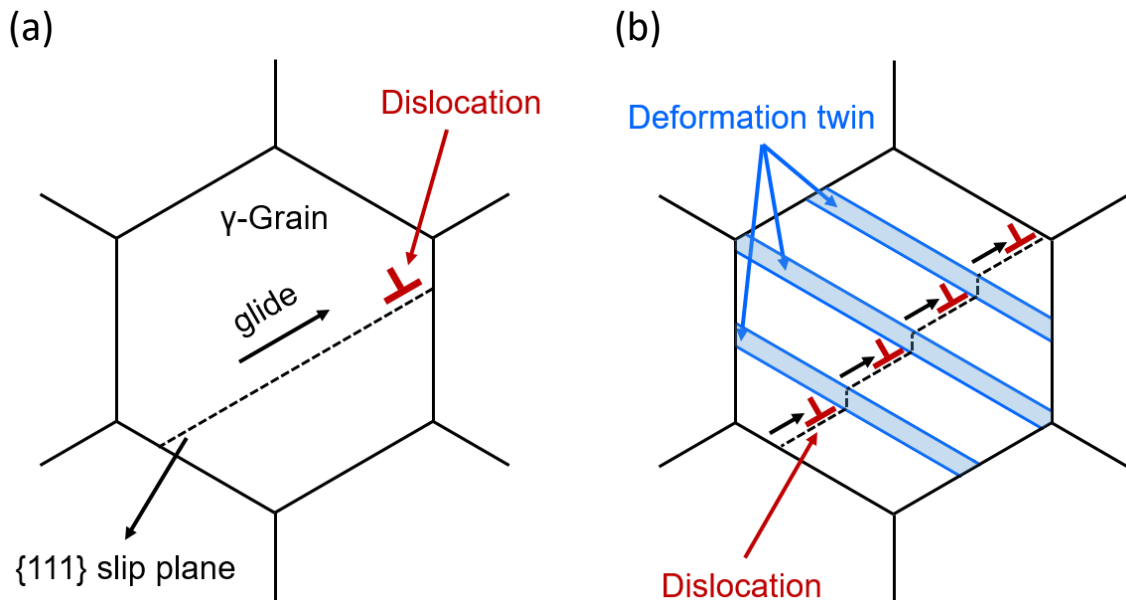
Fig. 1.2 Schematic illustration describing the dynamic Hall-Petch effect, where (a) is before deformation and (b) is after deformation. Dashed line indicates slip plane in FCC structure, and blue-colored regions in (b) indicate deformation twins, respectively.

1.2 Serration behavior in high-Mn austenitic steels

Carbon-containing steels frequently show serration behavior in their deformation curves. The serration behavior has been considered as a result of dynamic interaction between dislocations and solute atoms, which is called dynamic strain aging (DSA) [7,8].   The most well-known case for DSA is so-called 'blue brittleness' in ferritic steels [9].   As the ferritic steels are deformed at intermediate temperature range (373 K~ 573 K), carbon atoms are diffused near the dislocation core and pin the mobile dislocations, resulting in serrated flow accompanied with plastic instabilities in deformation curve, which is known as Portevin-Le Chatelier (PLC) effect [10,11]. It has been reported that PLC effect in the ferritic steels significantly decreases the ductility and leads to brittle fracture.   The blue brittleness in the ferritic steels has been the critical problems in manufacturing process and quality control of the steels.

On the other hand, carbon-containing high-Mn austenitic steels also frequently show the serration behavior.   **Figure 1.3 (a)** shows the stress-strain curves of 18Mn-1.7Al-0.5Si-0.75C steel tensile-deformed at different temperatures [12].   The materials tensile-deformed at intermediate temperatures (373 K and 473 K) exhibited the serration behavior along the tensile strain, whereas the materials tensile-deformed at 298 K and 573 K did not exhibit the serration behavior.   On the contrary to the blue brittleness in the ferritic steels, the materials showing the serration behavior (red and blue) showed larger ductility with having similar tensile strength, compared to the

8

materials without the serration behavior (black and green). **Fig. 1.3 (b, c, d)** shows their

deformation microstructures at a true strain of 0.3.   It was found that the area fraction of

deformation twins decreased with increasing the temperature, and there was very small fraction of

deformation twins in the microstructures deformed at 373 K and 473 K.   The results indicate that

the high strength and large ductility of the materials deformed at 373 K and 473 K was not attributed

to the TWIP or dynamic Hall-Petch effect.   The authors argued that the DSA was the dominant

mechanism responsible for the high strength and large ductility in the materials showing the

serration behavior.
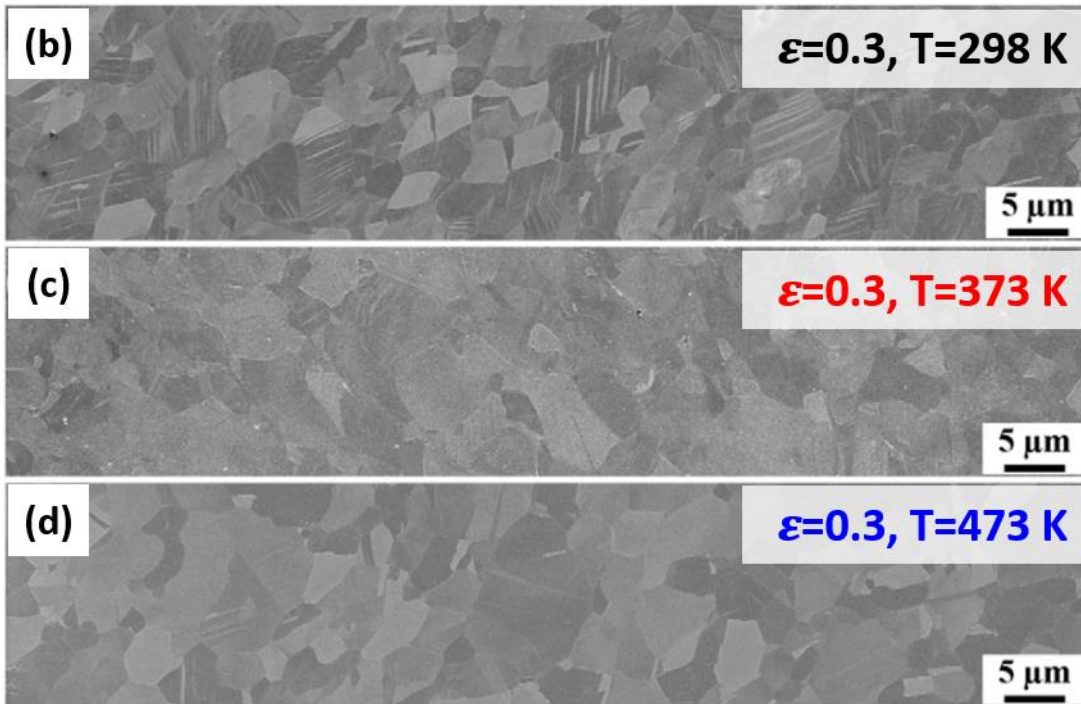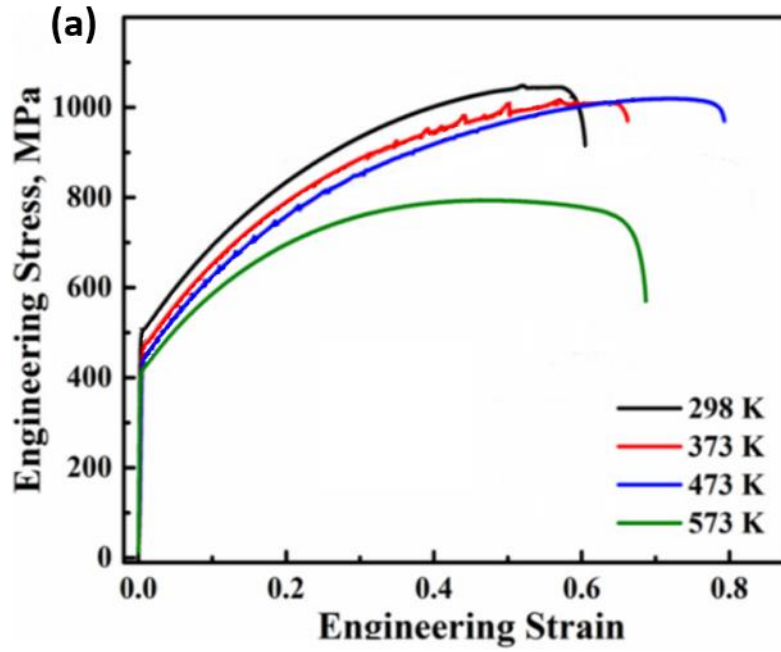
Fig. 1.3 (a) Engineering stress-strain curves of the 18Mn-1.7Al-0.5Si-0.75C steels tensile-deformed at different temperatures. Deformation microstructures at the true strain of 0.3 at (b) 298 K, (c) 373 K and (d) 473 K.

Besides deformation temperatures [12–15], many researchers have reported that the DSA accompanying the serration behavior is promoted under certain strain rates [13–18] and carbon contents [19,20], where dislocations are trapped by carbon atoms in a Cottrell atmosphere. Estrin investigated the effect of strain rate on DSA by calculations [18]. They found out that the DSA occurred only under the certain strain rate, where the parameter of the strain rate sensitivity ($m = d \ln \sigma / d \ln \dot{\varepsilon}$) was negative. According to their theory, dislocations glide slowly dragging solute atoms at low strain rate while dislocations glide rather fast without being hindered by the solute atoms at high strain rate. On the other hand, at the intermediate strain rate range, plastic deformation is inherently unstable, leading to the serration behavior and inhomogeneous deformation along the specimen in a form of band.

Lee et al. investigated the effect of carbon contents on mechanical properties [20]. The materials used in their study were Fe-31Mn, Fe-29Mn-0.3C and Fe-25Mn-0.6C having similar SFE ($\gamma \approx 44$ mJ/m^2). The three materials are referred to as 0C, 3C and 6C steels, respectively. **Figure 1.4 (a)** shows the engineering stress-strain curves of 0C, 3C and 6C steels. Interestingly, the yield strength, tensile strength, and ductility increased simultaneously with increasing carbon contents. The serration behavior was clearly observed in 3C and 6C steels. **Fig. 1.4 (b)** shows the twin fraction in the 3C and 6C steels obtained by EBSD. Deformation twins were not observed in 0C steel, according to the authors. The authors attributed the enhanced mechanical properties to the prevalent twinning in 3C and 6C steels, of which critical resolved shear stress

decreased with increasing the carbon contents.   Even though the authors overlooked the obvious serration behavior in 3C and 6C steels and they did not discuss about it in their paper, the results strongly suggest that the serration behavior associated with DSA significantly affect the mechanical properties.
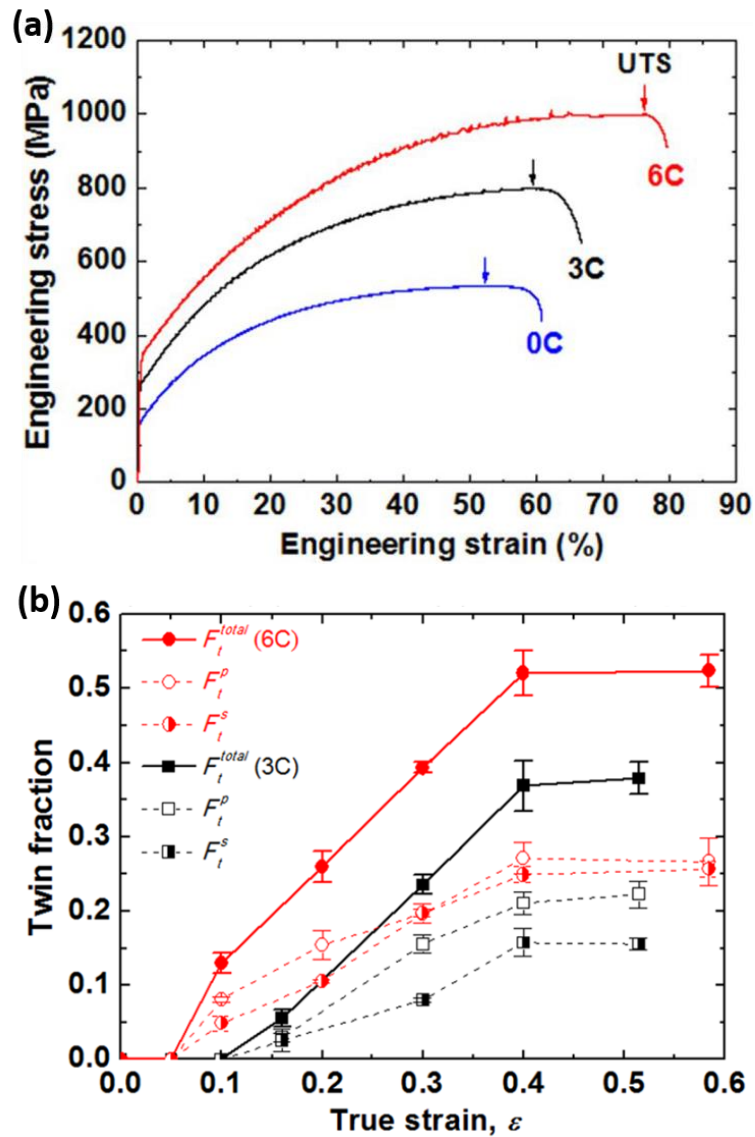
Fig. 1.4 (a) Engineering stress-strain curves of Fe-31Mn (0C), Fe-29Mn-0.3C (3C) and Fe-25Mn-0.6C (6C) steels. (b) Difference in the fraction of total (F_t^{total}), primary (F_t^p) and secondary (F_t^s) deformation twins as a function of true strain. Red and black lines indicate the change of twin fraction in Fe-25Mn-0.6C (6C) and Fe-29Mn-0.3C (3C) as a function of true strain, respectively.

Several researchers proposed the models in order to explain the DSA mechanism in high-Mn austenitic steels [5,19–21]. **Figure 1.5** shows the most referred model, which was firstly proposed by Lee et al. and reproduced by De cooman et al [5,21]. Lee and De cooman suggested that the DSA was associated with the interaction between leading partial dislocation and carbon atom. As a leading partial dislocation glided on the (111) plane, a carbon atom near the stacking fault plane forcedly transferred from octahedral site to tetrahedral site (**Fig. 1.5 (b)**). The authors argued that this resulted in significant lattice distortion and produced a strengthening effect, i.e., DSA effect. Then, the carbon atom reoriented itself by a single diffusive hop to an octahedral site away from the stacking fault plane ((**Fig. 1.5 (c)**) because the interstitial carbon atom at the tetrahedral site was unstable (**Fig. 1.5 (d)**) and the carbon also had an effect to increase the local SFE. They argued that this process would clear all the carbons out near the stacking fault plane and enhance the planar glide. Koyama et al. noted that deformation twins were formed in 18Mn-1.2C steel even with its high SFE ($\gamma = 55$ mJ/m^2) at 473 K [19]. They found that the steel exhibited serration behavior in the stress-strain curve tensile-deformed at 473 K, and they tried to correlate the serration behavior with deformation twins. **Figure 1.6** describes the DSA model proposed by Koyama et al. They argued that carbon atoms trapped a trailing partial dislocation when the Schmid factor of the trailing partial dislocation was much lower than that of the leading partial dislocation. As a result, the critical stress for deformation twinning became low when the DSA occurred, and it resulted in deformation twinning even though the steel had the high SFE.

13

They regarded this phenomenon as the DSA in high-Mn austenitic steels.

However, both models proposed by Lee and Koyama could not explain how such a nanoscale interaction between the solute atoms and the extended dislocations resulted in the global deformation responses appearing as the serration behavior on stress-strain curve. In addition, they did not consider very important feature of the serration behavior that the DSA accompanying the serration behavior was a repeated process during deformation. If the interaction between the solute atoms and the extended dislocations ended at once either by clearing carbons near the stacking fault plane (Lee and De cooman's model) or trapping trailing partial dislocation (Koyama's model), serration behavior would not be repeated during the deformation.
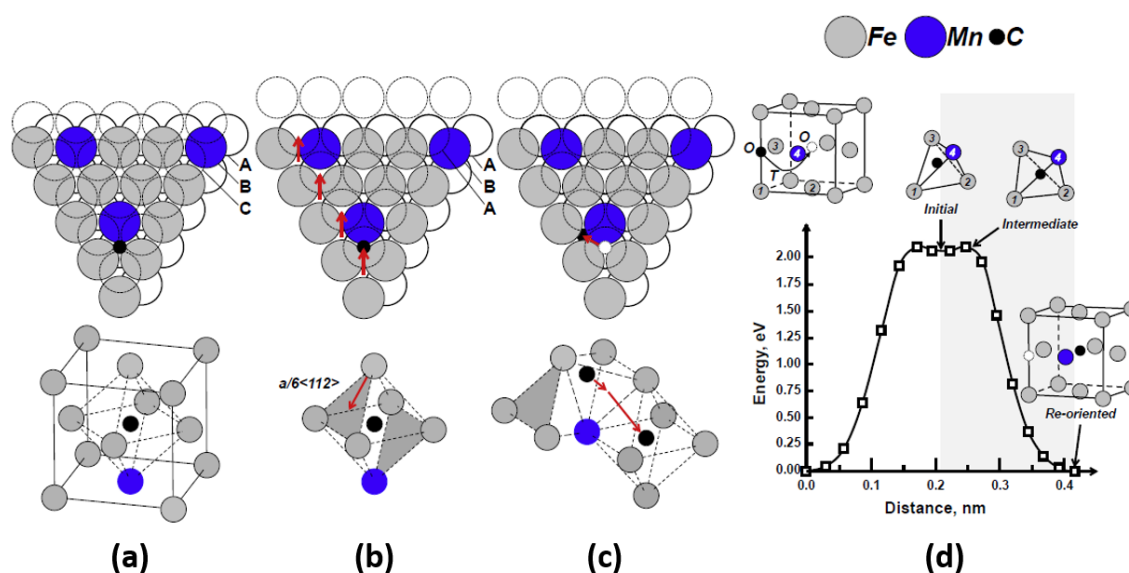
Fig. 1.5 Schematic illustration describing the reorientation of a carbon atom during the passage of a leading partial dislocation. (a) Atoms arrangement before the passage of a leading partial dislocation. (b) Lattice shear by the glide of a leading partial dislocation, causing the carbon atom to be located at a tetrahedral site. (c) Single diffusive hop of the carbon atom to an energetically more favorable neighboring octahedral site, which is away from the stacking fault plane. (d) Energy state depending on the carbon position.

14
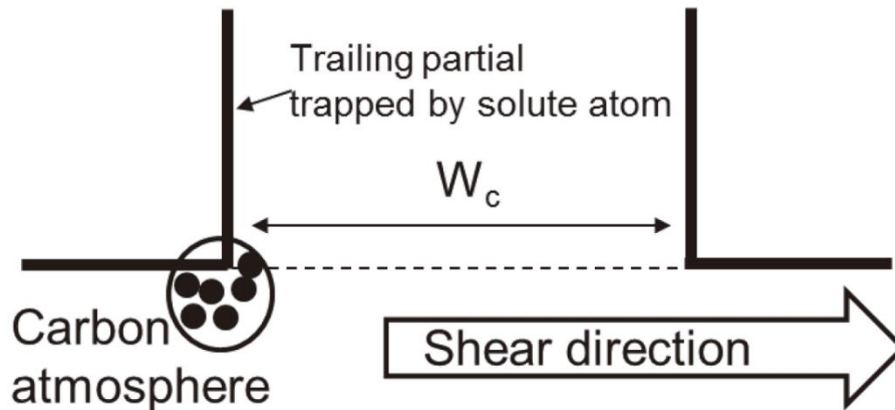
Fig. 1.6 Schematic illustration describing pinning of carbon atoms to trailing partial dislocation, when the Schmid factor of the leading partial was higher than that of trailing partial dislocation.

1.3 Heterogeneous deformation in high-Mn austenitic steels

It has also been reported recently that high-Mn steels showing the serration behavior accompany a heterogeneous deformation characterized as propagation of strain localized bands that are often called PLC bands.   Chen et al. investigated the localized deformation induced by PLC effect in 18Mn-0.6C steel [22].   **Figure 1.7 (a)** and **(b)** shows the global change of stress and strain during the experimental time from 120 s to 280 s, respectively.   The serration behavior was found in the stress-time curve (**Fig. 1.7 (a)**).   Interestingly, strain increased in a stepwise manner, and the time interval between each step increased with deformation time (**Fig. 1.7 (b)**).   **Fig. 1.7 (c)** shows the local change of the temperature at the center of the gage part during the experimental time from 120 s to 280 s.   The temperature at the center of the gage part increased from 50 °C to

110 °C with having the fluctuation ranging from ± 5 °C to ± 20 °C with increasing the strain (**Fig. 1.7 (c)**). **Fig. 1.7 (d)** shows the propagation of the PLC band from the experimental time of 165 s to 171 s. The authors argued that local heating (**Fig. 1.7 (c)**) was caused by the propagation of PLC bands (**Fig. 1.7 (d)**), where strain was concentrated within the band. Even though the authors did not pay attention to the temperature difference in detail, it is notable that the temperature difference between within the PLC band and beyond the PLC band was as small as 5°C to 20°C. The small increase of the temperature within the PLC band suggested that long-range carbon diffusion along the PLC band propagation was unlikely to happen. The time requirement for carbon atoms to diffuse from one octahedral site to a neighboring octahedral site (~0.4 nm) at the highest temperature of 110 °C (**Fig. 1.7 (c)**) was estimated at 226 s, where activation energy for carbon diffusion in the austenite (Q) was 112.5 kJ/mol and diffusion coefficient (D_0) was 0.0156 cm^2/s [5]. The authors clearly revealed the presence of the PLC band in the high-Mn austenitic steel, and the characteristic discontinuities in the stress-time and strain-time curves. However, the correlation between the nature of the localized bands and the PLC effect with serration behavior has not yet been clarified in the study.
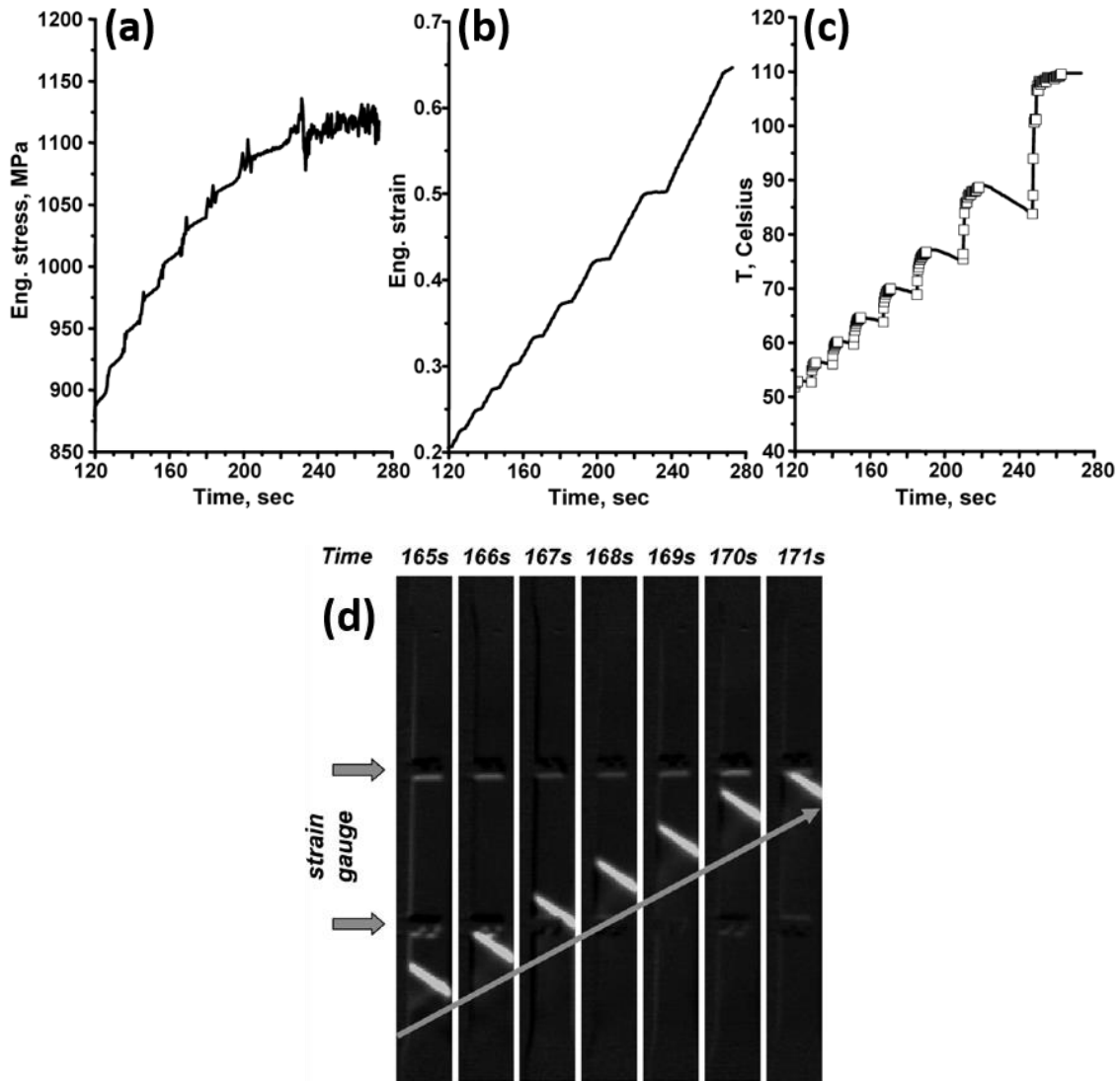
Fig. 1.7 The global change of (a) stress, (b) strain, and (c) the local change of the temperature at the center of the gage part during the experimental time from 120 s to 280 s. (d) The infrared thermographs of propagating PLC band with the temperature increase (+5°C) within the band.

1.4 Objective of the present thesis

Ever since Robert Hadfield discovered the TWIP steels in 1888, numerous studies were reported in order to explain the origin of the outstanding mechanical properties of the TWIP steel. On the contrary to the great progress in understanding the TWIP effect in high-Mn austenitic steels,

the role of serration behavior on mechanical properties, especially work-hardening, has not yet

been deeply understood.   Therefore, the current study aims to explore the nature of serration

behavior of the high-Mn austenitic steel, and the major objectives of the present study are as follows:

1. To clarify the correlation between a localized deformation band (PLC band) and a global mechanical response of a high-Mn steel appearing as the serration behavior.

2. To investigate the change of material parameters, e.g., dislocation density and lattice strain, caused by the PLC band propagation (PLC banding), for clarifying the effect of the PLC banding on plastic deformation and work-hardening behavior.

3. To reveal the mechanism of DSA that causes the PLC banding in mesoscopic scale by comparing the dislocation velocity within the PLC band and beyond the PLC band.

4. To investigate the effect of grain size on the PLC banding, from a view point of different work-hardening behavior of the various grain-sized specimens.

1.5 Outline of the dissertation

The thesis is composed of five chapters.

In **Chapter 1**, the background and objective of the present study are introduced.

In **Chapter 2**, mesoscopic nature of the serration behavior in a high-Mn austenitc steel was systematically investigated.   A 22Mn-0.6C steel with a mean grain size of 2.0 μm was fabricated after 4 cycles of repeated cold-rolling and annealing process.   The propagation of PLC bands is analysed by means of digital image correlation (DIC) method and the *in-situ* synchrotron XRD measurement both applied during tensile deformation of the material, for correlating the localized deformation with the global mechanical properties including the serration behavior.

In **Chapter 3**, the DSA mechanism explaining the PLC banding in mesoscopic scale was investigated.   DIC method and *in-situ* synchrotron XRD measurement was simultaneously applied during the tensile test.   From the experimentally obtained data, dislocation velocity was calculated and it was compared with the carbon diffusion velocity, for clarifying the pinning and de-pinning of dislocations with the PLC banding.

In **Chapter 4**, various grain-sized 22Mn-0.6C steels were fabricated by repeated cold-rolling and subsequent annealing process.   Onset strain of serration behavior, PLC band velocity, and strain localized in the PLC band were investigated on the various grain-sized specimens, with the aid of the DIC technique.

In **Chapter 5**, conclusions and new findings in the present study are summarized.

Chapter 2   Characterization of serration behavior in a high-Mn austenitic steel

2.1   Introduction

Serrations have been considered as a result of interactions between dislocations and solute

atoms, which is called dynamic strain aging (DSA) [7,8,21] or Portevin–Le Chatelier (PLC) effect

[10,11].   However, it is still unclear how such a nanoscale interaction between solute atoms and

dislocations results in the global deformation responses of the material including serrations on

stress-strain curves.   As introduced in the section 1.3, high-Mn steels also showed the serration

behavior accompanying with a heterogeneous deformation characterized as propagation of strain

localized bands that are called PLC bands, although the correlation between the nature of the

localized bands and the PLC effect with serrations has not yet been understood.   The achievements

so far have been mainly focused on the deformation variables under which serrations happen, and

little discussion has been done on the nature of serrations and their role on global mechanical

properties of materials.

One of the biggest hurdle for investigating the serration behavior has been how to evaluate

deformation localization in tensile tests, which cannot be measured by conventional methods like

extensometer or contact strain gages that can only measure average strains of the whole specimen.

Digital image correlation (DIC) technique has been introduced recently to quantify local strain

distributions in deformation of various metals and alloys [13,23–27].   In the DIC method,

displacements of different positions in the material are tracked during the deformation.   Local

displacements of patterns set on the surface of the tensile specimen are tracked, which enables the quantitative evaluation of local strain distributions during the deformation. For tracking the displacements of different positions, speckle patterns are covered on the surface of the material, or the microstructure contrast itself is used as markers. By applying the DIC method, it has been quantitatively clarified, for example, how martensitic transformation in a ultrafine grained metastable austenitic steel occurred in a heterogeneous manner, i.e., in the form of Lüders deformation, during tensile deformation, which was the key to realizing ultra-high strength and large ductility of the material [27]. Propagation of PLC bands in the materials showing serration behavior has been also investigated by the DIC method [13,23–26]. Halim et al. [26] found out the PLC band propagation in AA574 alloy by using DIC method, and investigated the effect of temperature and pre-strains on the serration behavior. However, the authors separately observed the macroscopic serration behavior and the local PLC banding in different tensile specimens, and they did not investigate the correlation. Canadinc et al. [23] examined strain rate sensitivity on flow stress of Hadfield steel, and simultaneously investigated the strain localization on a tensile specimen. They found out that flow stress decreased with increasing the strain rate, i.e., negative strain rate sensitivity. Eskandari et al. [25] also applied the DIC method to investigate the effect of strain rate and temperature on the strain localization in a high-Mn steel. Canadinc et al. and Eskandari et al. found out that the distribution of strains within the gage part were inhomogeneous at some global tensile strains, but they could not observe the PLC banding. This is probably

because the interval of global tensile strains was too large to detect the PLC banding having small strain.   Detailed correlation between the serration behavior and propagation of PLC bands was not achieved, and the role of PLC bands on the global deformation of materials are still unclear.

In-situ X-ray diffraction (XRD) measurement is another powerful method to understand a real-time evolution of material parameters, such as lattice strain and dislocation density, during deformation.   Adachi et al. [28] investigated the grain size dependence of the evolution of dislocation density during tensile deformation in a commercial purity Al by the use of an *in-situ* synchrotron XRD measurement, and found that the increase of dislocation density could be divided into the characteristic stages of which lengths depended on the average grain size.   Zhang et al. [29] revealed a development of lattice strain and dislocation density in a Lüders band propagating in a medium-Mn steel by the aid of an *in-situ* XRD measurement.   By fixing a focused X-ray beam at a certain position in the tensile specimen, heterogeneous deformation like PLC banding could be characterized by the *in-situ* XRD measurement.

The current chapter aims to explore the nature of serration behavior of a high-Mn steel in a mesoscopic scale.   The propagation of PLC bands is analyzed by means of the state-of-the-art DIC technique and the *in-situ* synchrotron XRD measurement both applied during tensile deformation of the material, for correlating the localized deformation with the global mechanical properties including the serration behavior.   In addition, the change of local stress with the propagation of PLC bands is precisely quantified, and the effect of the propagation of PLC band

on work-hardening is discussed.

2.2   Experimental procedures

2.2.1 Materials

A high-Mn austenitic steel, Fe-22Mn-0.6C (wt. %), was used in the present study.   The detailed chemical composition of the steel is shown in **Table 1**.   As illustrated in **Figure 2.1**, the as-received hot-forged plate 12 mm in thickness was subjected to 4 cycles of the cold-rolling and annealing treatments we developed before [30], in order to achieve grain refinement.   The thickness reduction at each cold-rolling step was 33.3%, 37.5%, 40% and 66.7%, respectively, and the final thickness of the sheet was 1 mm.   The intermediate annealing between each cold-rolling step was carried out at 600°C for 600 s for restoring deformability of the material.   The materials were water-cooled immediately after intermediate annealing.   A fine-grained specimen with an average grain size of 2.0 μm was obtained by annealing the final 1 mm thick sheet at 800°C for 300 s followed by water quenching.

Table 2.1 Chemical composition of the high-Mn steel investigated (wt. %).

C	Si	Mn	P	S	Al	Cr	O	N	Fe
0.56	0.06	21.68	<0.004	0.007	<0.01	<0.01	<0.0011	0.0049	Bal.
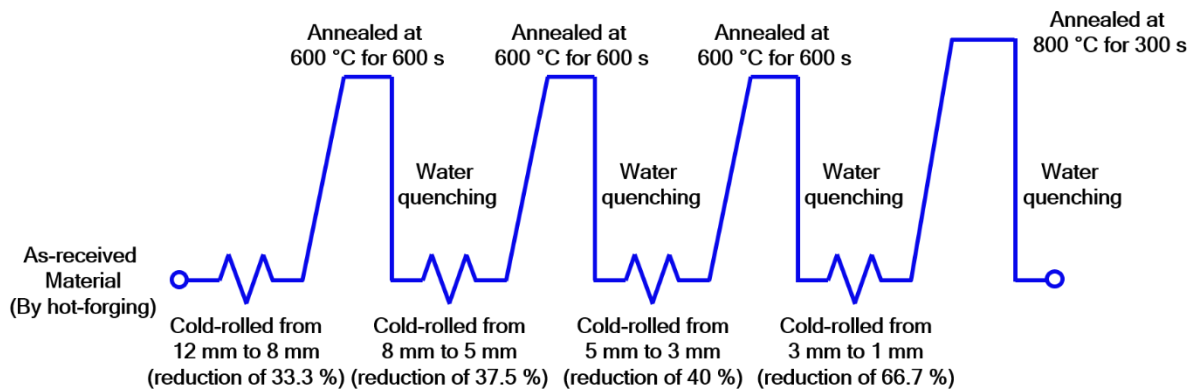
Fig. 2.1 Schematic illustration of thermomechanical process performed to 22Mn-0.6C steel.

2.2.2 Microstructure observation

After the final annealing, microstructural observations were carried out on a section perpendicular to the transverse direction (TD) of the sheet using a field-emission scanning electron microscope (FE-SEM: JEOL, JSM-7100F) equipped with an electron back-scattered diffraction (EBSD) operated at an accelerating voltage of 15 kV.   In order to obtain mirror-like surfaces, the TD section of the sheet was mechanically polished first by the use of 1000-4000 grit-sized fine SiC papers and then electro-polished in a solution of 10 % $HClO_4$ + 90 % C_2H_6O.   The mean grain size was determined by a line intercept method on EBSD images, counting high angle grain boundaries and annealing twin boundaries on the EBSD maps.   Texture and phases of the observed areas were also confirmed by EBSD using a software, TSL-OIM data collection and analysis ver. 5.31.

Deformation microstructures at an early stage of tensile deformation was also observed.

In order to characterize the deformation microstructures of the large area, the electron channeling contrast imaging (ECCI) technique was applied.   After the appearance of the second serration peak (e=0.023) in the stress-strain curve, the tensile specimen was unloaded and the microstructure observation was performed on three distinct regions: ① the region where PLC band has not yet swept, ② the region where PLC band was sweeping, ③ the region where PLC band finished sweeping.   Before the microstructure observations, the ND section of the deformed specimen was mechanically polished first by the use of 1000-4000 grit-sized fine SiC papers and then the specimen was polished again by using 3 and 1 μm diamond paste in order to remove dislocations introduced during the polishing treatment.   Then, the specimen was electro-polished in a solution of 10 % $HClO_4$ + 90 % C_2H_6O.   After the carful polish treatments, the ND surface of the specimen was observed in BSE mode at a working distance of 3 mm and acceleration voltage of 25 kV.   The specimen was tilted to find the best electron channeling condition with respect to the lattice orientation, so that the clear contrast between the defects and matrix was obtained.

2.2.3 Mechanical properties

Mechanical properties of the 22Mn-0.6C steel with the mean grain size of 2.0 μm were evaluated by tensile tests at an initial strain rate of 8.3 × 10^{-4} s^{-1} at room temperature using an uniaxial tensile testing machine (SHIMADZU, AG-100kN Xplus).   As shown in **Figure 2.2**, sheet-type tensile specimens with a gage length of 10 mm, gage width of 5 mm and thickness of 1

mm were cut from the cold-rolled and annealed sheet by an electrical discharge machine. The tensile direction was parallel to the rolling direction (RD) of the sheet. Tensile tests of the specimen with the mean grain size of 2.0 μm were also conducted for a DIC analysis. The dimension of the tensile specimens and condition for the *in-situ* X-ray diffraction experiments are explained in the section 2.2.5.
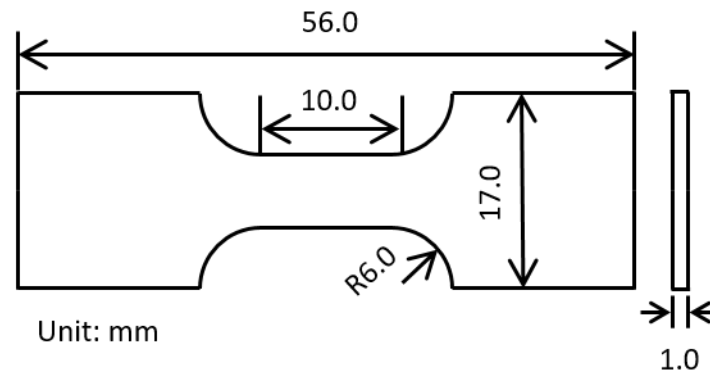
Fig. 2.2 Schematic illustration of the tensile specimen.

2.2.4 DIC analysis

In order to evaluate distributions of local strain and strain rate in the tensile specimens during the tensile test, a DIC technique was applied. Prior to the experiment, broad surfaces of the sheet-type tensile specimens were first painted white and then covered with randomly distributed black speckle patterns by using an airbrush, as shown in **Figure 2.3**. The speckle patterns were deformed together with the tensile specimens and used as markers to track displacements of different positions in the specimens. During the tensile deformation, the speckle

26

patterns were recorded at a rate of 5 frames per second by a CCD (charge-coupled device) camera with a resolution of 2432 × 2054 pixels. Two-dimensional strain tensors at different positions were obtained by differentiating displacement vectors obtained by tracking the speckle patterns. The recorded CCD images were analyzed by the use of Vic-2D software with a subset of 29 pixels in a square and a step size of 7 pixels, which was optimized for assessing local strains and strain rates under the given resolution of the CCD camera. **Figure 2.4** shows the displacement of a subset in two dimensions. Before deformation, the center of the subset is marked as point P, and point Q (x, y) is at the position of Δx and Δy apart from the center of the subset (P). After deformation, the point P moved to point P' by u in x-direction and v in y-direction, and point Q moved to Q' (x', y'), respectively. Here, Q' (x', y') is described as follows,

$$x' = x + u + \frac{\partial u}{\partial x}\Delta x + \frac{\partial u}{\partial y}\Delta y \tag{2.1}$$

$$y' = y + v + \frac{\partial v}{\partial x}\Delta x + \frac{\partial v}{\partial y}\Delta y \tag{2.2}$$

where u and v are displacement in x-direction and y-direction, respectively, and $\frac{\partial u}{\partial x}$, $\frac{\partial u}{\partial y}$, $\frac{\partial v}{\partial x}$ and $\frac{\partial v}{\partial y}$ correspond to e_{xx}, e_{xy}, e_{yx} and e_{yy}, respectively. Local strain rates $(\frac{\Delta e_{ij}}{\Delta t})$ at different positions were also evaluated by the use of the local strain data (e_{ij}). From such results, distributions of strain or strain-rate in the specimen were exhibited in the form of local strain or strain-rate maps.

It should be noted that the global stress and the local strains (and strain rates) were obtained by different tools: the global stress of the specimen was measured from the tensile-test machine equipped with a load cell, while the local strains were evaluated from the DIC images recorded by the CCD camera as was described above. The global stress obtained from the tensile machine and the local strains obtained from the DIC analysis were synchronized by adjusting the time of macroscopic fracture, as shown in **Figure 2.5**.
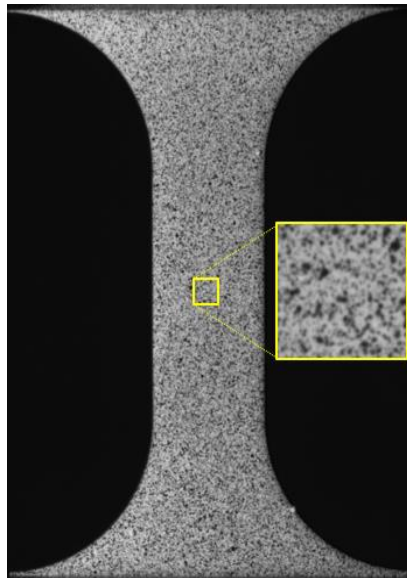
Fig. 2.3 The sheet-type tensile specimens first painted white and then sprayed with black speckle patterns.
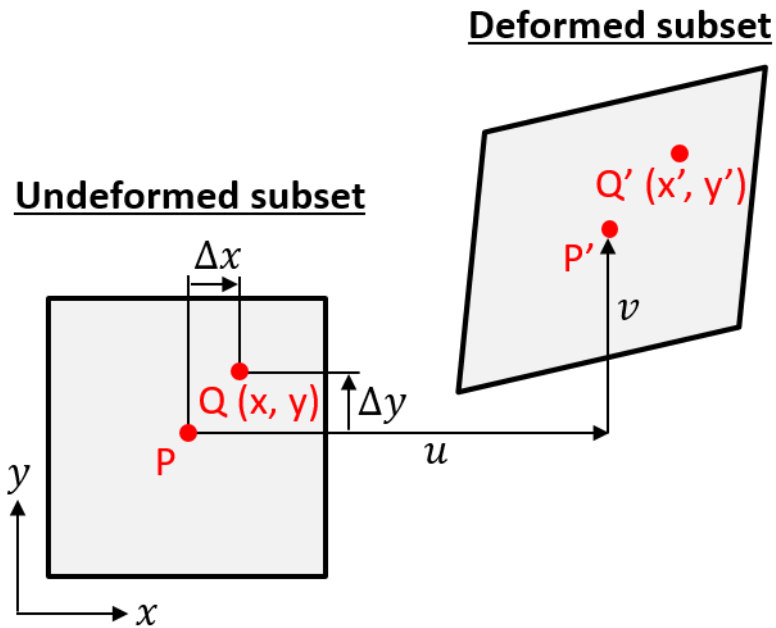
Fig. 2.4 Schematic illustration of strain measurement in DIC analysis
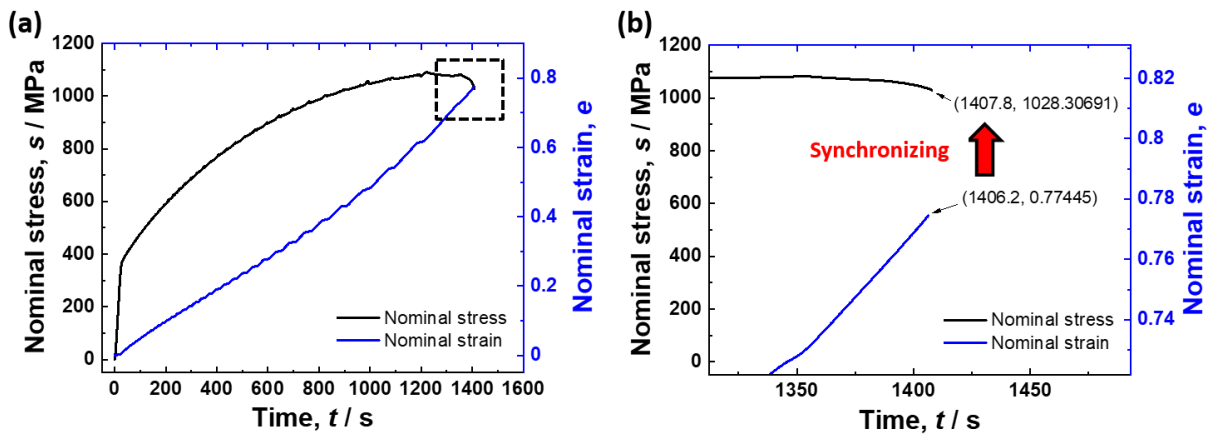
Fig. 2.5 (a) Nominal stress (left y-axis) and nominal strain (right y-axis) plotted as a function of deformation time. (b) Late stage of deformation is enlarged, and the arrow in the figure indicates the time at strain of fracture (blue) is synchronized to the time at stress of the fracture (black).

2.2.5 *In-situ* synchrotron XRD measurements

In-situ synchrotron XRD measurements were performed for evaluating lattice strain and dislocation density during the tensile test.   High energy (HE) synchrotron beam line of BL46 XU at SPring-8 (Super Photon ring – 8 GeV) of Japan Synchrotron Radiation Research Institute (JASRI) was utilized, which could provide diffraction profiles over a wide range of angles with a high resolution of time.   A monochromatic synchrotron beam with an intensity of 30 keV ($\lambda = 0.0413$ nm) was used for the transmission diffraction.   The time resolution for a diffraction profile was 1 second.   The configuration of the *in-situ* XRD measurement during the tensile test is illustrated in **Figure 2.6**.   **Figure 2.7** shows the sheet-type tensile specimen with a gage length of 10 mm, gage width of 3 mm and thickness of 0.5 mm, which was cut from the sheet having the fully recrystallized microstructure with an mean grain size of 2.0 μm.   The tensile direction was parallel to the rolling direction (RD) of the sheet.   Incident beam having a size of 2.0 mm in the gage-width direction and 0.5 mm in the gage-length direction was irradiated at the center of the gage part in the tensile specimen.   The direction of the incident beam was perpendicular to the tensile direction.   After a precise alignment, the tensile tests with the *in-situ* XRD measurement were carried at an initial strain rate of 8.3×10^{-4} s^{-1} at room temperature.   In the tensile test, the tensile specimen was elongated upward with the bottom grip part fixed.   During the tensile deformation, diffraction profiles were simultaneously collected by serially-connected 6 detectors (MYTHEN X, Dectris).   The diffraction peaks were fit to Voigt function using Origin Pro 2017 program, and

then the peak position and full width half-maximum (FWHM) of peaks were determined.   Peak

positions and FWHMs of (111), (200), (311) and (222) were considered for subsequent analysis.

Fig. 2.6 Schematic illustration showing the *in-situ* XRD measurement during tensile test at SPring-8.
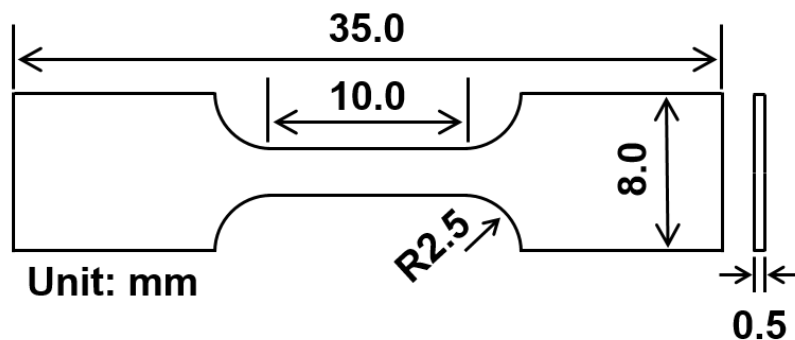
Fig. 2.7 Schematic illustration of the tensile specimen for *in-situ* synchrotron XRD measurement.

2.2.6 *In-situ* neutron beam diffraction experiment during tensile test

In order to measure the elastic modulus of the 22Mn-0.6C steel, *in-situ* neutron beam diffraction measurement was performed during tensile test. The reasons why elastic modulus was calculated not from the *in-situ* synchrotron XRD beam measurement but from the *in-situ* neutron beam measurement were (1) interval time for measurement in the *in-situ* synchrotron XRD beam diffraction was slightly irregular, e.g., 1 s, 2.2 s and 3.3 s…, which made a small deviation in determining the slope of lattice strain and nominal stress, and (2) neutron diffraction provided the change of lattice strain parallel to the tensile direction, so that elastic modulus could be obtained directly from the slope of the lattice strain and nominal stress.

The experiment was carried out using beam line of TAKUMI at J-PARC (Japan Proton Accelerator Research Complex), and the configuration of the *in-situ* neutron beam diffraction measurement during tensile test is illustrated in **Figure 2.8**. The tensile direction (TD) formed 45° with the incident beam, and the detector 1 and detector 2 were located to form 90° and -90°, respectively, with the TD. The diffracted beam from the planes perpendicular to the TD was collected to the detector 1, and the diffracted beam from the planes parallel to the TD was collected to the detector 2. In the present study, only the planes perpendicular to the TD was concerned, for obtaining the change of lattice strain parallel to the tensile stress. **Figure 2.9** shows the sheet-type tensile specimen with a gage length of 12 mm, gage width of 3.0 mm and thickness of 1.0 mm. The mean grain size of the specimen used in the experiment was 2.0 μm, which was same with the

specimen used in the DIC analysis and *In-situ* synchrotron XRD measurement.   After a precise

alignment, the tensile test with neutron beam diffraction measurement was carried at an initial strain

rate of 8.3 × 10⁻⁴ s⁻¹ at room temperature.   During the tensile deformation, neutron beam was

irradiated on the center of the tensile specimen.   **Figure 2.10** shows the change of nominal stress

with deformation time of the specimen with the mean grain size of the 2.0 μm.   The crosshead

was stopped at the five stress levels within the elastic region (10, 90, 180, 270 and 360 MPa), and

the strain rate was immediately slowed down almost to zero for 180 s, for obtaining enough

intensities of the diffraction profiles.   Since the neutron beam was composed of continuous range

of wave lengths and velocities, time of flight (TOF) of the beam changes depending on the

diffraction plane.   Therefore, TOF was converted into the interval of each *hkl* plane as follows,

$$d_{hkl} = \frac{1}{2 \sin \theta} \cdot \frac{h}{mL} \cdot t \qquad (2.3)$$

where θ is the diffraction angle (here, θ is fixed to 45° irrespective of the diffraction plane), m

is the mass of a neutron, L is the distance of flight, h is Planck constant (6.62×10^{-34} m²kg/ s) and
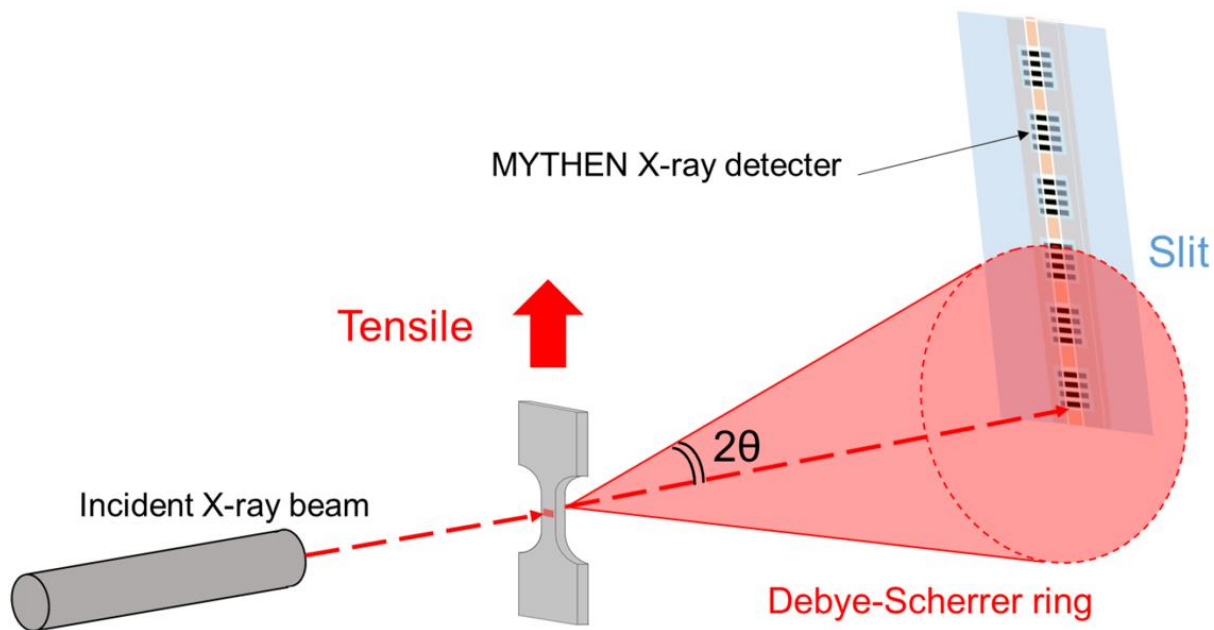
t is the time of flight (TOF).
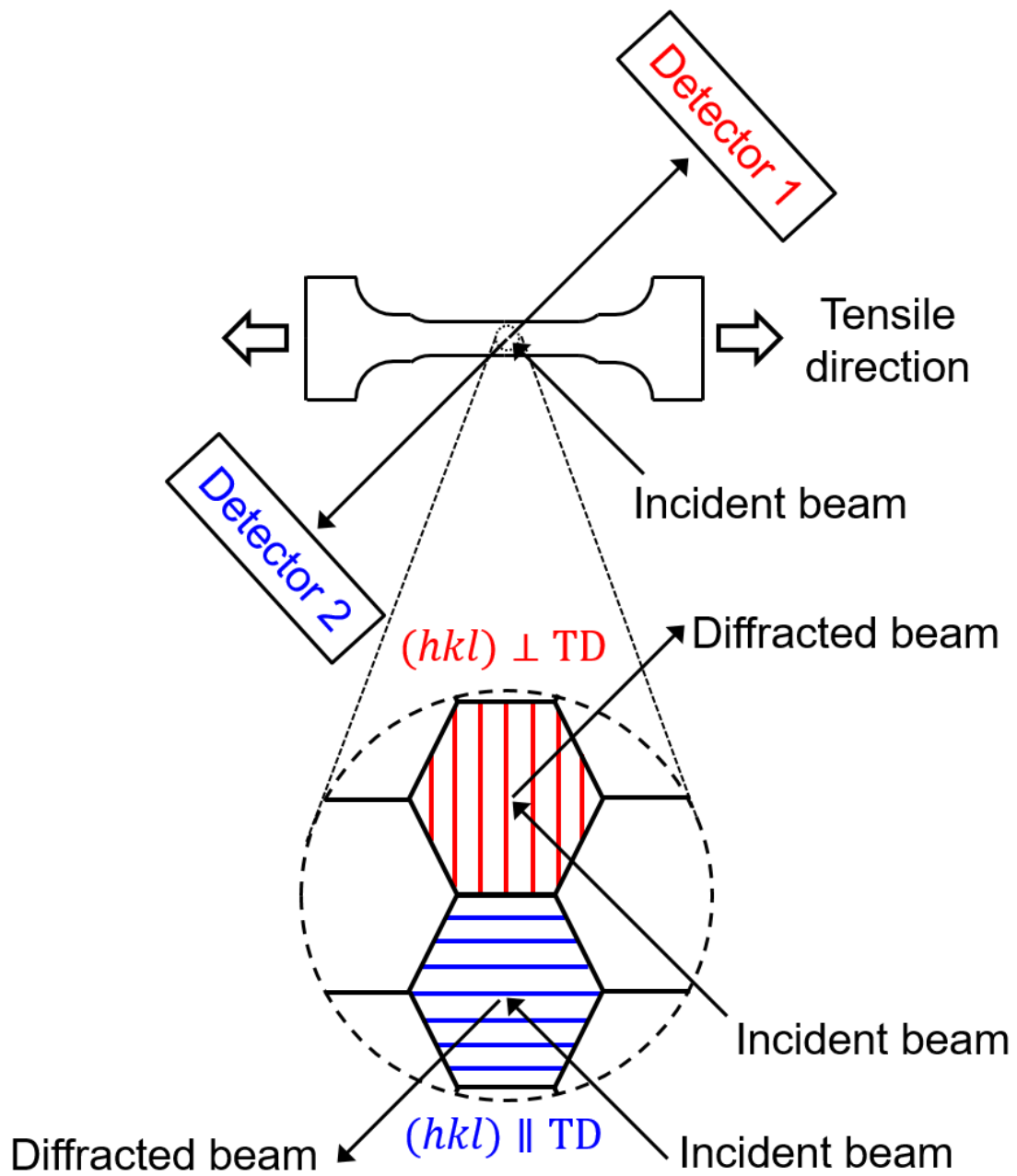
Fig. 2.8 Schematic illustration of the *in-situ* neutron measurement during tensile test at J-PARC.
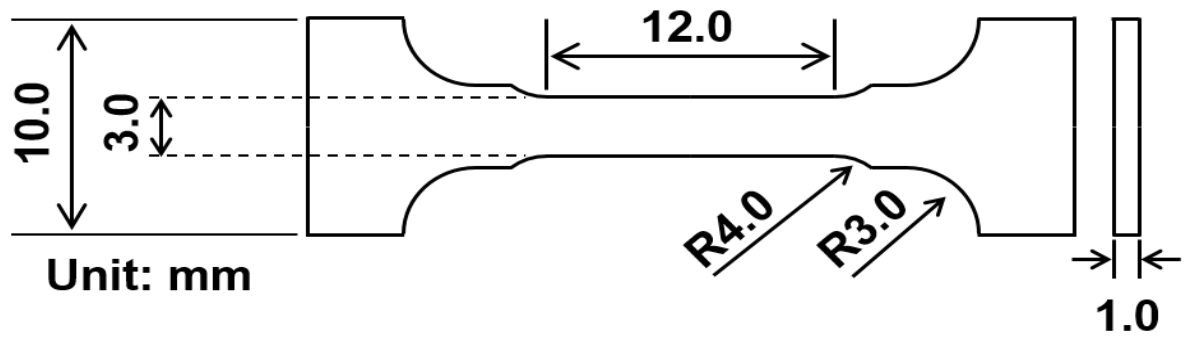
Fig. 2.9 Schematic illustration of the tensile specimen for *in-situ* neutron measurement.
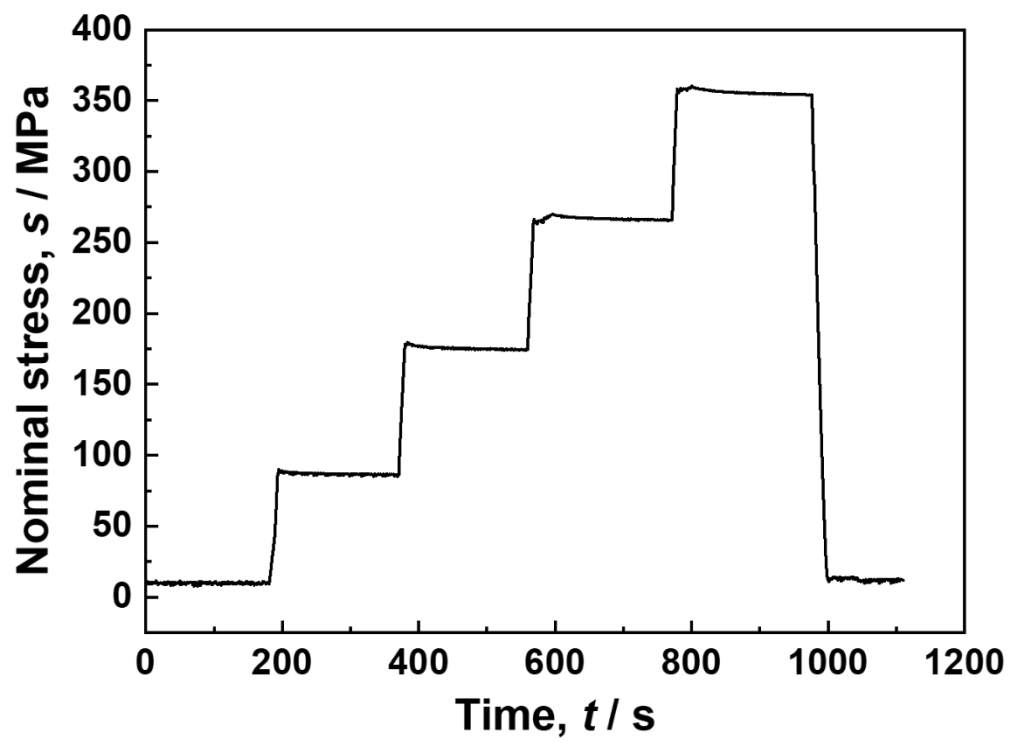
Fig. 2.10 The change of nominal stress with deformation time of the specimen with the mean grain size of the 2.0 μm. Diffraction profiles at the five stress levels within the elastic region (10, 90, 180, 270 and 360 MPa) were collected for 180 s.

2.3   Results and discussion

2.3.1 Microstructure before tensile test

Figure 2.11 (a) shows an EBSD inverse pole figure (IPF) map overlapped with an image quality (IQ) map of the specimen fabricated by the repeated cold-rolling and annealing.   The microstructure was observed on a longitudinal plane perpendicular to TD of the sheet.   Colors in the IPF map indicate crystallographic orientations parallel to TD, according to the key stereographic triangle inserted.   High angle grain boundaries (HAGBs) and annealing twin boundaries (TBs) are drawn by black lines and red lines, respectively, on EBSD maps.   The specimen showed the fully recrystallized microstructure, of which average grain size including TBs was 2.0 μm.   **Figure 2.11 (b)** shows a phase map together with HAGBs and TBs of the identical area of **Fig. 2.11 (a)**.   Yellow color indicates FCC structure confirmed from the Kikuchi-line diffraction pattern obtained at each point.   All areas showed yellow color, i.e., FCC structure, which proved that the specimen had an austenite single-phase structure.   **Fig. 2.11 (b)** also confirmed clearly that almost all grains were surrounded by HAGBs and the microstructure involved a high density of annealing TBs (39.2 % of all boundaries shown in **Fig. 2.11 (b)**).

Figure 2.11 (c) shows (001), (011) and (111) pole figures of the specimen constructed from the EBSD result.   The EBSD data of **Fig. 2.11 (a)** and **(b)** was rotated so that ND lies at the center of the pole figures.   All the pole figures exhibited low intensities, indicating that the specimen fabricated by the repeated cold-rolling and annealing process did not have strong crystallographic

36

texture.
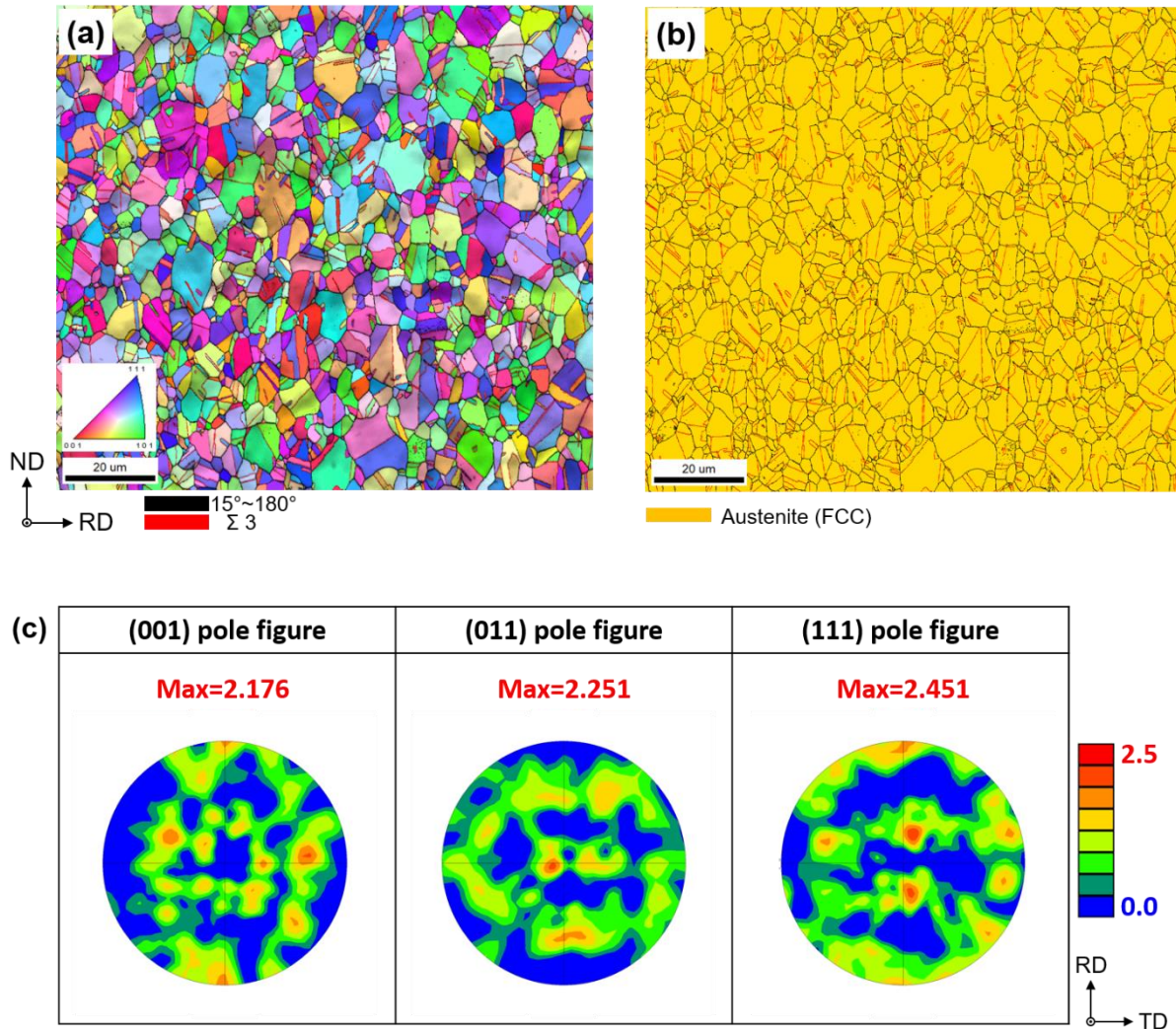
Fig. 2.11 EBSD results of the specimen prepared by the repeated cold-rolling and annealing process. (a) EBSD IPF map + IQ map. Colors indicate crystallographic orientations parallel to TD, according to the key stereographic triangle inserted. High angle grain boundaries (HAGBs) and annealing twin boundaries (TBs) are indicated as black lines and red lines, respectively. (b) EBSD phase map with HAGBs and TBs. FCC phase is expressed in yellow color. (c) (001), (011) and (111) pole figures of the specimen. The original EBSD data in **Fig. 2.11 (a)** and **(b)** were rotated so that ND lies at the center of the pole figures.

2.3.2 Stress-strain curve and strain hardening rate curve

A nominal (engineering) stress-strain curve of the specimen with the mean grain size of 2.0 μm is shown in **Figure 2.12 (a)**.   The specimen showed a good combination of high strength and large ductility with a yield strength (0.2 % proof stress) of 430 MPa, tensile strength of 1136 MPa and total elongation of 69 %.   The true stress-strain curve is shown in **Fig. 2.12 (b)**, which was obtained from the nominal stress-strain curve.   The total true strain was 0.53, and the maximum true stress was 1870 MPa.   **Fig. 2.12 (c)** shows the strain hardening rate ($d\sigma/d\varepsilon$, blue) and true stress (σ, red) of the specimen plotted as a function of true strain (ε).   The specimen maintained high strain hardening rate around 2000 MPa until the later stage of deformation.   The strain hardening rate showed severe fluctuation from about -5000 MPa to 15000 MPa, which corresponded to the serrated flow observed on the stress-strain curve.   The intersection of the strain hardening rate curve and the true stress-true strain curve corresponds to initiation of necking, which is also called plastic instability.   Considère's criterion for plastic instability is described as following formula [31].

$$\sigma \geq d\sigma/d\varepsilon \qquad\qquad\qquad (2.4)$$

where σ is the true stress, ε is the true strain and $d\sigma/d\varepsilon$ is the strain hardening rate, respectively.   When necking happens in a tensile specimen, the cross-sectional area in necking region decreases and proceeds to fracture.   The specimen showed very small post-uniform elongation, which indicated the specimen fractured soon after necking started.   This tendency is

frequently observed in high-Mn austenitic steels compared with other metallic materials.   The

small post-uniform elongation in the present material would be discussed in the section 2.3.10.
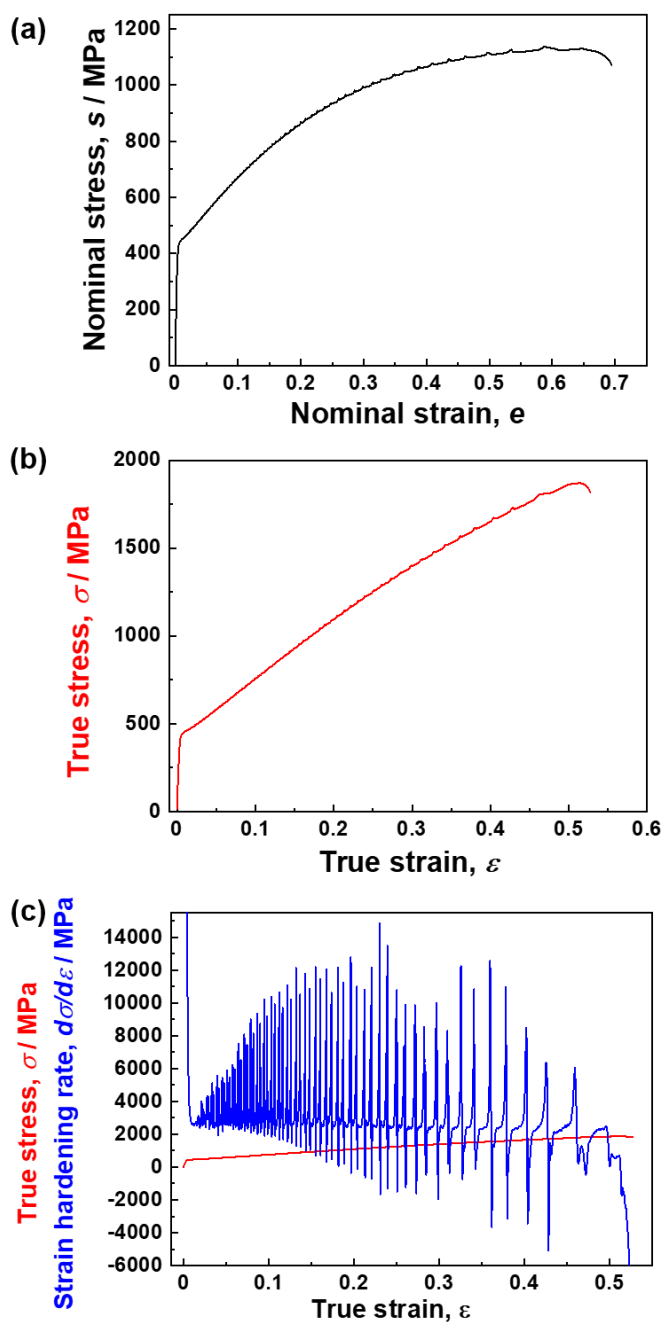
Fig. 2.12 (a) Nominal stress-strain curve of the specimen with a mean grain size of 2.0 μm. (b) True stress-strain curve obtained from the nominal stress-strain curve. (c) Strain-hardening rate (blue) and true stress (red) curves plotted against true strain.

2.3.3 Heterogeneous deformation characterized by DIC

The DIC analysis was carried out for characterizing the heterogeneity of deformation in a specimen scale.   Formation and propagation of PLC bands were observed in the gage part of the tensile specimen during the tensile test.   It was found that the amount of strain localized within PLC bands was not so high at the early and medium stages of tensile deformation (in a range of 0.0039 ~ 0.0108), so that it was difficult to observe PLC bands on local strain maps indicating the magnitude of strain in different colors using a large strain scale (like 0 ~ 0.5 in tensile strain (ε_{yy})).   Hence, strain-rate maps were used in the present study to exhibit or characterize the PLC bands.   **Figure 2.13** shows DIC strain-rate maps captured at different engineering tensile strains (e_{yy}) in a range from e_{yy} = 0.1193 to e_{yy} = 0.1303, which corresponded to one cycle of PLC band propagation along the whole gage length of the specimen.   The numbers (1) ~ (9) on figures indicate the positions on the corresponding stress-strain curve shown later (**Fig. 2.14 (b)**).   The magnitude of local strain rate is expressed in different colors according to the key color bar inserted in **Fig. 2.13**.   In (1) of **Fig. 2.13** a PLC band (former band) having higher local strain rates propagated from the center part to the lower part of the gage was disappearing in the lower shoulder part.   On the other hand, a new PLC band was nucleating at a little bit upper side of the gage center.   The new PLC band propagated upward, and the propagation of the PLC band was well captured in (2), (3) and (4)

40

of **Fig. 2.13**. The maximum strain rate within the PLC band in (2) ~ (4) was in a range from 0.0023 s^{-1} to 0.0027 s^{-1}, while the strain rate outside the PLC band was quite low and homogeneous (~0.0001 s^{-1}). Here, the global strain rate applied was 0.00084 s^{-1}. In (5), the band started to annihilate at the upper shoulder part, and another new band was about to nucleate at the middle of the gage part, which located slightly lower than the position where the previous band nucleated in (1). The newly nucleated band propagated downward (6, 7, 8) and was disappearing at the lower shoulder part in (9). Then, another new PLC band was nucleating at a little bit upper position of the gage center in (9). Besides the strain range investigated in **Fig. 2.13**, the repetition of the formation, propagation and annihilation of PLC bands having higher local strain rates were clearly observed in the entire deformation. The band did not necessarily form near the gage center, but often nucleated at one end of the gage part and propagated throughout the gage in one direction. Regardless of such patterns of the PLC band propagation, however, the nucleation and propagation of the band of next cycle started only after every position in the gage part was swept by the band(s) in the former cycle.
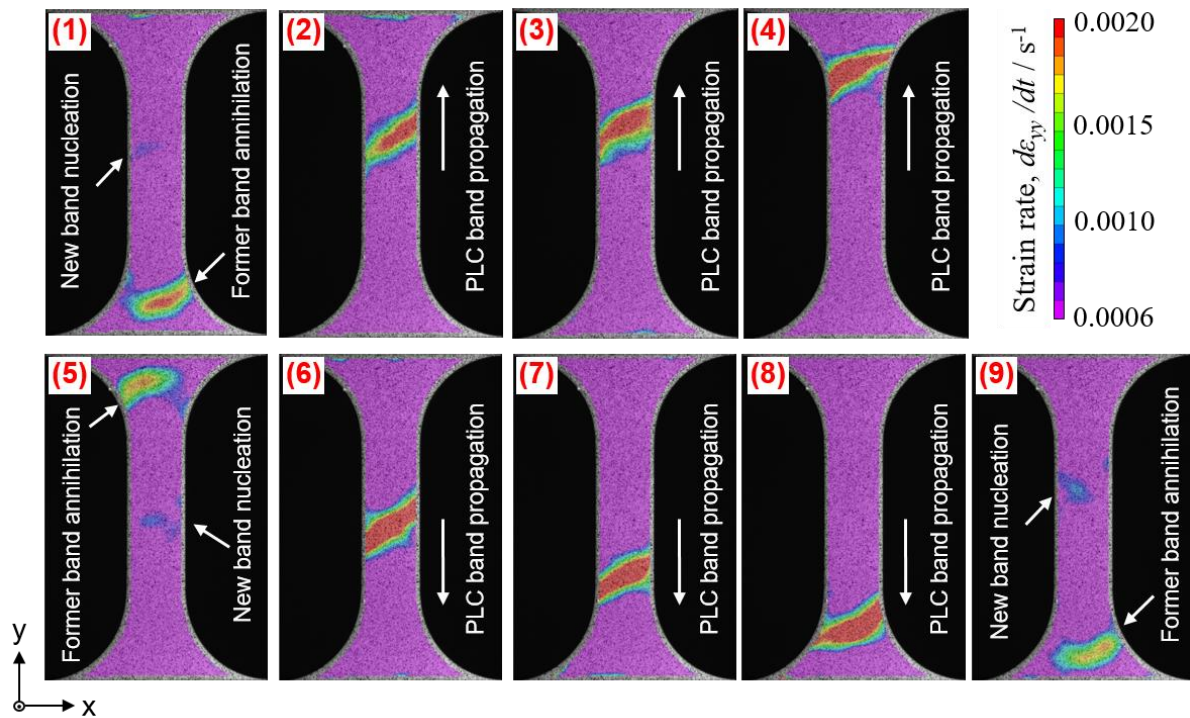
Fig. 2.13 DIC local strain-rate maps captured at different engineering tensile strains (e_{yy}), corresponding to one cycle of PLC band propagation through the gage part. (1) e_{yy} = 0.1193, (2) e_{yy} = 0.1199, (3) e_{yy} = 0.1210, (4) e_{yy} = 0.1236, (5) e_{yy} = 0.1241, (6) e_{yy} = 0.1249, (7) e_{yy} = 0.1283, (8) e_{yy} = 0.1298 and (9) e_{yy} = 0.1303, respectively. The banded regions with high strain rate shown as red color indicates the PLC bands.

2.3.4 Correlation between serration behavior and PLC band propagation

Figure 2.14 (a) shows the change of the average strain rate in the gage part (blue curve) together with the whole nominal stress-strain curve (black curve). The average strain rate was calculated from the DIC strain-rate maps and plotted as a function of the time of the measurement which was accurately synchronized between the tensile test and the DIC analysis for the identical specimen. Corresponding nominal strains are also indicated along the upper x-axis. The average strain rate in the gage part significantly fluctuated and the time interval between each

fluctuation became larger with progressing the deformation.   It was noteworthy that the interval

of serration peaks on the stress-strain curves also became larger with the progress of the tensile

deformation, which suggested a close correlation between the fluctuation of the average strain rate

and the serration behavior on the global stress-strain curve.

In order to investigate the relationship between the serration and the average strain rate in

more detail, the changes of the nominal stress and the average strain rate in the experimental time

from 230 s to 290 s, corresponding to the period indicated by a red broken-line square in **Fig. 2.14**

(a), were magnified and exhibited in **Fig. 2.14 (b)**.   In **Fig. 2.14 (b)**, thin dotted lines are drawn at

the experimental times when the serration peaks appeared.   It was clearly found that the serration

peaks corresponded well with the local minima of the average strain rate of the gage part.   When

the average strain rate quickly increased from the local minimum, the flow stress quickly dropped

from the serration peak.

The points (1) ~ (9) marked on the stress-strain curve in **Fig. 2.14 (b)** corresponded to **Fig.**

2.13 (1) ~ (9), respectively.   Comparing between **Fig. 2.14 (b)** and **Fig. 2.13**, at a serration peak

(the point (1)) in **Fig. 2.14 (b)**, a former PLC band was disappearing and a new band was nucleating

in **Fig. 2.13** (1).   At the points (2) and (3) in **Fig. 2.14 (b)** corresponding to an increase in the flow

stress just after a sharp stress drop from the serration peak, the newly nucleated band was

propagating upward along the gage part in the DIC maps (**Fig. 2.13** (2), (3)).   At the point (4)

where the flow stress was about to increase, the band was disappearing at the upper shoulder part

43

in **Fig. 2.13**.   From the point (5) to the point (8) on the stress-strain curve, annihilation, nucleation

and propagation of PLC bands, which were similar to the points (1) ~ (4), were observed in the

local strain-rate maps obtained by DIC (**Fig. 2.13**).   Annihilation of the former PLC band and

nucleation of the new band shown in **Fig. 2.13** (9) corresponded well again to the serration peak at

the point (9) in **Fig. 2.14 (b)**.   That is, it was clearly shown that the serration behavior appeared

on the stress-strain curve perfectly corresponded with the formation, propagation and annihilation

of PLC bands, i.e., localized deformation in the gage part.   Thus, the fluctuation of the average

strain rate in the gage part shown in **Fig. 2.14 (b)** also synchronized with the behavior of PLC bands.

We can conclude now that PLC banding determines the global mechanical response of the material

appearing as the serration behavior on the stress-strain curve.
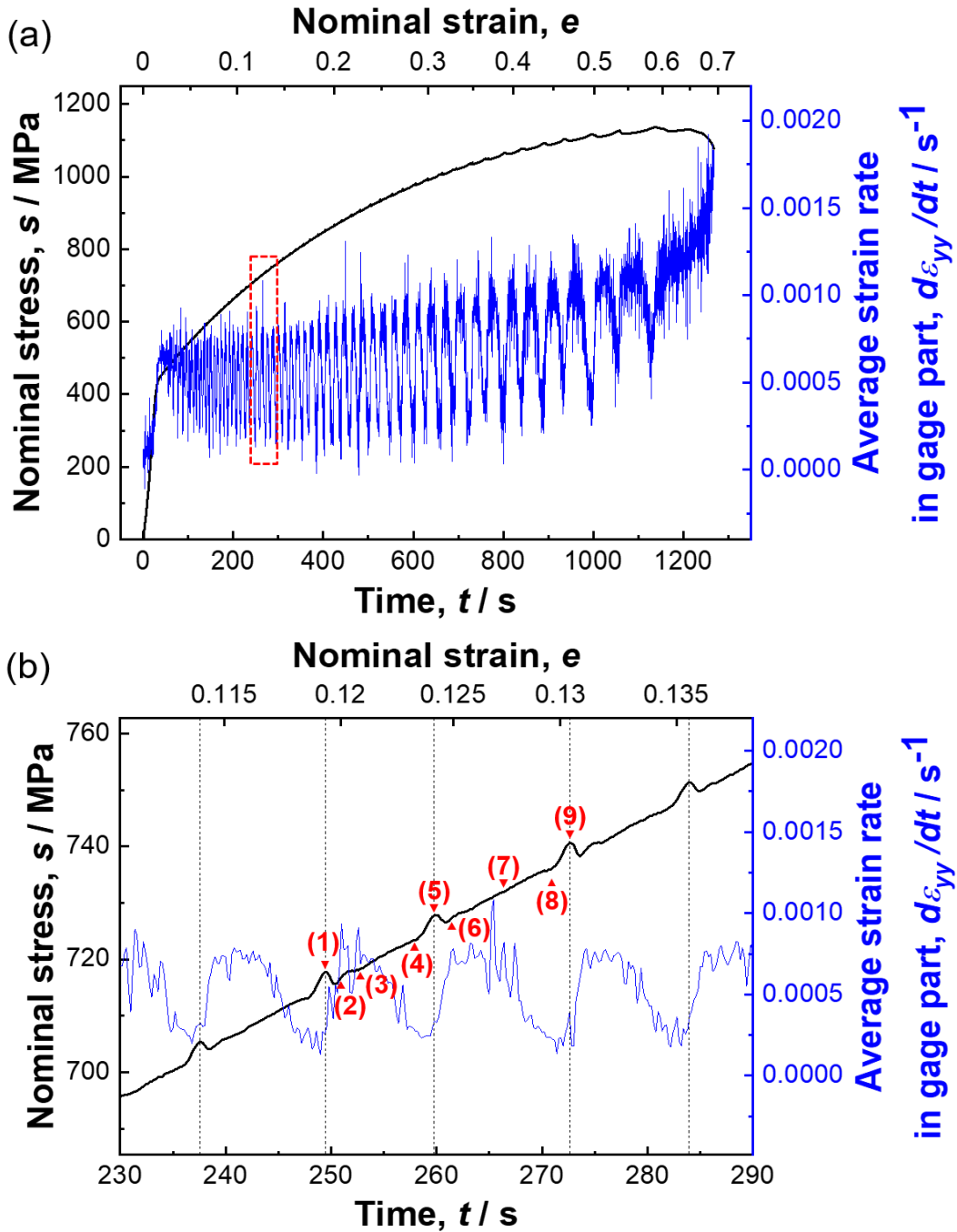
Fig. 2.14 (a) Change of the average strain rate in the gage part and the whole nominal stress-strain curve. The average strain rate was calculated from the DIC strain-rate maps and plotted as a function of the time of the measurement. Corresponding nominal strains are also indicated along the upper x-axis. (b) Changes of the nominal stress and the average strain rate in the experimental time range from 230 s to 290 s, indicated by a red-dashed square in **Fig.2.14 (a)**. Thin dotted lines are drawn at the experimental times when the serration peaks appeared. The points (1) ~ (9) marked by red triangles on the stress-strain curve correspond to the DIC images shown in **Fig.2.13** (1) ~ (9), respectively.

2.3.5 Changes in local strain and local strain-rate correlating to PLC band propagation

The strain rate shown and discussed in **Fig. 2.14** was the average of the gage part obtained

from the DIC data. However, the actual deformation in the gage part was heterogeneous

(localized), as was shown in **Fig. 2.13**. Then, deformation behavior at a local point was analyzed

from the DIC data. As represented in the image inserted in **Figure 2.15 (a)**, a point in the gage

part was set in the DIC maps, and changes of the local strain (ε_{yy}) and the local strain rate ($d\varepsilon_{yy}/dt$)

at this point were plotted in red and blue colors, respectively, in **Fig. 2.15 (a)** as a function of the

experimental time. Interestingly, the strain at the analyzed point (red curve) increased in a

stepwise manner, and the time interval between neighboring steps and the increment of strain at

each step both increased with increasing the experimental time (i.e., the global tensile strain). The

local strain rate at the analyzed point stayed in a very low value in most periods, but periodically

showed sharp peaks. The peak of the local strain rate corresponded to the time at which a PLC

band with high strain rates was just propagating at the analyzed point. As a result, the sudden

increases in the local strain corresponded with the strain rate peaks. Both the time interval

between the peaks and the maximum strain rate at the peak increased with increasing the

experimental time (the tensile strain).

In order to investigate the development of the local strain and the local strain rate with the

experimental time in more detail, the graph in a range from 210 s to 300 s of the experimental time

was enlarged in **Fig. 2.15 (b)**. The time ranges of the local strain-rate peaks, which corresponded

to the durations when each PLC band was passing through the analyzed point, are distinguished by black-dashed lines in **Fig. 2.15 (b)**. It was clearly shown that the sudden increases in the local strain perfectly coincided with the short durations of the strain-rate peaks, which meant that the strain at a certain local point increased drastically when a PLC band was passing through the point. On the other hand, increases of the local strain at the analyzed point between neighboring steps in the red curve of **Fig. 2.15 (b)** were quite small, during which no PLC band was overlapped at the analyzed point. The results clearly demonstrated that most of the plastic deformation within the gage part of the tensile specimen was given within the PLC bands
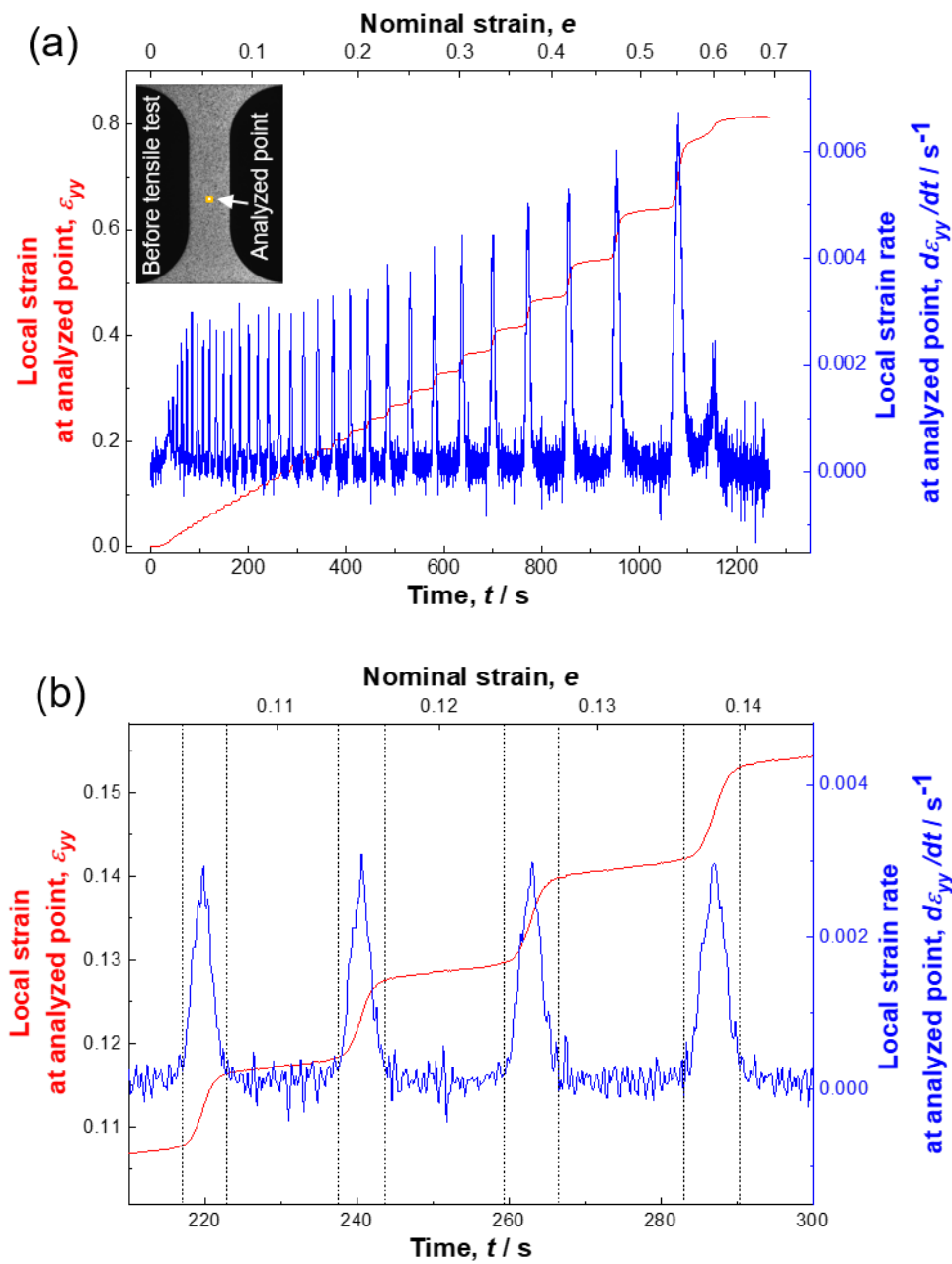
Fig. 2.15 Changes of the local strain (red) and strain rate (blue) at a certain point set in the gage part of the DIC maps, plotted as a function of experimental time. Corresponding global nominal strain is also indicated. (b) Enlarged profiles of the local strain (red) and strain rate (blue) from 210 s to 300 s of the experimental time. The time areas of the local strain-rate peaks are distinguished by black-dashed lines.

2.3.6 Development of plastic deformation within the gage part

Features of the localized deformation (PLC banding) in the present 22Mn-0.6C steel specimen and its correlation to the serration behavior on the global stress-strain curve were demonstrated above. Here the author would like to show how plastic deformation develops within the gage part of the 22Mn-0.6C specimen, again by the use of the DIC analysis. **Figure 2.16** shows DIC local strain maps demonstrating changes of local strain distributions (ε_{yy}) within the gage part during the deformation period from (1) to (9) shown in **Fig. 2.13** and **Fig. 2.14 (b)**. Local strain maps of **Fig. 2.16** (1) ~ (9) corresponded to one cycle of nucleation, propagation and annihilation of PLC bands shown in **Fig. 2.13** (1) ~ (9), respectively. In order to exhibit the change of local strain distributions obviously, a small strain scale from ε_{yy}=0.11 to ε_{yy}=0.14 was used in **Fig. 2.16**, and the magnitude of local strain was expressed in different colors according to the key color bar inserted in the figure. The areas surrounded by white-dashed lines in **Fig. 2.16** are the positions of PLC bands observed in **Fig. 2.13**. From (1) to (4) in **Fig. 2.16**, local strains in the upper side of the gage part became higher than the lower part, which corresponded to the PLC band propagation swept from the center to the upper side (**Fig. 2.13** (1) ~ (4)). At (5) where the PLC band annihilated in the upper shoulder part, strain distributions were heterogeneous and showed a clear contrast between the upper part with higher strains and lower part with lower strains in the gage. From (5) to (8) in **Fig. 2.16**, the strain in the lower side increased in this turn, corresponding to the downward propagation of the new PLC band from the center to the lower part.

Then the strain distribution in the gage part became fairly homogeneous in (8) and (9) after one cycle of PLC band sweeping. Besides the strain range investigated in **Fig. 2.16**, such processes during the tensile deformation was observed in the entire deformation.
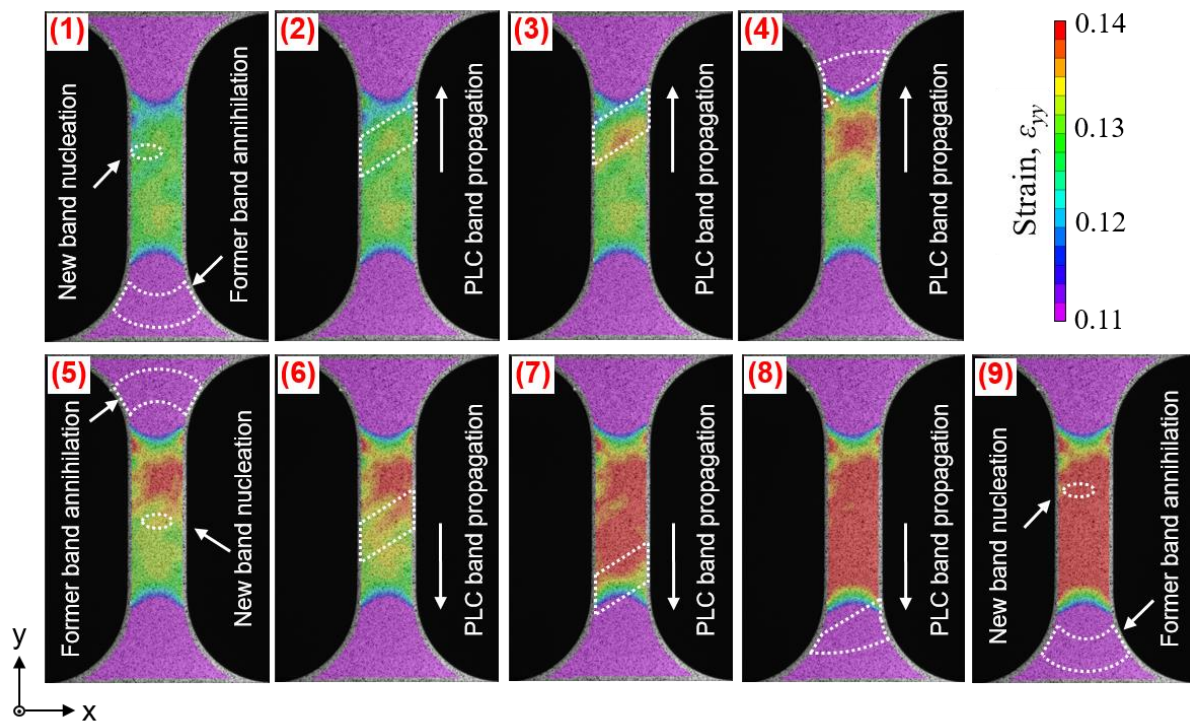
Fig. 2.16 DIC local strain maps captured at different engineering tensile strains (e_{yy}), corresponding to one cycle of PLC band propagation. (1) e_{yy} = 0.1193, (2) e_{yy} = 0.1199, (3) e_{yy} = 0.1210, (4) e_{yy} = 0.1236, (5) e_{yy} = 0.1241, (6) e_{yy} = 0.1249, (7) e_{yy} = 0.1283, (8) e_{yy} = 0.1298 and (9) e_{yy} = 0.1303, respectively. (1) ~ (9) exactly corresponded to the local strain-rate maps shown in **Fig.2.13**. Positions where PLC bands were observed in corresponding strain-rate maps (**Fig.2.13**) are marked by white-dashed lines. Magnitude of local strain was expressed in different colors according to the key color bar inserted in the figure.

2.3.7 Deformation microstructure at early stage of tensile test

The results obtained from the DIC analysis clarified that the serration behavior in the present 22Mn-0.6C steel perfectly corresponded with the heterogeneous deformation in the form of PLC banding.   As was introduced in the section 1.2, all the reports regarding the serration behavior (or DSA effect) in high-Mn austenitic steels tried to explain the phenomena from the view point of the interaction between partial dislocation(s) and interstitial carbon atoms.   However, the serration behavior was also frequently found in other FCC alloys.   Some of those FCC alloys did not contain either deformation-induced planar faults, e.g. transformation-induced plasticity (TRIP) steels [32], nor interstitial atoms, e.g. high-entropy alloys [33] and Cu-Zn alloys [34].   Al-Mg alloys [26,35,36] did not even contain both the deformation-induced planar faults and interstitial atoms, but showed the serration behavior.   Therefore, in the current section, deformation microstructures were observed by using ECCI technique, for understanding what caused the heterogeneous deformation in the present 22Mn-0.6C steel.

Figure 2.17 (a) shows the stress-strain curve of the interrupted tensile test for observing the deformation microstructures at early stage of deformation.   The unloading point was indicated by a red dot, and the enlarged curve was inset in the graph.   The strain at unloading was 0.023, and the corresponding stress was 460 MPa.   Before unloading the tensile specimen, two serration peaks were found.   **Fig. 2.17 (b)** shows the strain-rate distributions at the point of unloading (red dot in **Fig. 2.17 (a)**).   A PLC band was propagating to the left at this point, and the microstructure

observations were carried out depending on the PLC band position: ① the region where PLC band has not yet swept, ② the region where PLC band was sweeping, and ③ the region where PLC band finished sweeping.　In each region (①~③), 25 grains were observed by ECCI technique (total 75 grains).　**Fig. 2.17 (c)** shows the representative ECCI microstructures in the regions of ①, ② and ③.　For all three images, large number of dislocations were found even at the early stage of deformation (e=0.023), forming cell structures with wavy morphologies.　As the PLC band propagated (③→②→①), the number of dislocations significantly increased, and it was consistent with the increase of the strain with PLC banding, as shown in **Fig. 2.15 (b)**.　It should be noted that deformation twins or stacking faults were rarely found in all the regions of ①, ② and ③ even after the serration behavior has already started (two serration peaks in **Fig. 2.17 (a)**). Zhi et al. [37] reported that deformation twin fraction of the 22Mn-0.6C steel was close to 0 % before $\varepsilon = 0.05$, and deformation twin started to form at around $\varepsilon = 0.06$ and the deformation twin fraction reached 19 % at $\varepsilon = 0.35$.　The results strongly indicate that the serration (or DSA effect) of the present material was not caused by planar faults, but caused by dislocations.
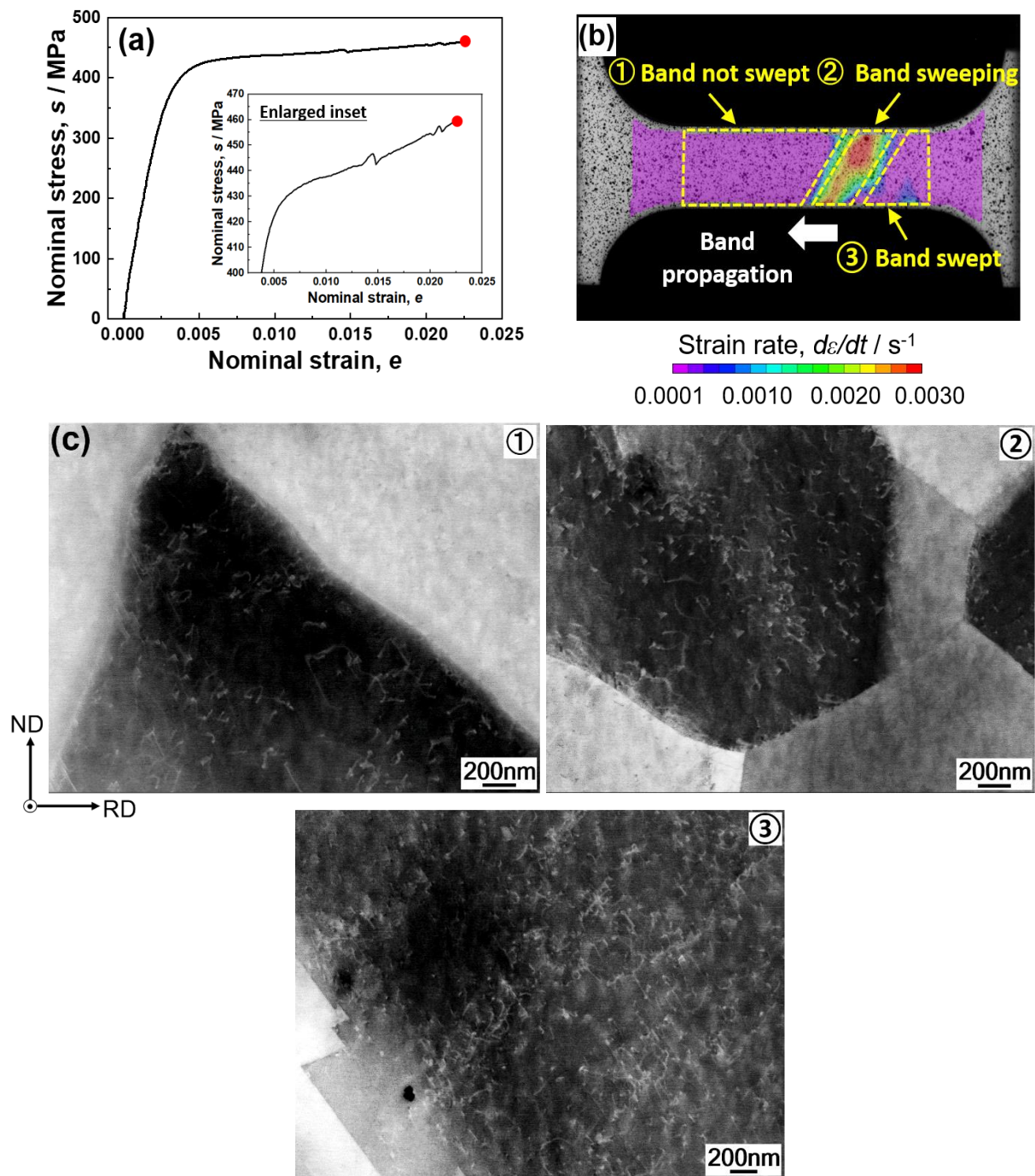
Fig. 2.17 (a) Tensile test was interrupted at (*e*=0.023, *s*=460 MPa) for microstructure observation. The enlarged curve was inset in the graph. (b) Strain-rate distribution at the point of unloading (red dot in **Fig. 2.17 (a)**). (c) Representative ECCI microstructures in the regions of ①, ② and ③ (**Fig. 2.17 (b)**).

2.3.8 The role of PLC band on global mechanical properties revealed by *in-situ* synchrotron XRD measurement

In the previous chapters, we found out that the serration behavior of the present material perfectly matched with the localized deformation characterized as PLC banding, and dislocations were generated within the PLC banding.   Next, in the current section, the *in-situ* synchrotron XRD measurement was also applied during the tensile deformation, for correlating the heterogeneous deformation clarified above with material parameters.   The *in-situ* XRD measurement can precisely reveal the changes of both dislocation densities evaluated from the peak broadening and elastic strain calculated from the peak shift, synchronizing with the physical PLC band propagation in the tensile specimen.

The results obtained from the *in-situ* XRD measurement during the tensile test are shown in **Figure 2.18**.   As was described in the section 2.2.5, a focused X-ray beam was irradiated on a center position in the gage part of the tensile specimen.   In **Fig. 2.18 (a)**, the whole diffraction profiles at two different stress levels of 0 MPa (before the tensile deformation) and 1000 MPa are shown on the left side, and (200) peaks at two stress levels are enlarged and shown on the right side.   The (200) peak was selected for the peak-shift analysis because the (200) peak showed high intensity and its peak shift was the largest among all diffraction peaks due to the lowest elastic modulus along <100> direction in FCC metals and alloy, which would be shown in the section 2.3.9.   A sharp diffraction profile of (200) plane was recognized before the deformation (at 0 MPa).

Both peak broadening and peak shift were clearly found at the stress level of 1000 MPa, which were the results of accumulation of lattice defects and elastic deformation of crystal lattices, respectively.   It has been reported that dislocations and planar faults contribute to the peak broadening, where diffraction angles are scattered due to local lattice distortion [38,39].   Considering that most of (both annealing and deformation) twin boundaries in FCC materials are composed of perfectly coherent $\{111\}\sum 3$ CSL boundaries, the lattice distortion produced by twin boundaries is thought to be small except for the areas near remaining leading partial dislocations or incoherent portions of twin boundaries.   Balogh, Ribárik, and Ungára [39] simulated the diffraction profile of nanocrystalline pure copper by using convolutional multiple whole profile (CMWP) method.   Based on the theoretically obtained profile functions, they fitted the experimentally obtained diffraction profile.   In their simulation, intrinsic/extrinsic stacking faults and twin boundaries caused a peak broadening at the bottom part of a diffraction peak.   In the present study, we calculated the dislocation density by using Williamson-Hall method, where FWHM of diffraction peaks (not the bottom part of diffraction peaks) were concerned.   Therefore, the peak broadening caused by planar faults (deformation twin boundaries and stacking faults) would not be significant in determining the FWHM, so that it was assumed in the present study that the most of the peak broadening resulted from accumulated dislocations.   The dislocation density (ρ) during the tensile test was calculated from the peak position and FWHM of (111), (200), (311) and (222) peaks at different experimental times by the use of the Williamson-Hall equation

[40],

$$\frac{\Delta 2\theta \cos\theta}{\lambda} = \frac{0.9}{D} + 2\varepsilon\frac{\sin\theta}{\lambda} \qquad (2.5)$$

$$\rho = 16.1\left(\frac{\varepsilon}{b}\right)^2 \qquad (2.6)$$

where θ is the diffraction angle of a peak, $\Delta 2\theta$ is FWHM of the peak, λ is the wavelength of the incident X-ray beam (0.0413 nm), D is a crystallite size, ε is a heterogeneous strain, and b is the magnitude of Burgers vector (0.2552 nm in the present material), respectively. From the equation (2.5), when taking $2\frac{\sin\theta}{\lambda}$ as the x-axis and $\frac{\Delta 2\theta \cos\theta}{\lambda}$ as the y-axis, the slope of the data plots corresponds to ε. By putting ε into the equation (2.6), the dislocation density (ρ) is obtained.

In order to also evaluate the evolution of elastic strain, the change of the lattice strain during tensile deformation was calculated. The lattice strain of *hkl* plane (ε^{hkl}) under loading is calculated from the change in the interval of the lattice plane corresponding to the concerning diffraction peak, as:

$$\varepsilon^{hkl} = \frac{d^{hkl} - d_0^{hkl}}{d_0^{hkl}} \qquad (2.7)$$

where d^{hkl} is the interval of *hkl* plane calculated from the *hkl* diffraction peak, and d_0^{hkl} is the initial interval of *hkl* plane under 0 MPa of tensile stress. As mentioned in the previous paragraph, the elastic modulus of (200) plane was the lowest in FCC metals and alloy. Therefore, by selecting the lattice strain of (200) plane (ε^{200}) for the analysis, it is possible to capture even small changes

in elastic strain. The term of the lattice strain hereafter in this paper refers to the lattice strain of (200) plane.

Changes in the dislocation density and the lattice strain during tensile deformation of the present 22Mn-0.6C specimen obtained from the *in-situ* XRD measurement are shown as a function of the experimental time in **Fig. 2.18 (b)**, together with the nominal stress curve. It should be noted that the nominal stress showed the global deformation response in the tensile deformation, whereas the lattice strain and the dislocation density revealed the local deformation response obtained from the limited area of 0.5 mm × 0.2 mm where the XRD beam was irradiated, as was described in the section 2.2.5.

In the lattice strain-time curve (red line) in **Fig. 2.18 (b)**, the lattice strain increased with the experimental time in most periods. Interestingly, however, the lattice strain dropped periodically, which indicated that periodical stress relaxation occurred at the local XRD beam position. Both the time interval between neighboring drops and the decrement of the lattice strain increased with increasing the experimental time, i.e., with the progress of the tensile deformation.

The dislocation density-time curve (blue line) in **Fig. 2.18 (b)** did not show a continuous increase, but increased in a stepwise manner. During the most periods, the dislocation density at the XRD beam position did not increase significantly, but it suddenly increased at certain experimental times. In addition, both the time interval between neighboring steps increases and the increment of dislocation density at each step increased with increasing the experimental time,

i.e., with the progress of the tensile deformation.   The dislocation density increased up to 5×10^{16} m^{-2} till the macroscopic fracture.   The high dislocation density might be overestimated somehow, because the peak broadening was evaluated, considering only contribution from dislocations as was described above.

In order to look into the discontinuous changes in the lattice strain and the dislocation density at the XRD beam position, the graph in a time range from 600 s to 850 s is enlarged in **Fig. 2.18 (c)**.   Thin broken lines are drawn in **Fig. 2.18 (c)** at the experimental times when serration peaks appeared on the flow stress curve (black).   Different marks are used to show the positions of serration peaks (▼A~▼E), peaks of the lattice strain (▼), drops of the lattice strain (△), and sudden increases of the dislocation density (△), respectively.   On the lattice strain curve (red) in **Fig. 2.17 (c)**, the peaks of the lattice strain (▼) coincided well with the serration peaks (▼A~▼E). As was explained in the section 2.3.4 (**Figs. 2.13** and **2.14**), the serration peak appeared when PLC bands disappeared from the gage part.   In addition, it was figured out in the section 2.3.6 (**Figs. 2.13** and **2.15**) that most of the plastic deformation was given within the PLC bands.   Therefore, at the serration peaks when PLC bands disappeared, the whole gage part of the tensile specimen was considered to be deformed more elastically with small amounts of plastic deformation.   This is the reason why the lattice (elastic) strain at the local XRD beam position showed the peaks (▼) at the same timing of the serration peaks (▼).

On the lattice strain curve (red) and the dislocation density curve (blue) in **Fig. 2.17 (c)**, the

drops of the lattice strain (△) and the sudden increases of the dislocation density (△) synchronized to each other.   Interestingly, the drops (with local minima) of the lattice strain (△) were found only after the serration peaks of ▼A, ▼C, and ▼E, but the drops (with local minima) of the lattice strain did not appear after the serration peaks of ▼B and ▼D.   As was mentioned in the section 2.3.3 (**Fig. 2.13**), the PLC bands in the present high-Mn steel sometimes formed near the gage center, propagated upward or downward, and disappeared at one side of shoulder part.   Then new PLC bands nucleated at the center, propagated to the opposite direction of the former PLC band (downward or upward), and disappeared.   It should be noted that the tensile specimen used in the present *in-situ* XRD measurement was elongated upward with its bottom grip part fixed, while the XRD beam position was fixed.   In the experimental time range from 600 s to 850 s shown in **Fig. 2.18 (c)**, the tensile specimen was already elongated much, so that the XRD beam position was located in the lower half of the gage part.   In this time range, the PLC band nucleated from the center and propagated upward never passed through the XRD beam position, but the next PLC band nucleated from the center and propagated downward passed through the beam position.   Therefore, the drops of the lattice strain (△) and the sudden increases of the dislocation density (△) observed at every other serration peak (i.e., after ▼A, ▼C, and ▼E) are considered to correspond to the PLC bands nucleated at the center and propagated downward that can pass through the XRD beam position located at a relatively lower part of the gage.   That is, the drops of the lattice strain (△) correspond to the passage of PLC bands on the beam position.   Since

59

plastic deformation is localized within the PLC band, the passage of the PLC band relaxes elastic stress, resulting in the drop of the lattice (elastic) strain at the X-ray beam position by plastic deformation.
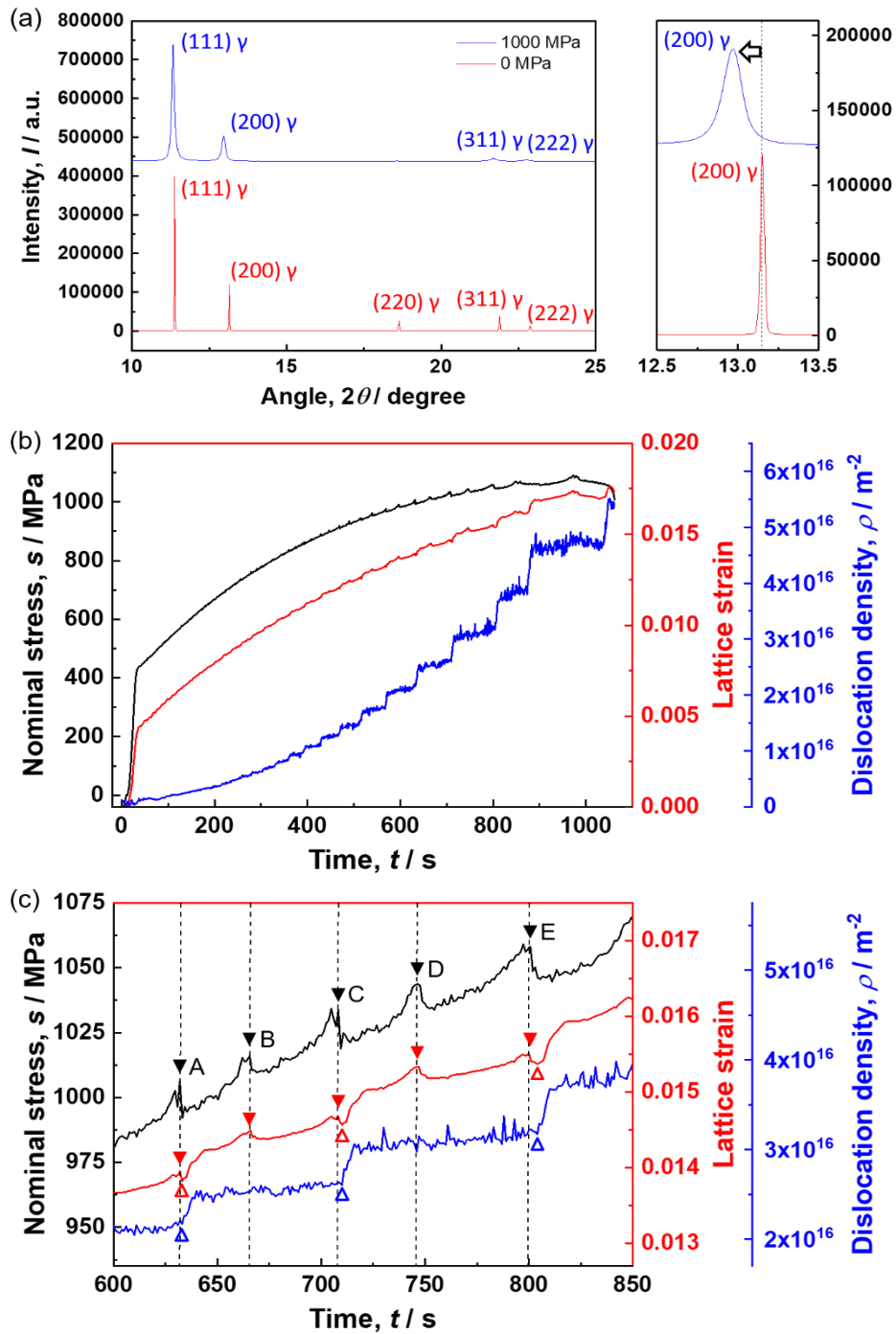
Fig. 2.18 (a) The whole angular diffraction profiles at 0 MPa and 1000 MPa, and enlarged (200) peaks at two stress levels are shown on the left and right side, respectively. A black dashed line in the right figure is drawn to indicate the center of the (200) peak at 0 MPa, and an arrow indicates the peak shift to lower angle at 1000 MPa. (b) The changes of nominal stress (black, left y-axis), lattice strain (red, the first right y-axis), and dislocation density (blue, the second right y-axis) are shown as a function of the experimental time. (c) Curves in the time range from 600 s to 850 s, enlarged from (b). Serration peaks are indicated by thin broken lines. Serration peaks (▼A~▼E), peaks of lattice strain (▼), drops of lattice strain (△), and sudden increases of dislocation density (△) are indicated on the curves.

In high-Mn austenitic steels, deformation twining was known to be an extra deformation mechanism besides dislocation glide. However, it is considered that the contribution of deformation twinning to plastic deformation (plastic tensile strain) was not dominant. As shown in **Figure 2.19**, when a leading partial dislocation glides on every (111) plane in FCC material, i.e. deformation twinning, resulting theoretical shear strain (γ) is calculated as,

$$\gamma = \frac{|\vec{b}_{leading\ partial}|}{d_{111}} = 0.707 \tag{2.8}$$

where $|\vec{b}_{leading\ partial}|$ is the size of Burgers vector of the leading partial dislocation and d_{111} is the interval of (111) planes. The shear strain calculated in the Eq. (2.8) should be converted into the tensile strain, considering the effect of crystallographic orientation additionally. In Taylor model for uniaxial tensile test, the tensile strain in unit volume is expressed as,

$$d\varepsilon_x = \frac{1}{M} \times \sum_{slip\ system} d\gamma \tag{2.9}$$

where, $d\varepsilon_x$ is the tensile strain in unit volume, $\sum_{slip\ system} d\gamma$ is the sum of shear strain on each slip plane in unit volume, and M is the Taylor factor. Taylor factor in FCC material with random texture is known to be 3.06, and the present material did not have any strong textures as was shown in **Fig. 2.11 (c)**. Considering $\sum_{slip\ system} d\gamma$ as the theoretical shear strain given by deformation twinning (expressed in Eq.(2.8)), therefore, the tensile strain produced by deformation twinning is estimated to be 0.231. In **Fig. 2.16 (c)**, the dislocation densities were intensively investigated in a time range from 600 s to 850 s, and this time range corresponded to a true strain range from 0.25

to 0.33.　The volume fraction of deformation twins in 22Mn-0.6C steel was reported to be around

13 % at true strain of 0.25 and 19 % at true strain of 0.33, respectively [37].　In the literature of

[37], the grain size was 4.9 μm (including annealing twin boundaries).　It has been reported that

the formation of deformation twins is suppressed by grain refinement in high-Mn austenitic steels

[41].　Because the 22Mn-0.6C steel used in the present study had an average grain size of 2.0 μm

(including annealing twin boundaries), the deformation twins in the present study were expected to

be less formed than the deformation twins in the literature of [37] in the same strain range.

Considering the volume fraction of deformation twins reported in [37], it can be roughly estimated

that the tensile strains produced by deformation twinning are smaller than 0.030 at $\varepsilon = 0.25$ and

0.043 at $\varepsilon = 0.33$, respectively.　Here, the increment of true strain (tensile strain) was 0.08 (=0.33

– 0.25), and the tensile strain produced by deformation twinning within this true strain range was

0.013 (= 0.043 – 0030).　This calculation indicates that the contribution of deformation twinning

to tensile strain was smaller than 16.3 % (= 0.013/0.08 x 100) within the true strain range from 0.25

to 0.33 in the present material.　Even though deformation twins somehow contribute to plastic

deformation as an extra deformation mechanism, the tensile strain within the PLC band is

considered to be given mostly by glides of many dislocations, resulting in the sudden increase of

the dislocation density (△) at the X-ray beam position.　The synchronized changes of the flow

stress, lattice strain, and dislocation density found in **Fig. 2.16 (c)** could be consistently understood

in such a way.
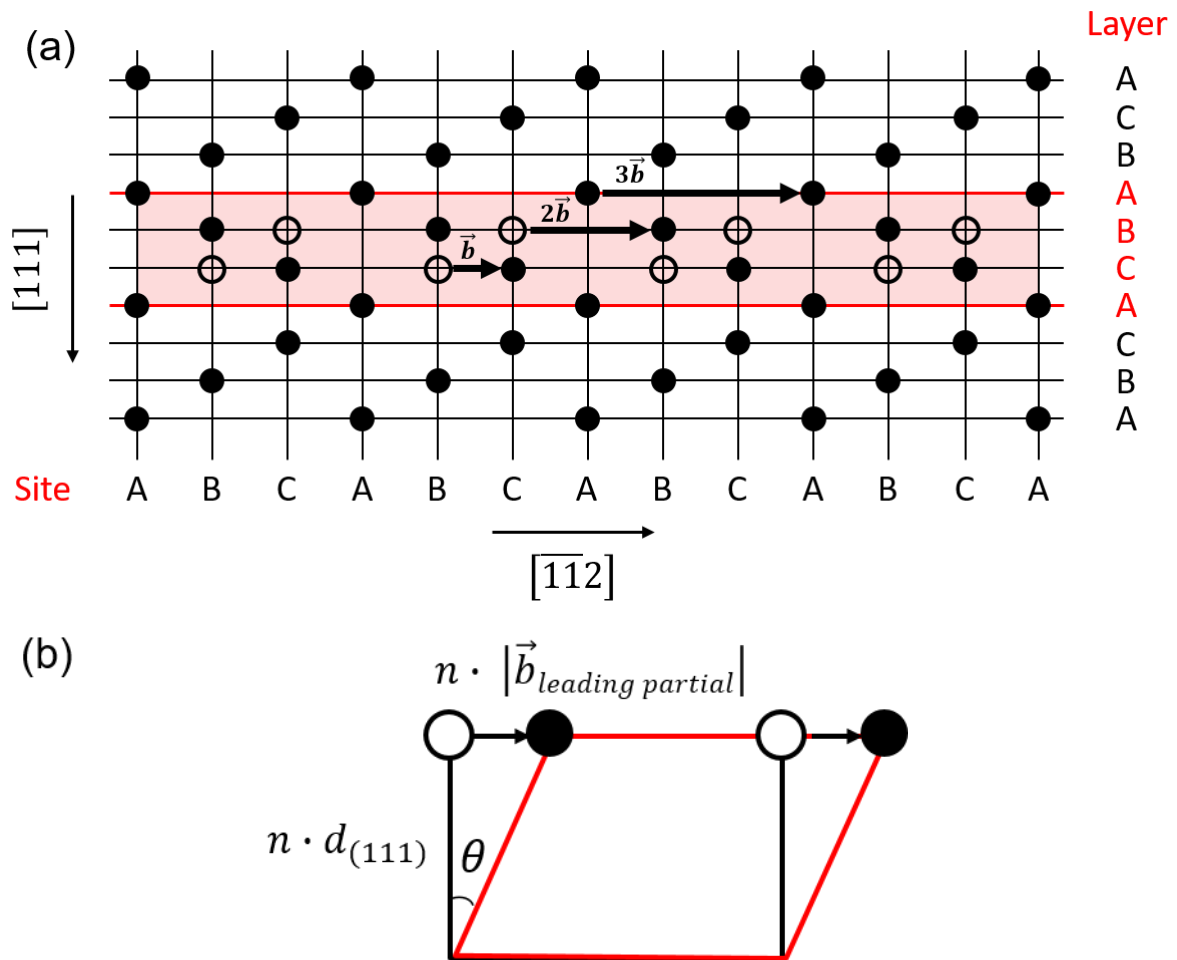
Fig. 2.19 (a) The schematic illustration of deformation twinning. A leading partial dislocation glides on every (111) plane, and the consequent twinned area is indicated as red color. (b) Shear deformation when n layers are within the twinned area.

The results obtained from the *in-situ* synchrotron XRD diffraction during the tensile test could give us the changes of material parameters in the local X-ray beam position, which consistently synchronized with the passage of the PLC band as well as the serration on the macroscopic flow stress curve. It is noteworthy that the dislocation density at the beam position significantly increased around the drops of the lattice strain ($\triangle$), i.e., the passage of PLC bands, as

shown in **Fig. 2.18 (c)**.   This suggests that a large strain-hardening by an increase of the

dislocation density locally occurs within the propagating PLC band, and it corresponds to the period

between serration peaks (i.e., the local stress maxima) on the global stress-strain curve.   The quick

strain-hardening (i.e., the quick increase in the local dislocation density right after $\triangle$) results in the

large increases of the local lattice strain right after $\triangle$ at A, C, and E in **Fig. 2.18 (c)**, because the

local region becomes more difficult to be plastically deformed by hardening.

2.3.9 Quantification of stress relaxation and work-hardening by PLC banding

It was clarified that the serration behavior on the global stress-strain curve in the high-Mn

austenitic steel perfectly corresponded to the local heterogeneous deformation characterized by the

formation, propagation and annihilation of PLC bands.   In addition, the heterogeneous

deformation in a mesoscopic scale with the local material parameters, i.e., the dislocation density

and the lattice strain in the beam position, was successfully correlated.   Elastic strain (thus stress)

was found to decrease within the PLC band, i.e., stress relaxation within the PLC band, and the

elastic strain in the region where the PLC band has swept significantly increased due to the sudden

increase of the dislocation density, i.e., work-hardening after the passage of the PLC band.   In the

current section, the stress relaxation and work-hardening induced by PLC banding would be

quantified.

The nominal stress-lattice strain curves obtained from the *in-situ* neutron beam diffraction

measurement during tensile test are shown in **Figure 2.20**.   Diffraction profiles at the five stress

levels within the elastic region (10, 90, 180, 270 and 360 MPa) were investigated.   As was

discussed in the section 2.2.6, TOF was converted into the interval of each *hkl* plane, and the lattice

strain of each (*hkl*) plane was calculated by using Eq. (2.7).   As shown in **Fig. 2.20**, fairly good

linear relationship between lattice strain and nominal stress was obtained in each (*hkl*) plane, and

the elastic modulus of each plane (E_{hkl}) was obtained from the slope of each line.   The obtained

E_{hkl} is summarized in the **Table 2.2**.   As mentioned in the section 2.3.8, it was confirmed that

E_{200} had the lowest elastic modulus among the first five Bragg reflections having high intensities.

By selecting the lattice strain of (200) plane, therefore, it was possible to capture the small change

of lattice strain (thus stress) with the PLC banding (**Fig. 2.18 (b) and (c)**).
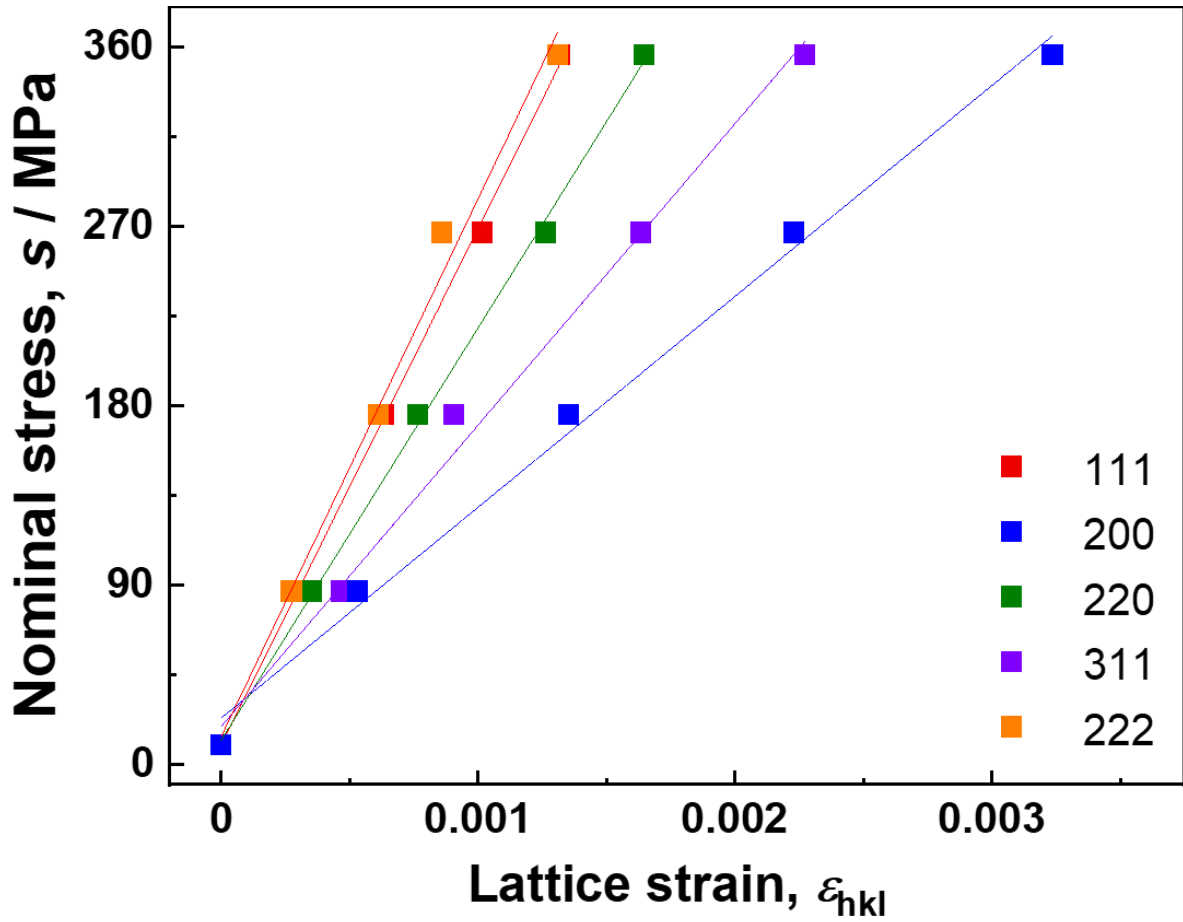
Fig. 2.20 The nominal stress-lattice strain curves obtained from the *in-situ* neutron beam diffraction measurements during tensile tests. Investigated stress levels were 10, 90, 180, 270 and 360 MPa within the elastic region, and the data points of each (*hkl*) were fitted linearly.

Table 2.2 The E_{hkl} of the 22Mn-0.6C steel (GPa).

E_{111}	E_{200}	E_{220}	E_{311}	E_{222}
259.1	105.8	206.9	151.2	269.8

From the experimentally obtained elastic modulus and elastic strain, stress can be calculated as follows,

$$\sigma_{hkl} = E_{hkl} \cdot \varepsilon_{hkl} \tag{2.10}$$

67

where, σ_{hkl} is the stress of (hkl) plane, E_{hkl} is elastic modulus of (hkl) plane, ε_{hkl} is elastic strain of (hkl) plane. Here, because ε_{200} was already obtained in the section 2.3.8 and E_{200} was calculated in the current section, stress (σ_{200}) can be be calculated by using these experimentally obtained values. However, it should be noted that the ε_{200} obtained from *in-situ* synchrotron XRD measurement formed the Bragg angle of θ to the tensile direction (TD), so the σ_{200} also formed the θ to the TD, as described in **Figure. 2.21 (a)**. In order to quantify the local stress relaxation and work-hardening with PLC banding along the TD, the σ_{200} should be converted to tensile stress. **Figure. 2.21 (b)** shows the Mohr circle in uniaxial tensile test. Mohr circle graphically determines the stress components (normal and shear stresses) acting on an arbitrary plane. Horizontal axis corresponds to normal stress, and vertical axis corresponds shear stress. Note that the angle between two different planes (θ) is drawn as double angle (2θ) in the Mohr circle. Here, it was assumed that tensile, transverse and normal directions of the tensile specimen were x_1, x_2 and x_3 of principal axes of the stress, respectively, and the principal stresses applied to transverse and normal directions were assumed to be zero ($\sigma_2 = \sigma_3 = 0$) in the uniaxial tensile test. By using the Mohr circle, the relation between a normal stress on an arbitrary plane (σ_{hkl}) and tensile stress (σ_1) can be described as follows,

$$R(1 + \cos 2\theta) = \sigma_{hkl} \tag{2.11}$$

$$\sigma_1 = 2R = 2 \cdot \frac{\sigma_{hkl}}{1 + \cos 2\theta} \tag{2.12}$$

where R is radius of the Mohr circle, θ is the angle between the arbitrary plane and principal

plane, which is drawn as double angle (2θ) in the Mohr circle, σ_{hkl} is the normal stress applied

on (hkl) plane and σ_1 is the tensile stress (a principal stress).   Since σ_{200} was calculated from

the Eq. (2.10) and θ was the Bragg angle of the (200) plane in the synchrotron XRD beam

measurement, tensile stress (σ_1) at the local XRD beam position was calculated from Eq. (2.12).
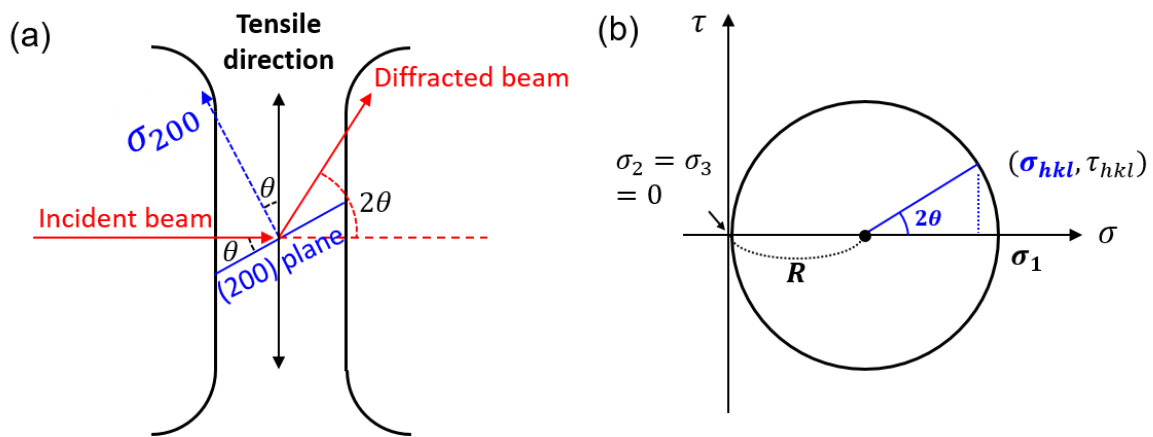
Fig. 2.21 (a) Schematic illustration describing $\boldsymbol{\sigma_{200}}$ forming Bragg angle of $\boldsymbol{\theta}$ to the tensile direction. (b) Mohr circle in uniaxial tensile test, where $\boldsymbol{\sigma_2 = \sigma_3 = 0}$ and $\boldsymbol{\sigma_1}$ is tensile stress. Horizontal and vertical axes correspond to normal stress and shear stress, respectively. $\boldsymbol{R}$ is radius of the Mohr circle, and $\boldsymbol{\theta}$ is the angle between the arbitrary plane and principal plane, which is drawn as double angle ($\boldsymbol{2\theta}$) in the Mohr circle.

Figure. 2.22 (a) shows the change of local stress (red), the dislocation density (blue) and

the global true stress* (black) of the present 22Mn-0.6C specimen as a function of the experimental

time.   The local stress was the tensile stress (σ_1) at the XRD beam position, which was calculated

from Eq. (2.12), and dislocation density was the same value obtained in the section 2.3.8.   Global

true stress* was calculated from the displacement of a cross-head, i.e. displacement of both gage

part and grip part. Considering that the grip part rarely deformed but its length was additionally included in initial length before deformation, the nominal strain ($e*$) calculated from the displacement of a cross-head was smaller than the nominal strain when only displacement of the gage part was concerned. Consequently, the global true stress*, which was calculated from $(1 + e*) \cdot \sigma_{nominal}$, was also smaller than the true stress when only displacement of the gage part was concerned. The smaller value of the global true stress*, as compared to the local stress over the entire deformation in **Fig. 2.22 (a)** can be understood in such a way. However, the global true stress of the present specimen obtained by using extensometer in DIC analysis, as shown in **Fig. 2.12 (b)**, was fairly similar with the local stress obtained in the present experiment. The maximum value of the global true stress was 1870 MPa (see **Fig. 2.12 (b)**) and that of the local stress was 1887 MPa (see **Fig. 2.22 (a)**). Those similar values indicated that the local stress calculated from Eq. (2.12) was precise. It is also notable that the entire curvature of the local stress curve (red) was fairly similar with the global true stress* curve (black). This indicated that global true stress* was naturally the averaged deformation of every local stress in the tensile specimen, including the local stress at the XRD beam position. The local stress at the XRD beam position increased with the experimental time in most periods but dropped periodically, and it was the same tendency of the lattice strain as discussed in the section 2.3.8. The dislocation density (blue) increased in the stepwise manner, and it was also discussed in detail in the section 2.3.8.

For the detailed investigation on the change of the local stress with the PLC banding, the

graph in a time range from 600 s to 850 s is enlarged in **Fig. 2.22 (b)**. Thin broken lines are drawn

at the experimental times when serration peaks appeared on the global true stress* curve (black).

Stress relaxation (σ_{SR}) and work-hardening (σ_{WH}) are indicated by arrows on the local stress curve.

It was discussed in the section 2.3.8 that the peaks of the lattice strain coincided very well with the

serration peaks in the stress-strain curve. As indicated by thin broken lines in **Fig. 2.22 (b)**, the

peaks of local stress also coincided very well with the serration peaks of global true stress*. In

addition, the height of the peaks of local stress and serration peaks of global true stress* was very

similar and only had small difference less than 7.0 MPa in this time range. It indicated that the

whole gage part of the tensile specimen, including the XRD beam position, experienced increase

in stress, i.e., serration peaks, whenever PLC bands disappeared. The stress relaxation (σ_{SR})

induced by passage of PLC band was $\sigma_{SR1} = 13.76$ MPa, $\sigma_{SR2} = 12.52$ MPa, $\sigma_{SR3} = 14.80$

MPa, respectively. Here, it should be noted that the stress relaxation was somehow overestimated.

In this experiment, PLC band annihilated in the shoulder part (shown as the peak of local stress)

and nucleated near the gage center where the XRD beam was irradiated (shown as drop of local

stress). Therefore, the peak of local stress was additionally included in stress relaxation (σ_{SR}), so

the σ_{SR} induced by the passage of PLC band should be smaller than obtained values and it was

probably at a range of several megapascals in this time range. The work-hardening (σ_{WH}) induced

by sudden increase of the dislocation density with the PLC banding was $\sigma_{WH1} = 43.94$ MPa,

$\sigma_{WH2} = 49.61$ MPa, $\sigma_{WH3} = 59.89$ MPa, respectively. Considering that the slope of the local

stress beyond the PLC band was almost flat, the most of work-hardening of the present material was achieved within the PLC band.　In addition, the significant work-hardening within PLC bands explained the nature of PLC band propagation.　After a region within a PLC band was sufficiently work-hardened by the accumulation of many dislocations, plastic deformation occurred in neighboring region which was rarely work-hardened and had more work-hardening capability. Such localized deformation occurred sequentially, and it was shown as the propagation of PLC bands.
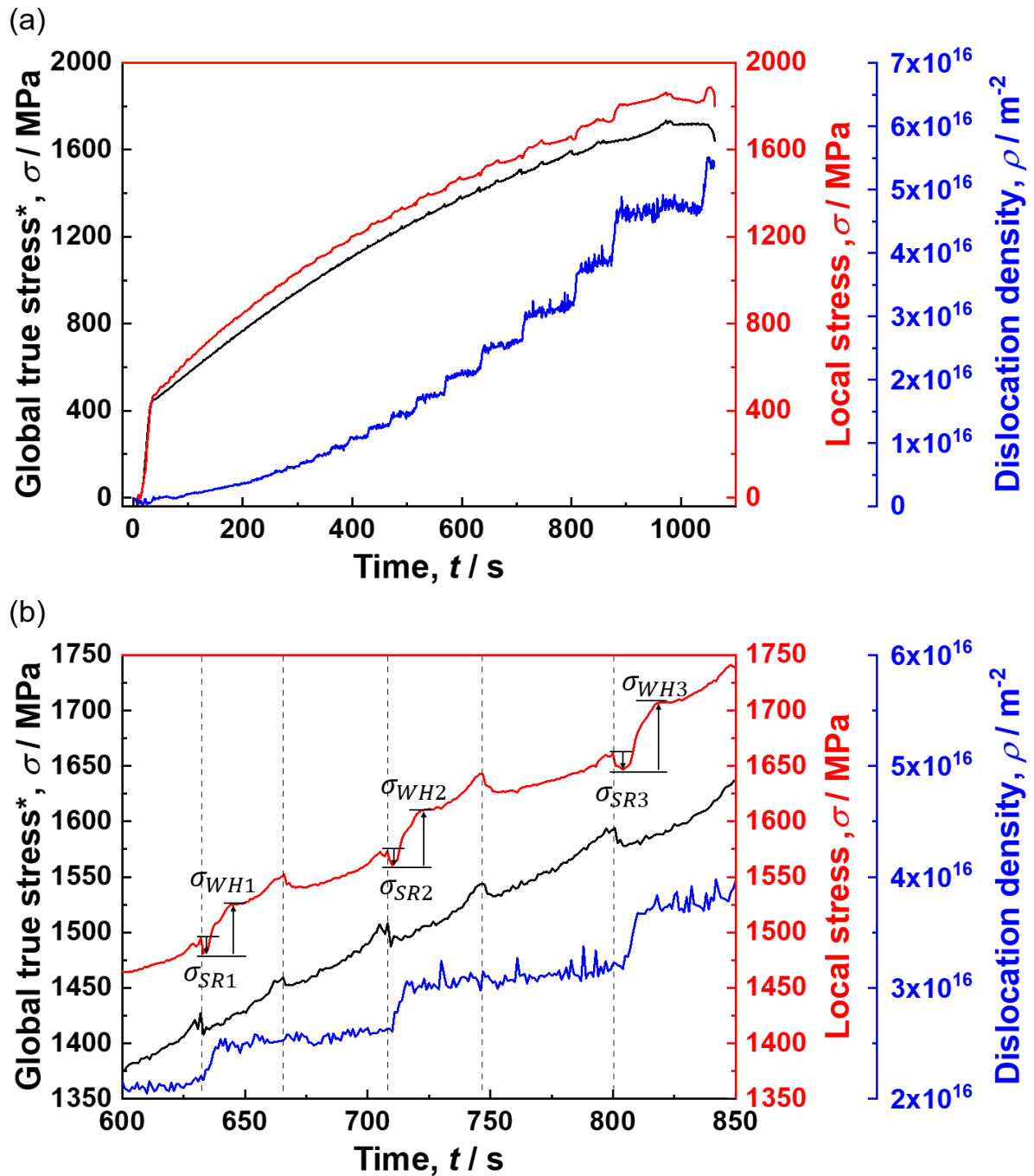
Fig. 2.22 (a) The changes of global true stress* (black, left y-axis), local stress at the XRD beam position (red, the first right y-axis), and dislocation density (blue, the second right y-axis) are shown as a function of the experimental time. (b) Curves in the time range from 600 s to 850 s, enlarged from (a). Serration peaks are indicated by thin broken lines. Stress relaxation (σ_{SR}) and work-hardening (σ_{WH}) are indicated by arrows on the curves.

2.3.10 Correlation between global stress-strain curve (serrations) and localized deformation (PLC banding)

In the current section, the results obtained in a mesoscopic scale would be summarized and schematically illustrated how the localized deformation induced by PLC banding develops the global work-hardening.

Figure. 2.23 schematically illustrates an enlarged stress-strain curve including three serration peaks. Nine representative stages (①～⑨) are indicated on the schematic stress-strain curve in **Figure. 2.23 (a)**. PLC banding in the tensile specimen, and corresponding evolutions of elastic and plastic strains at the deformation stages ①～⑨ are illustrated in **Figure. 2.23 (b)**. Just before the stage ①, there is no PLC band in the gage part, so that the plastic deformation is suppressed and the elastic strain (thus stress) quickly increases to form a serration peak. At the stage ① corresponding to the serration peak, a new PLC band nucleates near the gage center, so that elastic strain in the whole gage part of the tensile specimen decreased by plastic accommodation, leading to a stress drop in the stress-strain curve, as was observed in **Fig. 2.18 (c)** and **Fig. 2.22 (b)**. Elastic strain within the nucleating PLC band starts to be furthermore relaxed while the plastic strain starts to increase. At the stage ② just after the stress drop on the stress-strain curve, the PLC band starts to propagate to the right direction. At this stage, a significant relaxation of elastic strain and an increase of plastic strain occur inside the PLC band, as was observed in **Fig. 2.18 (c)**, **Fig. 2.22 (b)** and **Fig. 2.15 (c)**, respectively. At the stage ③, the PLC

band continues to propagate, and the area the PLC band already swept (yellow-colored region) has been work-hardened since a large number of dislocations are activated and accumulated, as was shown in **Fig. 2.18 (c)** and **Fig. 2.22 (b)**. Because of this work-hardening, the elastic strain in the yellow region should be somehow larger than that in the left-side region where the PLC band has not yet swept. Meanwhile, the plastic strain remains almost constant in the area the PLC band has swept (yellow-colored region). At the stage ④, the PLC band has finished propagating the right half of the gage part and is disappearing at the right shoulder part. As a result, the distribution of plastic strain is heterogeneous and the right half of the gage part is more strain-hardened than the left half, as was shown in **Fig. 2.16**. From the stage ④ to ⑤ where no PLC band exists within the gage part, the plastic deformation of the specimen is greatly suppressed and the elastic deformation becomes dominant in the whole gage part, so that the flow stress of the material quickly increases to form a serration peak on the stress-strain curve. It should be noted that the slope of the stress-strain curve just before the serration peak was measured to be 5 GPa ~ 13 GPa, which was much smaller than the Young's modulus of the present material (116 GPa). This indicates that the material still deforms plastically from the stage ④ to ⑤ even with no PLC band in the gage part. The elastic strain in the right half of the gage would be somehow higher than that in the left half, because the right half is more strain-hardened. At the stage ⑤, a new PLC band nucleates near the center, probably due to the imbalance of the plastic and elastic strains (so that the imbalance of the local stress) between the right half and left half of the gage section. The

newly nucleated PLC band propagates to the left direction (to the softer region) in this turn at the stages ⑥ to ⑦.   With the PLC band sweeping the left half, the plastic and elastic strains in the whole gage part becomes uniform (⑧).   Then, the PLC band disappears at the left shoulder part, elastic strain in the specimen increases to form another serration peak, and a new PLC band nucleates somewhere (⑨) leading to the stress drop.   By the repetition of the processes from ① to ⑧ (corresponding to one cycle of the PLC banding), the global deformation of the present material proceeds.

In the present study, the mesoscopic nature of the serration behavior in the 22Mn-0.6C austenitic steel was clarified by the aid of the *in-situ* DIC analysis and synchrotron diffraction during tensile deformation.   It was shown that the plastic (and also elastic) deformation within the gage part of the tensile specimen was quite heterogeneous, and characterized by the nucleation, propagation and annihilation of the PLC bands where plastic deformation is localized. Interestingly, the serrations appearing on the global stress-strain curve, which expressed averaged deformation of the specimen totally corresponded with the localized deformation behavior, i.e., PLC banding.   The characteristics of the shape of serrations, and the changes in the local lattice (elastic) strain and the dislocation density were all consistently explained by the PLC banding.

Atomistic mechanisms of the localized deformation were not clarified in the present study. However, if the serration behavior is caused by DSA as has been believed, the current results suggest that dynamic interaction between dislocations and solute atoms change depending on the

location with the propagation of PLC bands. Although deformation twinning can be another deformation mechanism, the contribution of twinning to plastic deformation is considered to be fairly smaller than that by dislocation slips, as was discussed in the section 2.3.8. Furthermore, it is difficult to imagine that deformation twinning induces PLC banding, i.e., nucleation, propagation and annihilation of deformation localized bands observed in the present study. The mechanism of DSA and PLC banding would be discussed in the next chapter.

The quick increase of the local dislocation density within the PLC bands should be associated with the localized deformation at higher strain rates in the bands. It should be noted that the local strains within the PLC bands were not so much high compared to those outside the bands up to medium stages of tensile deformation, which would make the whole deformation of the material relatively stable and maintain high strain-hardening rates (**Fig. 2.12 (c)**). As was shown in **Fig. 2.15 (a)**, however, the magnitude of strains localized in the PLC bands increased with increasing tensile strain and reached to 0.0546 ~ 0.1137 at later stage of tensile deformation, which could be the reason for the fracture with small post-uniform elongation in high-Mn TWIP steels compared with other kinds of steels and metallic materials. Yu et al. [42] reported that the post-uniform elongation in 18Mn-0.6C-(0~1.5)Al steels decreased with decreasing the Al contents. In their study, PLC band propagation was observed along the side surface of the tensile specimen of the Al-free steel, whereas the PLC band was not observed in the Al-added steels. At later stage of deformation (e=30 %) of the Al-free steel, several edge cracks formed within the PLC band.

They considered that the localized strain within the PLC band caused the edge crack on the side surface of the tensile specimen, leading to fracture and the limited post-uniform elongation in the Al-free 18Mn-0.6C steel.

The serration behavior is often observed in the metallic materials having good strain-hardening abilities (so that showing both high strength and large ductility), which include not only high-Mn steels but also Al-Mg alloys, high entropy alloys, and so on. The mesoscopic features of serrations and PLC banding which have been systematically clarified in the current study would greatly help to deepen the understanding of the nature of the PLC effect (or DSA).
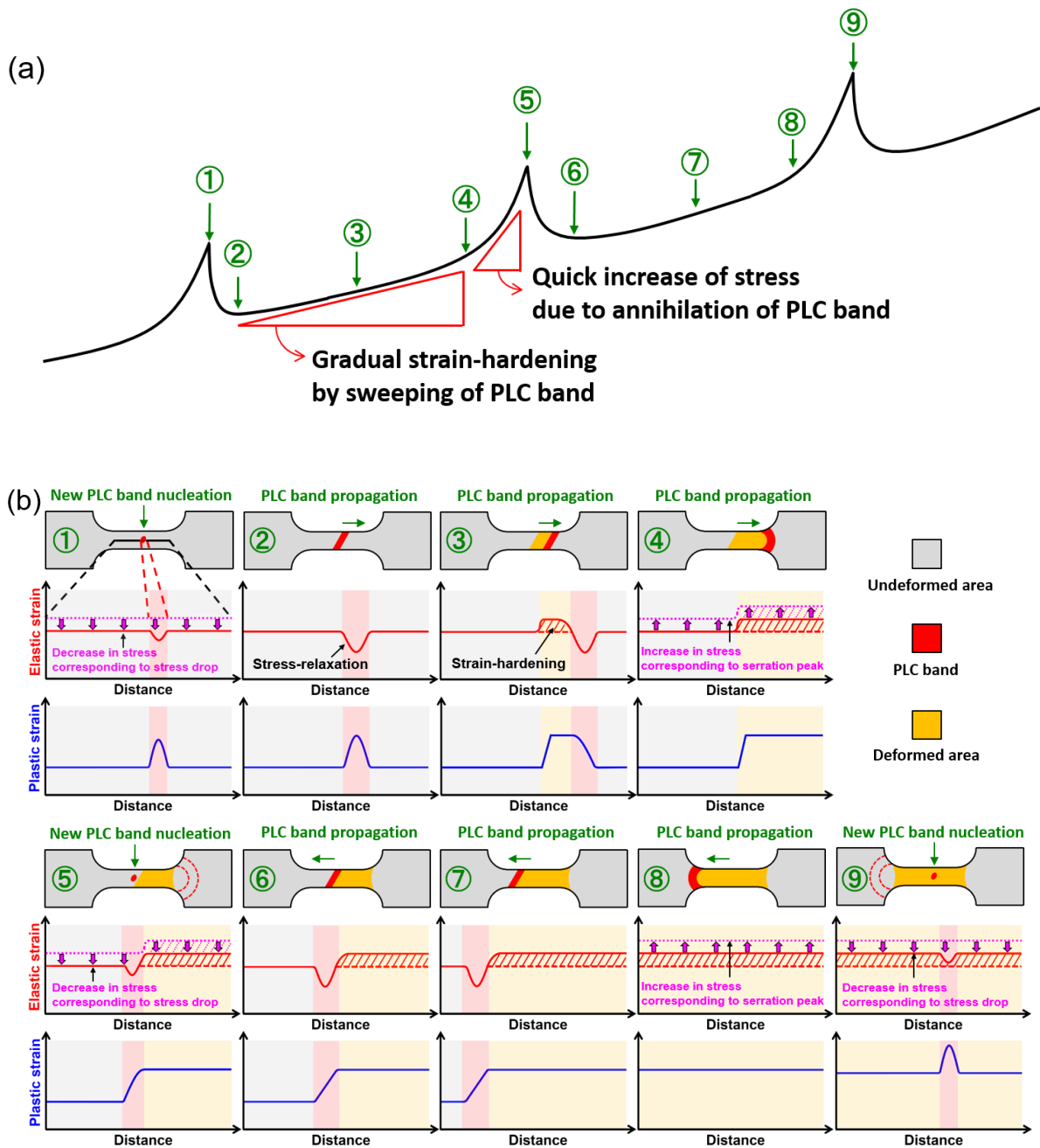
Fig. 2.23 Schematic illustrations summarizing the correlation between the macroscopic serration behavior and the mesoscopic localized deformation clarified in the present study. Slopes of the stress-strain curve (i.e., strain hardening) are roughly indicated by red triangles. (a) Schematic illustration of stress-strain curve including three serration peaks. (b) Schematic illustrations showing the nucleation, propagation and annihilation of PLC bands in the gage part, and corresponding distributions of elastic and plastic strains along the gage, at different stages (① ~ ⑨) on the stress-strain curve (a). Gray, red and yellow colored areas indicate the region with little plastic deformation, the region the PLC band is propagating, and the region the PLC band already swept, respectively.

2.4   Conclusion

The mesoscopic nature of the serration behavior in a 22Mn-0.6C steel was systematically investigated by the aid of the *in-situ* DIC technique and the *in-situ* synchrotron XRD measurement during tensile tests, and the localized deformation behavior in the form of PLC banding was correlated with the global deformation of the material.   The results can be summarized as follows:

1. After 4 cycles of repeated cold-rolling and annealing process, the 22Mn-0.6C steel with a fully recrystallized microstructure having the mean grain size of 2.0 μm was obtained.

2. The material exhibited the good balance of high strength and large ductility: Yield strength was 430 MPa (0.2 % proof stress), tensile strength was 1136 MPa, and total elongation was 69 %. Serrations were observed during the tensile deformation.

3. With the aid of the DIC method, it was found that the serration behavior was the response of the formation, propagation and annihilation of PLC bands (PLC banding) in the tensile specimen.   It was clarified that the plastic strain increased drastically only within the PLC band, whereas the plastic strain remained almost constant beyond the PLC band.   The serration peaks corresponded to the suppression of plastic deformation due to the annihilation of PLC band within the gage part.   Nucleation of a new PLC band resulted in the quick stress accommodation (stress-drop) just after the peak.

4. The *in-situ* synchrotron XRD measurement at a fixed position during the tensile test revealed that the lattice strain in the X-ray beam position increased at every serration peak, which indicated that the whole specimen was more elastically deformed due to the absence of PLC band within the gage part. The dislocation density suddenly increased when a PLC band was passing through the measurement area because plastic deformation was concentrated and a large number of dislocations were introduced within the PLC band, which corresponded to a drop of the local lattice strain (elastic strain).

5. From the experimentally obtained elastic modulus and elastic strain, local stress at the X-ray beam position was quantified. In a time range from 600 s to 850 s, the stress relaxation induced by the propagation of PLC band was around several megapascals. In this time range, the work-hardening by single passage of PLC band was in a range of 44 ~ 60 MPa, indicating that most of the work-hardening of the present material was achieved by the propagation of PLC bands.

6. By the repetition of such a cycle of PLC banding (i.e., the nucleation, propagation, and annihilation of PLC bands) throughout the whole tensile deformation, plastic deformation of the material gradually proceeded, resulting in the global work-hardening in the present 22Mn-0.6C steel.

Chapter 3　　　　Mechanism of DSA correlating to the PLC banding

3.1　　　　Introduction

In the previous chapter, mesoscopic nature of serration behavior in the 22Mn-0.6C steel was thoroughly investigated. Serration behavior on the global stress-strain curve in the high-Mn austenitic steel perfectly corresponded to the local heterogeneous deformation characterized by the formation, propagation and annihilation of PLC bands, i.e., PLC banding. Furthermore, heterogeneous deformation in mesoscopic scale was successfully correlated with local stress and dislocation density. The region within the PLC band temporarily experienced stress relaxation due to the sudden increase of dislocation density, and then the local stress within the PLC band significantly increased, indicating that the work-hardening of the 22Mn-0.6C steel occurred sequentially with the propagation of the PLC band.

However, it is still unclear how such a mesoscopic inhomogeneous deformation characterized as the PLC banding was related with the microscopic DSA effect (or PLC effect). As discussed in the section 1.2, the DSA effect has been considered to be the result of the dynamic interaction between dislocations and carbon atoms during deformation. Under certain deformation conditions, e.g., intermediate temperature or strain rate, carbon atoms diffuse near the mobile dislocations, and they pinned mobile dislocations creating the Cottrell atmosphere. If the stress sufficiently increased to overcome the obstacles, they de-pinned from carbon atoms and glided away until they were pinned again by diffusing carbons. So far, it has been considered

that the stress to de-pin the dislocations corresponded to serration peak in stress-strain curves.

The idea was extended to high-Mn austenitic steels (TWIP steels), and many researchers

substituted partial dislocations for the perfect dislocation in the conventional theory for DSA

effect, as discussed in the section 1.2.   However, most of the studies so far commonly assumed

that serrations induced by DSA happened homogeneously over the entire tensile specimen, and

none of the studies considered how the DSA effect lead to the inhomogeneous deformation

characterized as the PLC banding.

Recently, Oh et al. [43] reported that the DSA during tensile deformation of 18Mn-0.55C

steel was induced by long-range diffusion of carbons along the dislocation line, which was known

as pipe diffusion of carbon.   They calculated the activation energy for serration for their material,

and found out the calculated value was similar with the activation energy for dislocation pipe

diffusion of carbon that was previously reported by other researchers.   They also observed the

distribution of carbons within the PLC band by atom prove tomography (APT) analysis, and they

argued that the lines containing higher carbon contents in APT maps corresponded to dislocations

pinned by carbons.   However, it was natural for carbons to be segregated near defects by

diffusion, if enough time was allowed after the tensile specimen was unloaded.   To discuss the

nature of dynamic strain aging (DSA), the consequent change of dislocation glide should be

investigated in real time during tensile test.

The studies on the motion of dislocations, especially about the velocity of dislocations, are

very small in number due to the difficulty in measurement. Several decades ago, Johnston and

Gilman [44] invented a method to measure the average velocity of dislocations by tracing etch

pits, and their study has been still widely referred. They first introduced dislocations in the LiF

by lightly deforming its surface, and etched the surface to detect the position of dislocations.

Then, the crystal was subjected to a constant stress pulse. Before and after each stress pulse, the

crystal was etched to trace the dislocation movement. By measuring the distance between the

former etch pit and a newly formed etch pit, which corresponded to the distance of dislocation

movement, the average velocity of dislocations was determined. They performed the

experiment at different stress levels, and they found out that the velocity of dislocations increased

as the applied shear stress increased. However, it is difficult to apply their method for measuring

dislocation velocity during uniaxial tensile test.

According to Orowan et al. [45], shear strain can be related with the dislocation density and

the glide of dislocations, as:

$$\gamma = \rho b \bar{x} \tag{3.1}$$

where, γ is the shear strain, ρ is the dislocation density, b is the magnitude of Burger vector,

and $\bar{x}$ is the average distance of dislocation glide. If the $\bar{x}$ is the rate-controlling factor in

determining the plastic shear strain, the Eq. (3.1) can be written again, as:

$$\dot{\gamma} = \frac{d\gamma}{dt} = \rho b \bar{v}_d \tag{3.2}$$

where, $\dot{\gamma}$ is the shear strain rate and $\bar{v}_d$ is the average dislocation velocity. Therefore, the

average dislocation velocity ($\bar{v}_d$) can be determined if shear strain rate ($\dot{\gamma}$) and dislocation density (ρ) can be experimentally obtained.

In the current chapter, we aim to investigate how the motion of dislocation glide changes with PLC banding.   In addition, carbon diffusivity in the present material was also calculated. By making a comparison between the dislocation velocity and the carbon diffusivity with PLC banding, we can understand how pinning and de-pinning of dislocations by carbons, i.e., DSA effect, caused the macroscopic serration behavior.   DIC technique and *in-situ* synchrotron XRD measurement were applied simultaneously during tensile deformation of the material, for obtaining the local strain rate and dislocation density of an identical area.

3.2   Experimental procedures

3.2.1 Materials

Fe-22Mn-0.6C (wt. %) was used in the present study.   The detailed chemical composition of the steel was shown in **Table 2.1**.   The as-received hot-forged material was subjected to 4 cycles of the cold-rolling and annealing treatments in order to achieve grain refinement.   A fine-grained specimen with an average grain size of 2.0 μm was obtained by annealing the final sheet at 800 °C for 300 s followed by water quenching.   Detailed thermomechanical process was illustrated in **Fig. 2.1**.

3.2.2 Simultaneous performance of DIC technique and *in-situ* synchrotron XRD measurement during tensile test

In order to simultaneously evaluate the local strain rate and dislocation density of an identical area, DIC technique and *in-situ* synchrotron XRD measurement were performed simultaneously during tensile test.　The sheet-type tensile specimen illustrated in **Fig. 2.7** was cut from the sheet having the fully recrystallized microstructure with the mean grain size of 2.0 μm. The tensile specimen was first painted white and then covered with randomly distributed black speckle patterns by using an airbrush, as illustrated in **Fig. 2.3**.　The DIC technique and *in-situ* synchrotron XRD measurements were performed together at high energy (HE) synchrotron beam line of BL46 XU at SPring-8 of JASRI.　A monochromatic synchrotron beam with an intensity of 30 keV (λ = 0.0413 nm) was used for the transmission diffraction.　The time resolution for a diffraction profile was 1 second.　Before tensile test, a complementary MOS (CMOS) camera were set in the beam line for recording the speckle patterns on the specimen at a rate of 2 frames per second.　Two-dimensional strain tensors at different positions were obtained by differentiating displacement vectors obtained by tracking the speckle patterns.　Local strain rates at different position were evaluated by the use of the local strain data.　The tensile direction was parallel to the rolling direction (RD) of the sheet.　The direction of the incident beam was perpendicular to the tensile direction, and the incident beam having a size of 0.5 mm in the gage-width direction and 0.2 mm in the gage-length direction was irradiated at the center of the gage part of the tensile

specimen.　The configuration of the synchronized DIC technique and *in-situ* synchrotron XRD measurement during the tensile test is shown in **Figure 3.1**.　After a precise alignment, the tensile test was carried at an initial strain rate of 8.3×10^{-4} s^{-1} at room temperature.　In the tensile test, the tensile specimen was elongated upward with the bottom grip part fixed.　During the tensile deformation, diffraction profiles were simultaneously collected by serially-connected 6 detectors (MYTHEN X, Dectris).　The diffraction peaks were fit to Voigt function using Origin Pro 2017 program, and then the peak position and full width half-maximum (FWHM) of peaks were determined.　Peak positions and FWHMs of (111), (200), (311) and (222) were considered for subsequent analysis.　For evaluating the strain and stain rate distributions, the recorded images were analyzed by the use of Vic-2D software with a subset of 35 pixels in a square and a step size of 7 pixels, which was optimized for assessing the strain and strain rate distributions under the given resolution of the camera.　In the software, the imaginary extensometer was set along the gage part, and the global tensile strain (nominal strain) was also precisely measured.　The DIC and synchrotron XRD results were accurately synchronized by adjusting the time of macroscopic loading.
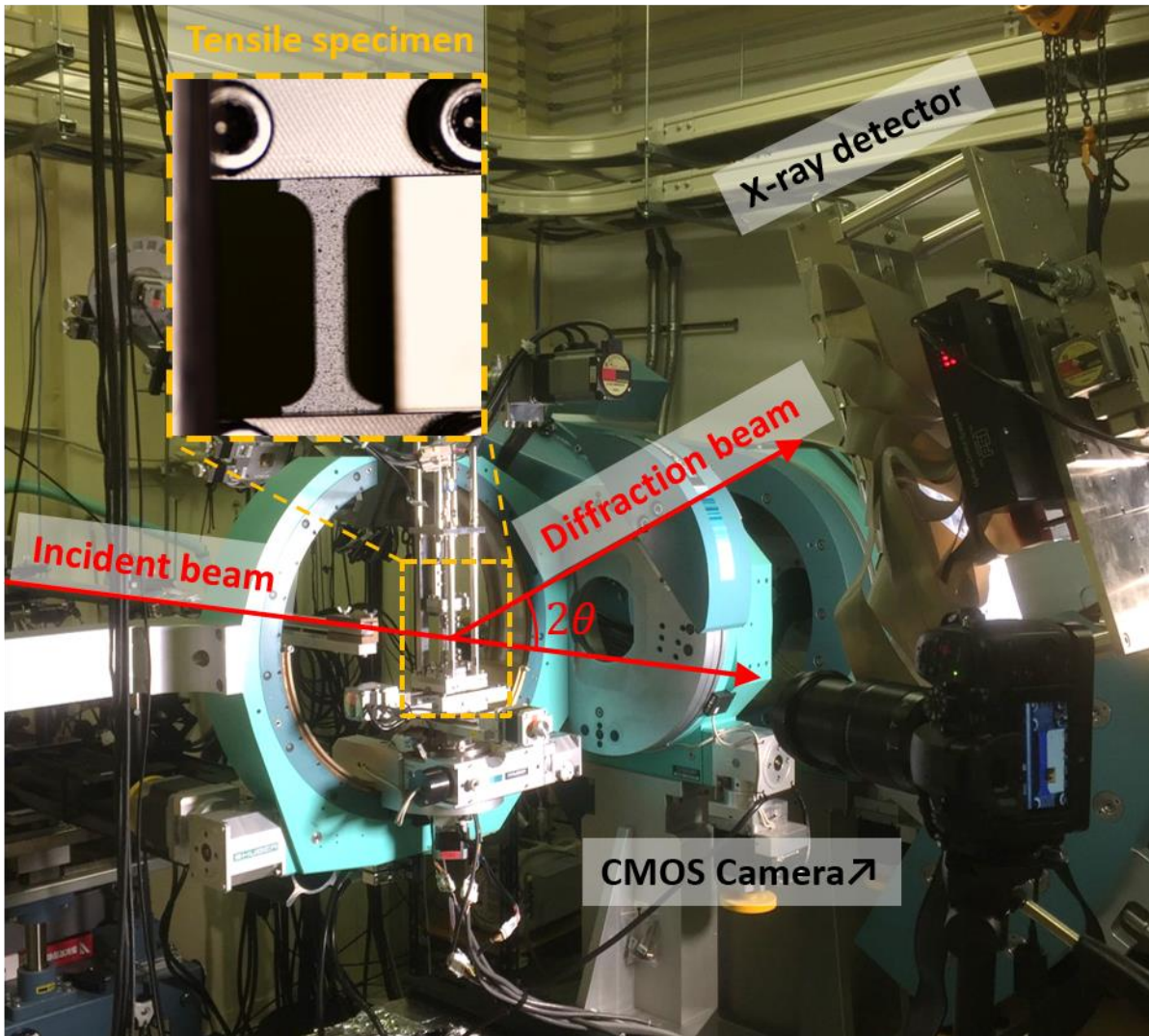
Fig. 3.1 The configuration of the synchronized DIC technique and *in-situ* synchrotron XRD measurement during the tensile test at SPring-8. Tensile specimen is enlarged in the figure.

3.2.3 Temperature measurement during tensile test

The change of local temperature during the tensile test was investigated, for the calculation of carbon diffusivity of the present material. The sheet-type tensile specimen illustrated in **Fig. 2.2** was cut from the sheet having the fully recrystallized microstructure with the mean grain size of 2.0 μm. Prior to the measurement, the tensile specimen was painted white to reduce the reflection from other light source. A thermal camera (FLIR, CPA-E75S) was set perpendicular to

the broad surface of the tensile specimen.   The tensile direction was parallel to the rolling direction

(RD) of the sheet.   After the careful alignment, tensile test was carried out on the painted specimen

at an initial strain rate of 8.3 $\times$ 10^{-4} s^{-1} at room temperature using a uniaxial tensile testing machine

(SHIMADZU, AG-100kN Xplus).   During the tensile deformation, the change of local

temperature was recorded at a 30 frames per second by the thermal camera with a thermal

sensitivity of 0.04 °C (at 30 °C) and graphical resolution of 320 $\times$ 240 pixels.   The recorded

images were analyzed by using FLIRTools software.

3.3   Results and discussion

3.3.1 Synchronized material parameters and local strain rate during tensile test

The DIC analysis and XRD measurement were synchronized precisely, and the results are

shown in **Figure 3.2**.   **Fig. 3.2 (a)** shows the changes of lattice strain (red) and dislocation density

(blue) at the XRD beam position during tensile deformation of the 22Mn-0.6C specimen, together

with nominal stress curve (black).   Nominal strain corresponding to experimental time is also

indicated along the upper x-axis.   Here, lattice strain refers to lattice strain of (200) plane, which

has the lowest modulus along <100> direction in FCC metals and alloys.   The lattice strain was

obtained by using Eq. (2.7), and the dislocation density (ρ) was calculated by using Eq. (2.5) and

(2.6).   As was discussed in the section 2.3.8, most of the peak broadening was considered to result

from accumulated dislocations.   In **Fig. 3.2 (a)**, the lattice strain (red) increased with experimental

time in most periods, but it dropped periodically. Dislocation density (blue) did not increase continuously, but increased in a stepwise manner. During the most periods, the curve of dislocation density was almost flat, but it increased significantly at certain experimental times.

Fig. 3.2 (b) shows the enlarged curves in a time range from 625 s to 850 s. In this time range, it was confirmed the PLC bands nucleated at a little upper position of the gage part, and propagated upwards and downwards alternately. The pattern of nucleation and propagation of PLC bands was same as the one in the section 2.3.3. Thin broken lines are drawn at the experimental times when serration peaks appeared on the nominal stress curve. Different marks are used to indicate the positions of serration peaks (▼), peaks of lattice strain (▼), drops of lattice strain (△) and sudden increase of dislocation density (△). The numbers (1) ~ (5) on dislocation density curve correspond to the strain-rate maps shown in later (**Fig. 3.2 (c)**). In **Fig. 3.2 (b)**, two serration peaks (▼) appeared consecutively, and they perfectly coincided with the peaks of lattice strain (▼), indicating that the serration peaks in global stress-strain curve were the response of the local peaks of lattice strain. As was clarified in the section 2.3.8, the sudden increases of dislocation density (△) resulted from the passage of PLC bands on the beam position. Because the sudden increases of dislocation density (△), i.e., plastic deformation, relaxed elastic stress, small drops of lattice strains (△) were observed at the same time. **Fig. 3.2 (c)** shows the strain-rate maps ($d\varepsilon_{yy}/dt$) corresponding to the PLC band propagation near the XRD beam position. The number (1) ~ (5) in the strain-rate maps corresponded to the numbers indicated in **Fig. 3.2 (b)**. Comparing between

90

Fig. 3.2 (b) and **Fig. 3.2 (c)**, when the PLC band was away from the beam position ((1) in **Fig. 3.2 (c)**), increase of the local dislocation density was very small ((1) in **Fig. 3.2 (b)**).   At the point (2) in **Fig. 3.2 (c)**, when the PLC band was about to enter the beam position, the local dislocation density started to increase drastically ((2) in **Fig. 3.2 (b)**).   At the point (3) in **Fig. 3.2 (c)**, when the beam was totally inside the PLC band, the local dislocation density was increasing significantly ((3) in **Fig. 3.2 (b)**).   At the point (4) in **Fig. 3.2 (c)**, when the PLC band was about to leave the beam position, the local dislocation density changed from significant increase to flat curve.   At the point (5) in **Fig. 3.2 (c)**, when the PLC band totally left the beam position, the increase of the local dislocation density became very small again ((5) in **Fig. 3.2 (b)**), as before the PLC band passed the beam position ((1) in **Fig. 3.2 (b)**).   It was clearly confirmed again that sudden increase of dislocation density ($\triangle$) perfectly corresponded with the passage of the PLC band through the beam position, and through the synchronized XRD measurement and DIC analysis, it was also possible to obtain both dislocation density and the corresponding strain rate of an identical area, i.e., beam position, at the same time.
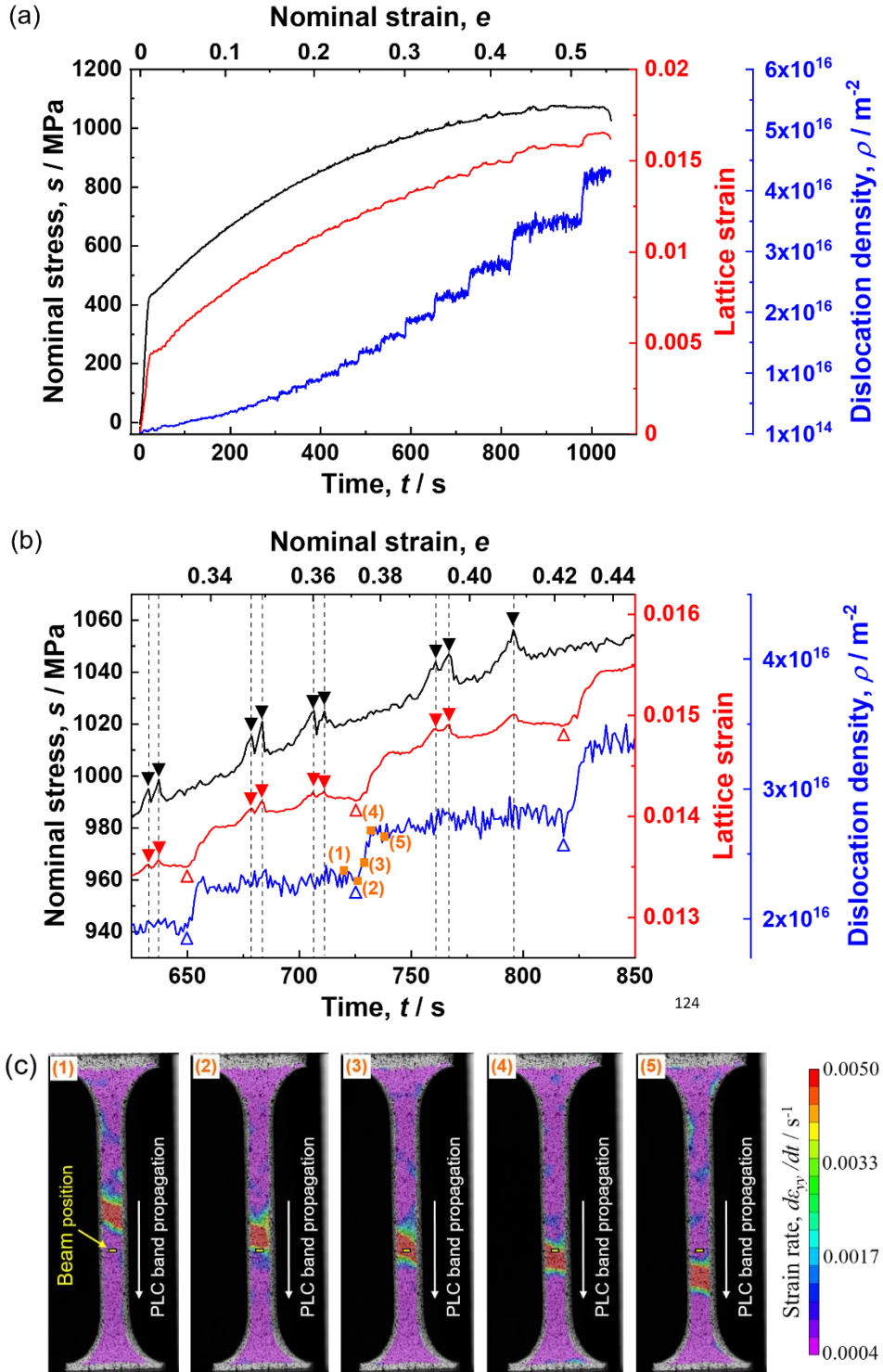
Fig. 3.2 (a) The changes of lattice strain (red) and dislocation density (blue), and nominal stress curve (black) are shown as a function of the experimental time. (b) Curves in the time range from 625 s to 850 s, enlarged from (a). Serration peaks are indicated by thin broken lines. Serration peaks (▼), peaks of lattice strain (▼), drops of lattice strain (△), and sudden increases of dislocation density (△) are indicated on the curves. The numbers (1) ~ (5) marked on the dislocation density curve correspond to the DIC images of (1) ~ (5) in (c). (c) DIC strain-rate maps corresponding to the PLC band propagation near the XRD beam position.

3.3.2 DSA effect correlated with PLC banding during tensile test

By applying both DIC analysis and XRD measurement during tensile test, the local strain rate and dislocation density of an identical area (XRD beam position) were successfully obtained. However, the strain rate obtained from the DIC analysis was the tensile strain rate, so the tensile strain should be converted to the shear strain for calculating the dislocation velocity by using Eq. (3.2). In Taylor model for uniaxial tensile test, the sum of the individual shear strain given by every slip system in a grain is expressed as,

$$\Gamma = \sum_{\alpha} \gamma^{(\alpha)} = M \times \varepsilon_{yy} \tag{3.3}$$

where, Γ is the sum of the individual shear strain given by every slip system in a grain, $\gamma^{(\alpha)}$ is the shear strain given by the slip system of α, M is the Taylor factor, and ε_{yy} is the tensile strain. When plastic deformation in a grain is mostly given by the primary slip system at a certain deformation time, the sum of the individual shear strain in a grain (Γ) is approximated to the shear strain given by the primary slip system. The term of the shear strain (γ) hereafter refers to the shear strain given by the primary slip system in a grain. Taylor factor in FCC material with random texture is known to be 3.06, and the local tensile strain (ε_{yy}) at the beam position was obtained over the entire deformation from the DIC analysis. The shear strain (γ) was calculated from Eq. (3.3), and it is plotted as a function of the dislocation density (ρ) in **Figure 3.3**. Total 25 data points were plotted, and they were shown together with the fitted line (red line). It was

found that the shear strain increased as the dislocation density increased.   Interestingly, however, the shear strain at a low dislocation density increased nonlinearly, whereas the shear strain increased linearly from a medium-low dislocation density.   Those two regions were colored in green and blue, respectively, in **Fig. 3.3**.   In the Eq. (3.1), shear strain (γ) is given by both dislocation density (ρ) and average distance of dislocation glide ($\bar{x}$).   At the early stage of deformation where the dislocation density was low (green-colored region), dislocations can glide large distance without being hindered by other dislocations, i.e., large mean free path (MFP) of dislocations.   The shear strain given by large $\bar{x}$ (large MFP) at the low dislocation density lead to the deviation from the linearity of the γ-ρ curve, and the tendency was more apparent at the very early stage of deformation.   On the other hand, after the dislocation density has increased significantly (blue-colored region), dislocations can glide rather short distance being hindered by other dislocations, i.e., small MFP of dislocations.   The   small $\bar{x}$ (small MFP) lead to the linear increase of the shear strain with the dislocation density.   Therefore, within the blue-colored region, the increase of the shear strain ($\Delta\gamma$) was controlled by the average distance of dislocation glide ($\Delta\bar{x}$), which is so-called the rate-controlling factor, rather than dislocation density ($\Delta\rho$).
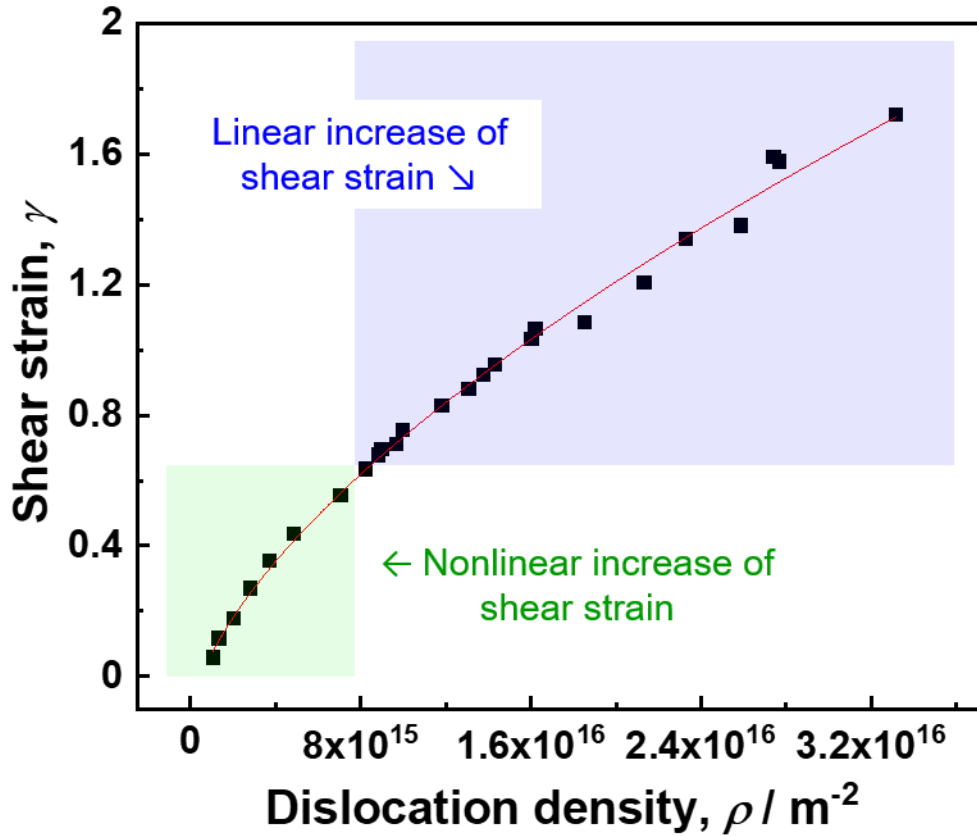
Fig. 3.3 Change of shear strain as a function of dislocation density. 25 data points were plotted, and they were shown together with the fitted line (red line). Green-colored region indicated the nonlinear increase of the shear strain with dislocation density, and blue-colored region indicated linear increase of the shear strain with dislocation density.

By applying the Eq. (3.2), the average dislocation velocity ($\bar{v}_d$) was calculated, and it is plotted as a function of experimental time in **Figure. 3.4**.   The average dislocation velocity was distinguished in two groups depending on the PLC band position.   The average dislocation velocity within the PLC band was colored red, and the average dislocation velocity beyond the PLC band was colored blue.   The average dislocation velocity was commonly smaller than 10 nm/ s irrespective of the PLC band position.   The fastest average dislocation velocity was 7.6107 nm /s at 368 s, and the slowest average dislocation velocity was 0.01163 nm/ s at 693 s.   It was

also found that the average dislocation velocity within the PLC band (red) was decreasing with

increasing experimental times, whereas the average dislocation velocity beyond the PLC band (blue)

was not changed much.   Interestingly, the average dislocation velocity within the PLC band (red)

was 50~700 times faster than the average dislocation velocity beyond the PLC band (blue).   The

results strongly suggest that the dynamic interaction between carbon and dislocation changes with

the PLC band position.   The very slow dislocation velocity beyond the PLC band was thought to

be the result of the pinning of dislocations by carbons, and much faster dislocation velocity within

the PLC band was thought to be the result of the de-pinning of dislocations within the PLC band.
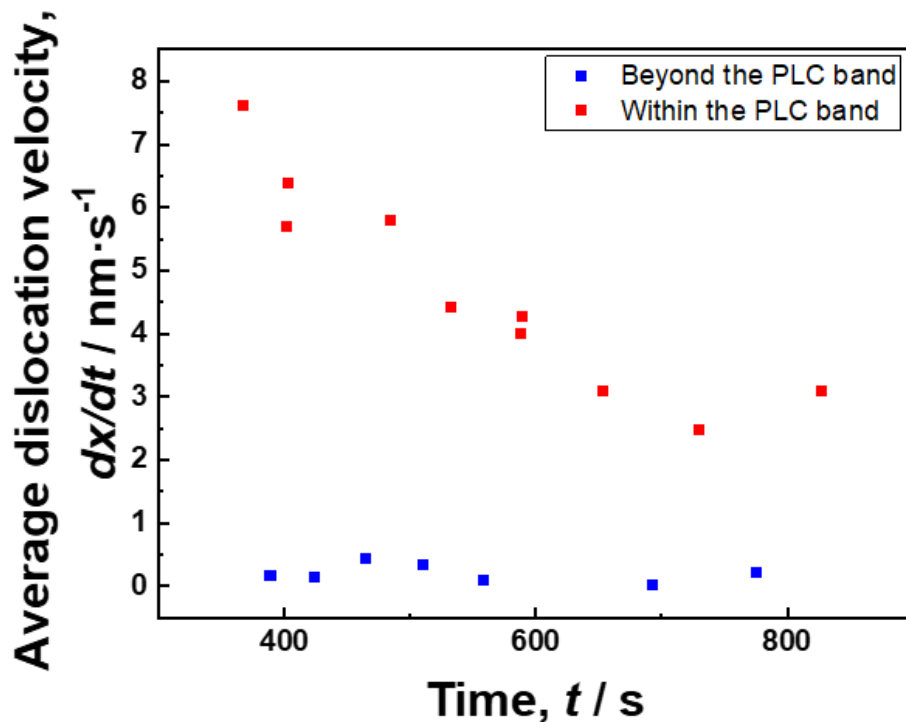
Fig. 3.4 The average dislocation velocity was calculated by applying the Eq. (3.2), and it is plotted as a function of experimental time. The average dislocation velocity within the PLC band was colored red, and the average dislocation velocity beyond the PLC band was colored blue.

Next, carbon diffusion in the present material was investigated in comparison with the dislocation velocity, for clarifying the dynamic interaction between carbon and dislocation. Diffusion coefficient of carbon is expressed by Arrhenius equation, as follows,

$$D_c = D_0 exp\left(-\frac{Q}{RT}\right) \tag{3.4}$$

where, D_c is the diffusion coefficient of carbon, D_0 is the pre-exponential factor, R is the gas constant, T is the temperature and Q is the activation energy of carbon diffusion. **Figure 3.5 (a)** shows temperature map at a late stage of deformation (t=1003.9 s to 1125.4 s), which corresponded to one cycle of PLC bands. The magnitude of the local temperature is expressed in different colors according to the color bar shown above. PLC bands appeared having higher temperature. The pattern of the PLC band propagation in the present study was same with the pattern shown in **Fig.2.13**. The PLC band nucleated near the gage center in (1), propagated upward (2, 3), and annihilated at the upper shoulder part in (4). The band again nucleated near the gage center again (5), propagated downward (6, 7), and annihilated at the lower shoulder part in (8). At the point of (7), The temperature within the PLC band was 24.2 °C and that beyond the PLC band was 22.2 °C. As shown in the image inserted in **Fig. 3.5 (b)**, an analyzed spot was set in the gage part, and the change of the local temperature was plotted as a function of experimental time. The local temperature fluctuated during the deformation, and the height of the temperature fluctuation, i.e., before and after the passage of the PLC band, became higher with progressing the deformation. It was found that the temperature difference within the PLC band

97

and beyond the PLC band was 2.9 °C at the largest (the temperature difference between at t=1179.8

s and t=1267.5 s).   In addition, the temperature of the tensile specimen was 20.9 °C before tensile

test, and increased to 27.1 °C at the point of fracture.   Therefore, the temperature (T) in Eq. (3.4)

was commonly set to 300 K, regardless of the PLC band position and nor the stage of the

deformation.   Pre-exponential factor (D_0) and activation energy (Q) of carbon diffusion in the

high-Mn austenitic steel (here, Fe-15Mn-0.34C [wt.%]) was reported to be 9×10^{11} nm^2/ s and

133800 J/ mol, respectively [46].   By substituting T, D_0, and Q into Eq. (3.4), the diffusion

coefficient of carbon (D_c) of the present material was estimated to be 4.5×10^{-12} nm^2/ s.   The

diffusion distance of carbon can be calculated as,

$$x_c = \sqrt{D_c t} \qquad (3.5)$$

where, x_c is the diffusion distance of carbon, D_c is the diffusion coefficient of carbon ($4.5 \times$

10^{-12} nm^2/ s) and t is the time for carbon diffusion.   For 1 second, carbon can diffuse only

2.1×10^{-6} nm.   Comparing the carbon diffusivity with the dislocation velocity, which was the

order of 10^{-2} nm/ s beyond the PLC band and the order of 10^{0} nm/ s within the PLC band, it is

hard to imagine that carbons can catch up with dislocations.   It is more reasonable to consider that

gliding dislocations sweep the stationary carbons, and at certain points the dislocations get pinned

by large number of carbons that were swept by the dislocations.   Such a phenomenon was

happening beyond the PLC band, where the dislocation velocity was much slower than that within

the PLC band (**Fig. 3.4**).   However, once the local stress in the region increases to de-pin the

dislocation (**Fig. 3.2 (b)**), dislocations can glide freely again, and the sudden activation and

accumulation of dislocations appeared as the localized deformation in the mesoscopic scale, i.e.,

the PLC band.
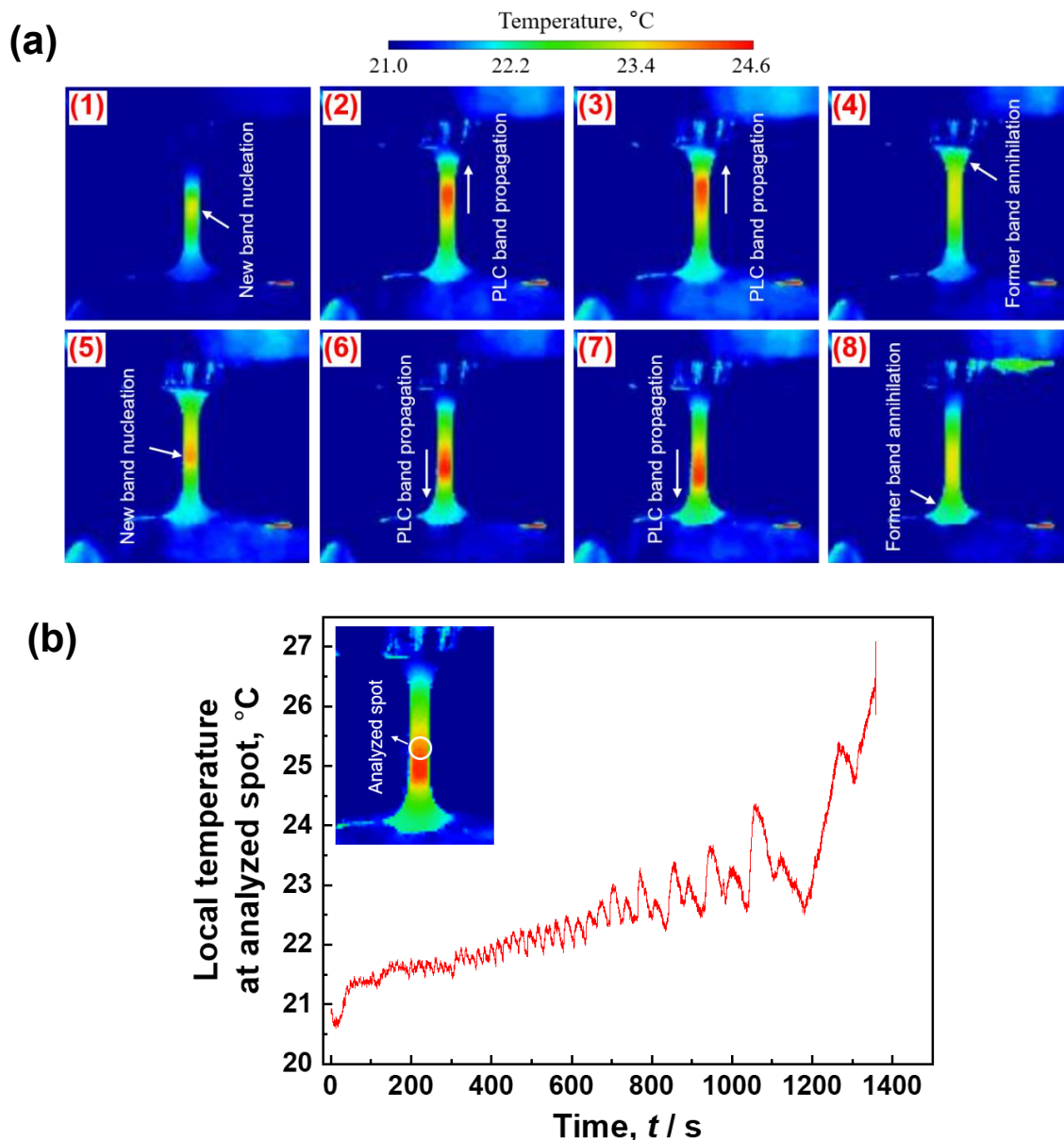
Fig. 3.5 (a) Local temperature maps at a late stage of deformation (t=1003.9 s to 1125.4 s), which corresponded to one cycle of PLC bands. The magnitude of the local temperature is expressed in different colors according to the color bar shown above. PLC bands appeared having higher temperature. (b) Changes of the local temperature at a analyzed spot set in the gage part till fracture, plotted as a function of experimental time.

The dislocation density (ρ) in Eq. (3.2) was somehow overestimated because (1) the peak broadening effect was assumed to result solely from dislocations and (2) all the dislocations were considered to be mobile dislocations.   However, the overestimated dislocation density indicates that the average dislocation velocity in Eq. (3.2) was underestimated to produce a certain shear strain.   That is, the difference between carbon diffusivity and dislocation velocity was actually larger, so that long-range diffusion of carbon was more unlikely to happen to pin the dislocations.

Figure. 3.6 schematically illustrates how the DSA effect was correlated with the mesoscopic inhomogeneous deformation characterized as the PLC banding.   Three regions represent ① the region where PLC band has not yet swept (blue-colored region in the left), ② the region where PLC band is sweeping (red-colored region in the center), and ③ the region where PLC band has finished sweeping (blue-colored region in the right), respectively.   In the region of ①, dislocation density is relatively small because the PLC band has not yet swept, and dislocation is pinned by carbons until the local stress in the region increases to de-pin the dislocation.   In the region of ②, dislocation density starts to increase significantly, and dislocations are de-pinned from carbons.   Due to the sudden activation and accumulation of dislocations, this region showed higher strain-rate and it appeared as the local PLC band in mesoscopic scale.   In the region of ③, the dislocation density has rarely changed after the PLC band swept away.   Dislocations are pinned again after the passage of the PLC band until the local stress becomes high enough to de-

pin the dislocations, i.e., next passage of the PLC band.   The results obtained in the current section

consistently explained that a large number of dislocations are activated and accumulated within the

local PLC bands, and the consequent PLC banding (the nucleation, propagation and annihilation

of the PLC bands) determined the global serration behavior in the stress-strain curve.
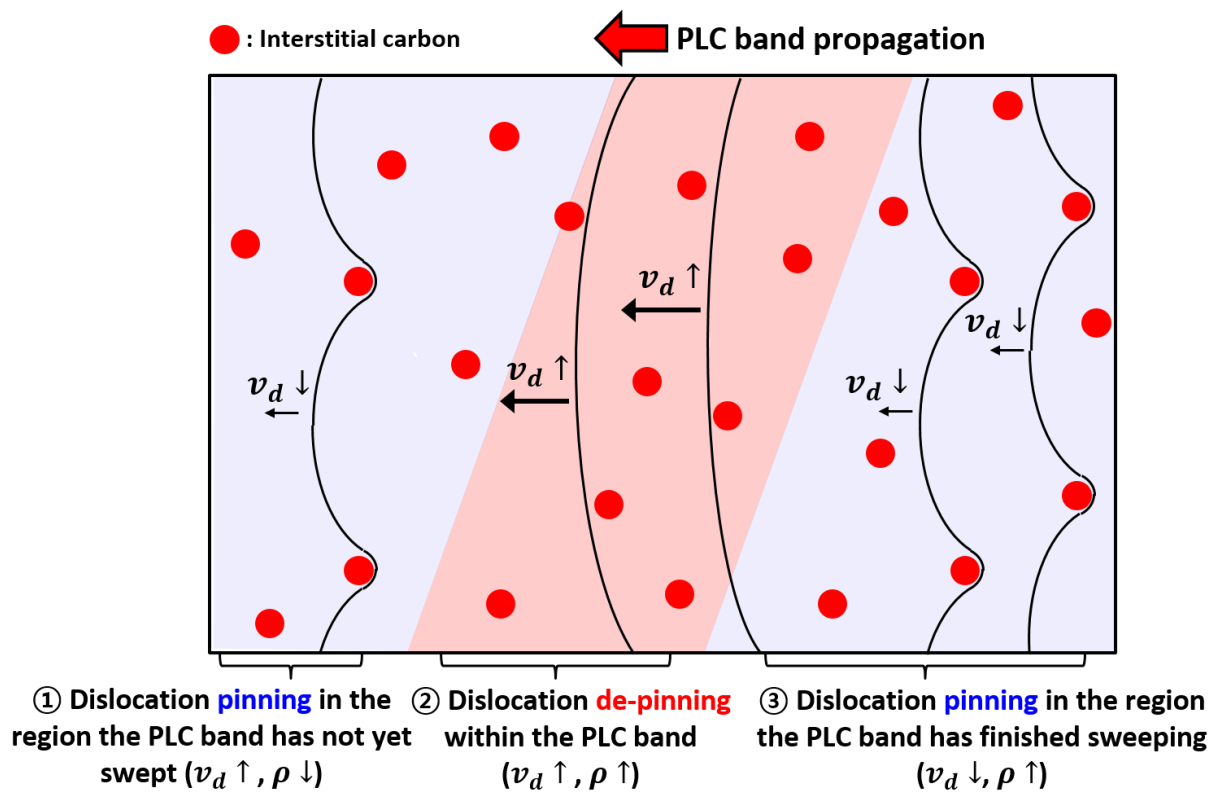
Fig. 3.6 Schematic illustration summarizing the correlation between the DSA effect and the mesoscopic PLC banding. Three regions are distinguished: ① the region where PLC band has not yet swept (blue-colored region in the left), ② the region where PLC band is sweeping (red-colored region in the center, and ③ the region where PLC band has finished sweeping (blue-colored region in the right), respectively.   Interstitial carbon atoms are shown as red circle.

3.4   Conclusion

In the current section, the DSA effect was successfully correlated with the mesoscopic PLC

banding with the aid of the DIC technique and *in-situ* synchrotron XRD measurement during tensile test. The results can be summarized as follows:

1.   The local strain rate and dislocation density at the XRD beam position were successfully obtained by simultaneously performing DIC technique and *in-situ* synchrotron XRD measurement. It was clearly clarified that sudden increase of dislocation density perfectly corresponded with the passage of the PLC band through the beam position.

2.   In the shear strain-dislocation density curve, the shear strain increased nonlinearly at a low dislocation density because dislocations can glide large distance without being hindered by other dislocations (large MFP of dislocations), whereas the shear strain increased linearly from a medium-low dislocation density because dislocations can glide rather short distance being hindered by other dislocations (small MFP of dislocations).

3.   The average dislocation velocity beyond the PLC band was the order of 10^0 nm/s, which was much slower than that within the PLC band of the order of 10^{-2} nm/s. Compared to the dislocation velocity, carbon diffusivity was extremely low that carbon can diffuse only 2.1×10^{-6} nm for 1 second. The obtained results indicate that gliding dislocations became pinned by sweeping the stationary carbons, and such a phenomena was happening beyond the PLC band. On the other hand, dislocations de-pinned again once the local stress sufficiently increased to overcome the pinning by carbons, and such a phenomena was happening within the PLC band.

4.   Such localized pinning and de-pinning (the DSA effect) occurred sequentially, and it was

shown as the propagation of PLC bands.

Chapter 4　　　　Serration behaviors in various grain-sized high-Mn austenitic steels

4.1　　　Introduction

Grain refinement is one of the most effective ways to increase the yield strength of polycrystalline materials without addition of alloying elements. The relationship between yield strength and grain size is empirically described by the following equation, which is known as Hall-Petch relationship [47,48].

$$\sigma_y = \sigma_0 + k \cdot d^{-\frac{1}{2}} \tag{4.1}$$

where σ_y is the yield strength, σ_0 is friction stress, k is Hall-Petch coefficient and d is the mean grain size. According to the equation, yield strength increases in proportion to inverse square root of the mean grain size.

Recently, significant attention has been paid to increase the yield strength of high-Mn austenitic steels, whose yield strength is generally low due to their face-centered cubic (FCC) structure. In order to achieve grain refinement in bulk high-Mn austenitic steels having fully recrystallized microstructure, conventional rolling and subsequent annealing processes have been carried out. Ueji et al. [41] refined the grain size of a 31Mn-3Al-3Si alloy from 49.8 μm to 1.8 μm by applying cold-rolling and subsequent annealing process, and the yield strength of the material significantly increased form 220 MPa to 520 MPa with retaining high elongation over 48 % in the specimen with the mean grain size of 1.8 μm. Jo et al. [49] investigated the grain size dependence on mechanical properties of 18Mn-0.6C-1.5Si steels having various grain sizes from

4.5 μm to 49.8 μm.　　The material was deformed by applying both hot-rolling and cold-rolling, and the various grain sizes were obtained by controlling annealing condition.　　With grain refinement, the yield strength increased from 350 MPa to 620 MPa, and the ductility also increased, which resulted from the change of deformation mechanism from ε-martensitic transformation to deformation twinning.　　However, the minimum grain size so far obtained by the conventional rolling and subsequent annealing processes was limited to several micrometers.　　Recently, Tian et al. [50] have succeeded in fabricating fully recrystallized ultrafine grained (UFG) microstructures with average mean grain size of 576 nm in 22Mn-0.6C steel by applying repeated cold-rolling and subsequent annealing .　　It was noteworthy that the UFG steel exhibited superior strength and ductility balance with yield strength of 785 MPa, tensile strength of 1250 MPa and uniform elongation of 48 %.

　　As discussed in the section 1.2, many studies have been reported that DSA effect accompanying serration behavior was promoted under certain range of deformation temperature, strain rate and carbon concentration, where carbon atoms exerted a retarding force on mobile dislocations in the Cottrell atmosphere.　　However, few discussions have been carried out on the effect of grain size on the serration behavior especially in FCC alloys.　　Some researchers investigated the effect of grain refinement on the onset strain for serrated flow, at which serrated flow started to appear in the stress-strain curves.　　According to Charnock [34], the onset strain of serration behavior of various grain-sized Cu-Zn30 alloy (d_{mean}=4 to 200 μm) decreased with grain

refinement.　The author attributed the early onset of serration behavior in the fine-grained specimens to both decrease of dislocation velocity and increase of dislocation density.　On the other hand, McCormick [51] found out that the onset strain of various grain-sized 6063 aluminium alloy (d_{mean}=46 to 650 μm) was independent of grain size, and he considered that the grain size may have minor effect on the dislocation density or velocity.　Koyama et al. [52] investigated the effect of grain refinement on the onset strain of serration behavior in high-Mn austenitic steel (d_{mean}=3.5 to 44 μm), and it was found out that the onset strain of serration behavior increased with grain refinement.　According to the authors' explanation, dislocation extension was suppressed by grain refinement, and hence dislocation multiplication rate was decreased due to easier cross-slip of dislocation, resulting in the increase of the onset strain of serration behavior.　The result is the complete opposite to the report from Charnock.　The reports regarding the effect of grain refinement on the serration behavior were few in number and even lack coherence.　As was shown in **Fig. 2.12 (a)**, it should be also noted that serration peaks at the very early stage of deformation were so small that the analysis solely done from stress-strain curves could lead to a misinterpretation of the effect of grain refinement on the serration behavior.　In addition, the grain refinement in the previous reports was limited to micrometers, and the serration behavior in the UFGed microstructures has never been discussed.

In the present study, the 22Mn-0.6C steels with a wide range of mean grain sizes, of which minimum grain size was 0.86 μm, are fabricated through the repeated cold rolling and subsequent

annealing process.　The effect of grain refinement on the serration behavior was systematically investigated by analyzing both serrated flow in the stress-strain curves and the local PLC banding in the DIC strain-rate maps.

4.2　Experimental procedures

4.2.1　Materials

A 22Mn-0.6C steel (wt. %) was used in the present study.　The detailed chemical composition of the steel is shown in **Table 2.1**.　The as-received hot-forged plate 12 mm in thickness was subjected to 4 cycles of the cold-rolling and annealing processes, in order to fabricate the specimens with various mean grain sizes including the UFG microstructures ($d_{mean} \leq 1$ μm). The thickness reduction at each cold-rolling step was 33.3 %, 37.5 %, 40 % and 66.7 %, respectively, and the final thickness of the sheet was 1 mm.　The intermediate annealing between each cold-rolling step was performed at 600 °C for 600 s for restoring deformability of the material.　The materials were water-cooled immediately after intermediate annealing.　The specimens with various grain sizes ranging from 0.86 μm to 17 μm were successfully fabricated by changing final annealing condition, as illustrated in **Figure 4.1**.
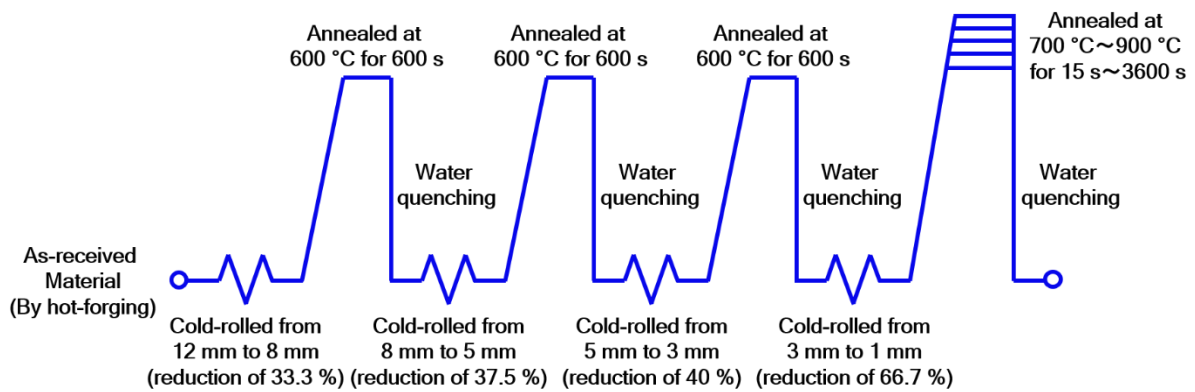
Fig. 4.1 Schematic illustration of thermomechanical process performed to 22Mn-0.6C steel.

4.2.2 Microstructure observation

After the repeated cold-rolling and annealing processes, microstructural observations were

carried out on a section perpendicular to the transverse direction (TD) of the sheet using a field-

emission scanning electron microscope (FE-SEM: JEOL, JSM-7800F) equipped with a back-

scattered electron (BSE) detector operated at an accelerating voltage of 15 kV.   In order to obtain

mirror-like surfaces, the TD section of the sheet was mechanically polished first by the use of 1000-

400 grit-sized fine SiC papers and then electro-polished in a solution of 10 % $HClO_4$ + 90 % C_2H_6O.

The mean grain size was determined by a line intercept method on the BSE images, counting

annealing twin boundaries and high angle grain boundaries having sharp contrast with neighboring

grains.

For the detailed analysis of the phase and texture, the microstructures were observed by a

FE-SEM (JEOL, JSM-7100F) equipped with an electron backscattering diffraction (EBSD)

detector.   Surface treatment to obtain mirror-like surfaces was performed in the same manner with

the observation for the SEM-BSE.   EBSD observation was carried out with a working distance of

15 mm at an accelerating voltage was 15 kV.   Obtained data were analyzed using TSL softwares

(TSL-OIM data collection, analysis ver. 5.31).   Confidence index (CI) values smaller than 0.1 was

eliminated in order to exhibit only reliable EBSD data.

4.2.3 Tensile test

In order to evaluate the mechanical properties of the 22Mn-0.6C steels with the various

mean grain sizes, tensile test was performed at an initial strain rate of 8.3×10^{-4} s^{-1} at room

temperature using a uniaxial tensile testing machine (SHIMADZU, AG-100kN Xplus).   As shown

in **Figure 2.2**, sheet-type tensile specimens with a gage length of 10 mm, gage width of 5 mm and

thickness of 1 mm were cut from the sheet by an electrical discharge machine.   The tensile

direction was parallel to the rolling direction (RD) of the sheet.

4.2.4 Digital image correlation (DIC) technique

In order to evaluate distributions of local strain and strain rate during the tensile tests of the

various grain-sized tensile specimens, a DIC technique was applied.   Prior to the tensile test, all

the specimens were first painted white and sprayed with black speckle patterns by using an airbrush,

as was shown in **Figure 2.3**.   The speckle patterns were deformed together with the tensile

specimens and used as markers to track displacements of different positions in the specimens.

During the tensile deformation, the speckle patterns were recorded at a rate of 5 frames per second

by a CCD (charge-coupled device) camera with a resolution of 2432 × 2054 pixels.   As was

described in **Fig. 2.4**, two-dimensional strain tensors at different positions were obtained by

differentiating displacement vectors obtained by tracking the speckle patterns.   The recorded CCD

images were analyzed by the use of Vic-2D software with a subset of 29 pixels in a square and a

step size of 7 pixels, which was optimized for assessing local strains and strain rates under the given

resolution of the CCD camera.   For obtaining global tensile strain, the imaginary extensometer

was set along the gage part, and the global tensile strain was precisely measured.

4.3   Results and discussion

4.3.1 Microstructures of the specimens with the various mean grain sizes

Figure 4.3 (a) − (g) shows SEM-BSE images of the 22Mn-0.6C steels with the various

mean grain sizes ranging from 0.86 μm to 17 μm, which were obtained by changing the final

annealing condition after the 4 cycles of cold rolling and annealing processes.   The

microstructures were observed on a longitudinal plane perpendicular to TD of the sheet.   All

microstructures showed homogeneous and equiaxed grains containing a large number of annealing

twins.   The contrasts in each grain were homogeneous, indicating that the microstructures were

fully recrystallized.   Considerable grain refinement down to UFG region (**Fig. 4.3 (a)**) with fully

recrystallized microstructure was successfully achieved even at the short annealing time 15 s because high density of nucleation sites were introduced after the repeated cold-rolling and annealing processes.

Figure 4.4 (a) – (c) shows EBSD phase maps of the representative specimens having UFG of 0.86 μm, medium grain (MG) of 5.1 μm and coarse grain (CG) of 17 μm, respectively. The microstructures were observed from the same direction as the SEM-BSE images (**Fig. 4.3**). Yellow color indicates FCC structure confirmed from the Kikuchi-line diffraction pattern obtained at each point. All areas in each image showed yellow color, i.e., FCC structure, which indicated that the specimens had an austenite singe-phase structure. Low angle grain boundaries ($2° \leq \theta < 15°$), high angle grain boundaries ($15° \leq \theta < 180°$) and annealing twin boundaries ($\sum 3$ boundaries) are drawn by green lines, black lines and red lines, respectively. For all the specimens, almost all grains were surrounded by high angle grain boundaries, and a large number of annealing twin boundaries were observed as well.

Figure 4.5 shows (001), (011) and (111) pole figures of the representative specimens, which was rotated from the EBSD data (**Fig. 4.4 (a) – (c)**) so that ND lies at the center of the pole figures. All the pole figures of the specimens exhibited low intensities, indicating that the specimens fabricated by the repeated cold-rolling and annealing processes did not have strong crystallographic texture.
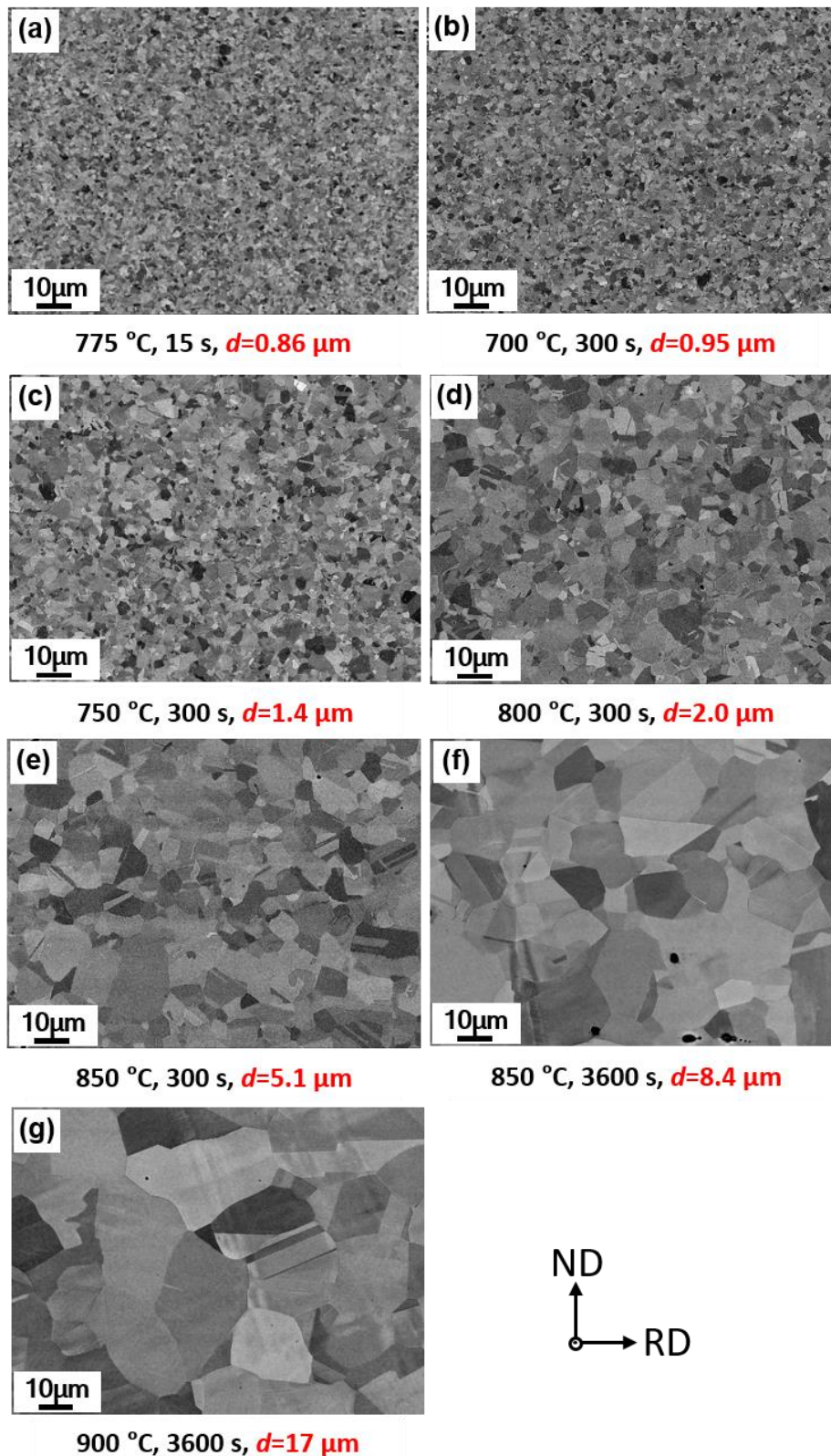
Fig. 4.3 SEM-BSE images of the fully recrystallized microstructures with various mean grain sizes of (a) 0.86 μm, (b) 0.95 μm, (c) 1.4 μm, (d) 2.0 μm, (e) 5.1 μm, (f) 8.4 μm and (g) 17 μm. The annealing conditions and the corresponding mean grain sizes are indicated at the bottom of each image.
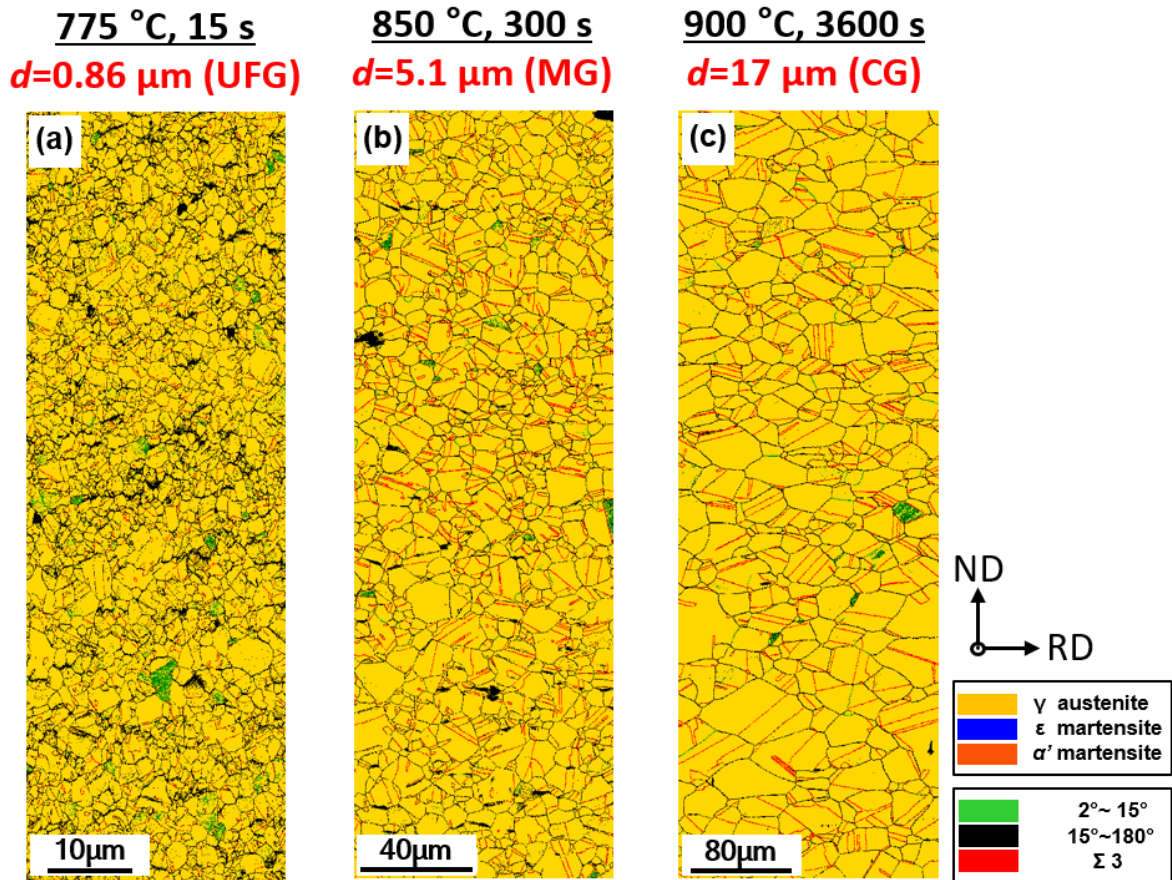
Fig. 4.4 EBSD phase maps of the representative specimens with the mean grain sizes of (a) 0.86 μm (UFG), (b) 5.1 μm (MG) and (c) 17 μm (CG). Phases and the grain boundaries with different misorientation angles are shown in distinct colors as indicated at the bottom of the right side. The annealing conditions and the corresponding mean grain sizes are indicated above each image.

	775 °C, 15 s, *d*=0.86 μm	850 °C, 300 s, *d*=5.1 μm	900 °C, 3600 s, *d*=17 μm
(001) pole figure	Max=1.741	Max=2.154	Max=2.674
(011) pole figure	Max=1.696	Max=1.993	Max=2.428
(111) pole figure	Max=2.014	Max=2.432	Max=2.269
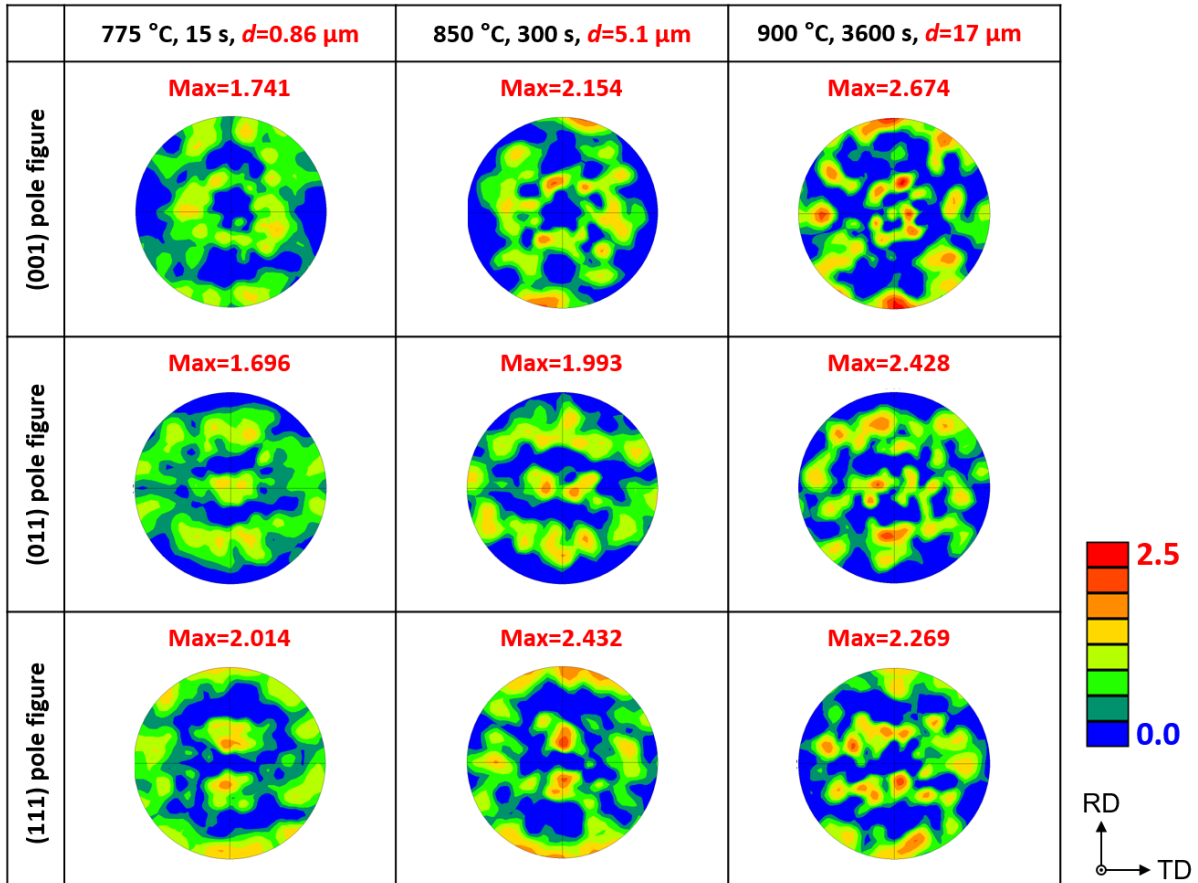
Fig. 4.5 (001), (011) and (111) pole figures of the representative specimens. The EBSD data in **Fig. 4.4** was rotated so that ND lies at the center of the pole figures.

4.3.2 Mechanical properties of the specimens with the various mean grain sizes

Nominal (engineering) stress-strain curves of the specimens with the various mean grain sizes ranging from 0.86 μm to 17 μm are shown with distinct colors in **Figure 4.6**.   It was clearly found that yield strength and tensile strength greatly increased with the grain refinement from 17 μm to 0.86 μm.   Yield strength (0.2 % proof stress) increased from 266 MPa to 703 MPa, and tensile strength increased from 981 MPa to 1236 MPa.   Total elongation decreased from 0.71 to 0.62 with the grain refinement, but it is notable that the UFG specimen still retained the large total elongation.   When the grain size was refined under 2.0 μm, small yield-drop accompanying

114

Lüders deformation was observed and it became more apparent in the UFG specimen with the mean grain size of 0.86 μm.　It is also notable that the post uniform elongation of the total elongation was quite small in all the specimens, indicating that the specimens were fractured soon after experiencing the necking.　As was discussed in the section 2.3.10, this was because the strain was localized much in the PLC bands at later stage of tensile deformation.　The mechanical properties obtained from the tensile tests are summarized in **Table 4.2**.

Serration behavior was observed on the stress-strain curves of all the specimens. Interestingly, the UFG specimen showed a weak serration behavior in the stress-strain curve, especially in the early stage of deformation (e= 0.05 ~ 0.25), whereas obvious serration behavior was found in the specimens having coarser grain sizes over the whole deformation.　As was introduced in the section 4.1, DSA accompanying serration behavior was more pronounced under certain strain rates, temperatures and carbon contents.　In other words, the serration behavior (or DSA) was suppressed outside of those certain conditions.　However, to the best of the author's knowledge, there was no single study reported that DSA (or serration behavior) was suppressed in the UFG region.　This unique feature would be discussed in the section 4.3.4.

Figure 4.7 (a) – (c) shows the strain hardening ($d\sigma/d\varepsilon$, blue) and true stress (σ, red) curves of the UFG, MG and CG specimens plotted as a function of true strain (ε).　All the specimens maintained high strain hardening rate above 2000 MPa until the later stage of deformation.　The intersection of the strain hardening rate curve and the true stress-true strain curve corresponds to

initiation of necking, which is also called plastic instability. Considère's criterion for plastic

instability is described as following formula [31].

$$\sigma \geq d\sigma/d\varepsilon \qquad\qquad (4.2)$$

where σ is the true stress, ε is the true strain and $d\sigma/d\varepsilon$ is the strain hardening rate,

respectively. Interestingly, the strain hardening rate curves (blue) of the MG and CG specimens

showed severe fluctuation intersecting the true stress-true strain curves (red), whereas that of the

UFG specimen rarely showed the intersection with the true stress-true strain curve except for later

stage of deformation. The severe fluctuation of the strain hardening rate in the MG and CG

specimens corresponded to the serrated flow observed on the stress-strain curve, and the small

fluctuation of the strain hardening rate in the UFG specimen corresponded to the weak serrated

flow in the stress-strain curve, as was shown in **Fig. 4.6**.
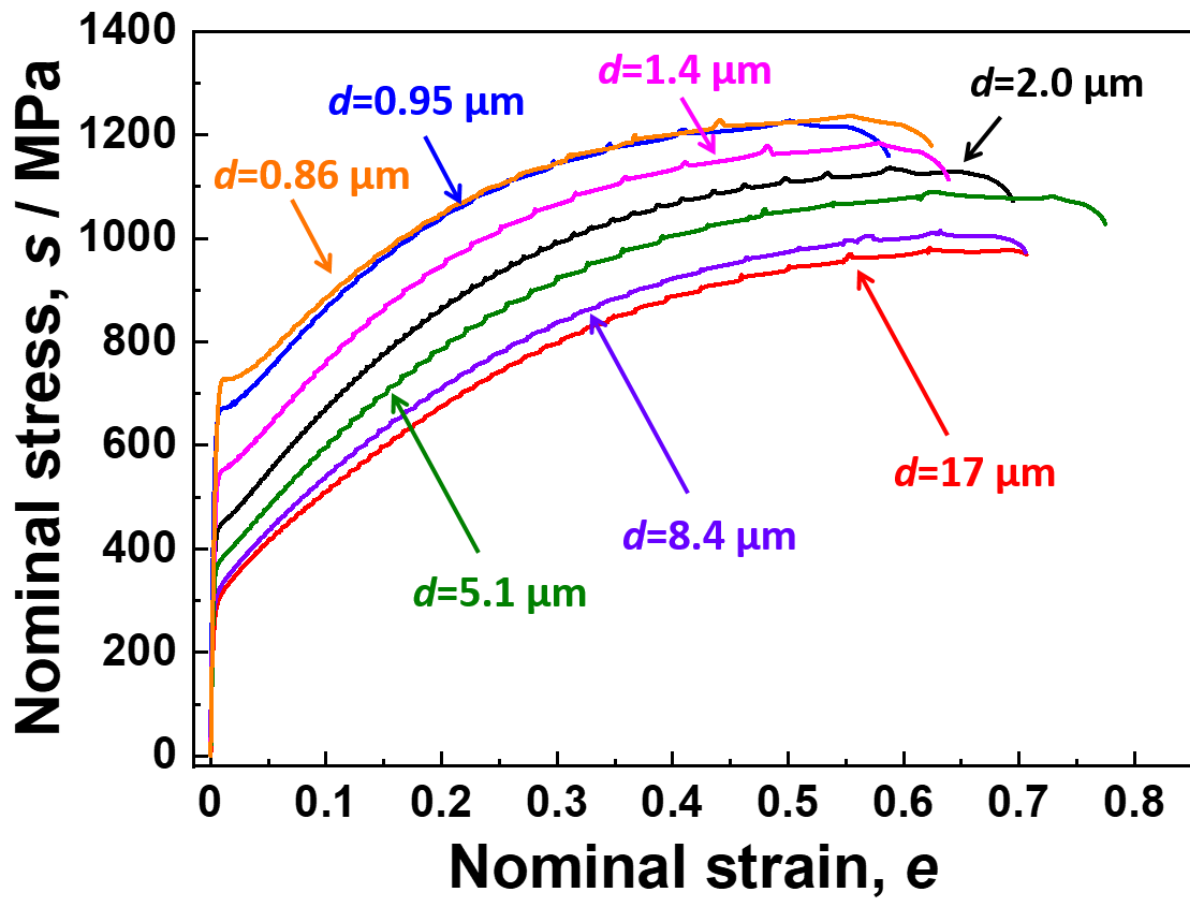
Fig. 4.6 Nominal stress-strain curves of the 22Mn-0.6C steel with various mean grain sizes.

Table 4.2 Mechanical properties of the 22Mn-0.6C steels with the various mean grain sizes.

Heat treatment condition	Mean grain size, d_{mean}/μm	Yield strength, σ_{YS} / MPa	Tensile strength, σ_{TS} / MPa	Total elongation, e_t	Uniform elongation, e_u	Post-uniform elongation, e_p
775° C, 15 s	0.86	703	1236	0.62	0.55	0.07
700° C, 300 s	0.95	654	1227	0.59	0.5	0.09
750° C, 300 s	1.4	529	1184	0.64	0.58	0.06
800° C, 300 s	2.0	430	1163	0.69	0.59	0.07
850° C, 300 s	5.1	354	1090	0.77	0.63	0.14
850° C, 3600 s	8.4	294	1015	0.71	0.63	0.08
900° C, 3600 s	17	266	981	0.71	0.62	0.09
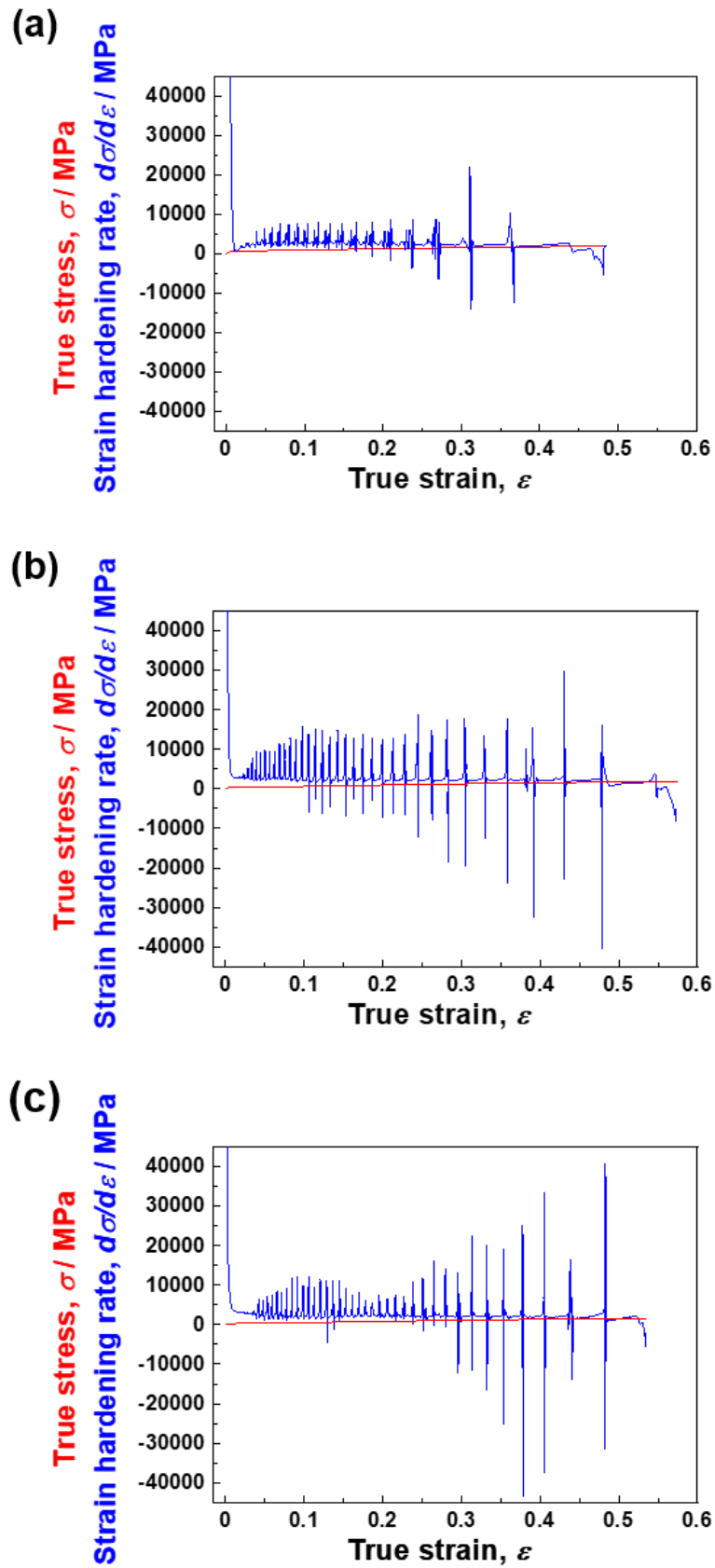
Fig. 4.7 Strain-hardening rate (blue) and true stress (red) curves plotted against true strain of (a) the UFG (d=0.86 μm), (b) MG (d=5.1 μm) and (c) CG (d=17 μm) specimens, respectively.

4.3.3 Grain size dependence on the onset strain of serration behavior

Many researches have focused on the onset strain of serration behavior, at which serrated flow started to appear in the stress-strain curves of the various alloys such as aluminum alloys [36], copper alloys [34], Ni alloys [53] and steels [52], and it was found in the studies that the onset strain of serration behavior was strongly dependent on solute concentration, temperature, strain rate, and dislocation density. Nakada and Keh [53] incorporated the effects of those variables on the onset strain of serration behavior (ε_c) in a carbon containing nickel alloy, and developed an empirical equation as follows.

$$\dot{\varepsilon} = KC^n \exp(-\frac{Q_M}{RT})\varepsilon_c{}^m \tag{4.3}$$

where $\dot{\varepsilon}$ is the strain rate, C is the solute concentration (wt. %), Q_M is the activation energy responsible for DSA (or serration), R is the gas constant, ε_c is the critical strain for the onset of serration, and K, n, m are experimental constants. In their study, the activation energy responsible for DSA (Q_M) was calculated to be the one half of that for bulk diffusion of carbon in nickel. They argued that small critical strain was necessary for de-pinning the carbons swept into the dislocation core in the early stage of plastic deformation. The constant m is associated with the multiplication of both dislocation and vacancy, and the authors considered that dislocation multiplication plays a much bigger role than vacancy generation in determining m value for the alloys having interstitial atoms.

The grain size dependence on the onset strain of serration behavior of the 22Mn-0.6C steel

was investigated in wide range of grain sizes, where the finest grain size was 0.86 μm, and the

results are shown in **Figure 4.8**. In **Fig. 4.8 (a)**, the first serration peaks are enlarged from the

stress-strain curves of the various grain-sized specimens (**Fig. 4.6**) and indicated by arrows. The

strain at the first serration peak in the stress-strain curve (ε_c^{ss}), was plotted as a function of mean

grain size (d_{mean}) in **Fig. 4.8 (b)**. The data points of the specimens with the mean grain sizes of

2.0 μm, 5.1 μm and 8.4 μm in **Fig. 4.8 (b)** represent the average value of two tensile-tested

specimens. It was clearly found that the (ε_c^{ss}) decreased with grain refinement from 17 μm to 1.4

μm. On the other hand, the ε_c^{ss} increased steeply with further grain refinement from 1.4 μm to

0.86 μm. The increase of the ε_c^{ss} with grain refinement in the UFG region could be presumably

attributed to the Lüders strain in the strain-strain curves in **Fig. 4.8 (a)**. For the detailed

investigation, the onset strain was newly determined by the first appearance of the PLC band (ε_c^{PLC})

in DIC strain and strain-rate maps. In order to characterize the first appearance of PLC band, a

point in the gage part was set in the DIC strain and strain-rate maps, as in the same manner shown

in **Fig. 2.15**, and changes of local strain and the local strain rate at this point at early stage of

deformation ($t \leq 160$ s) was plotted for the UFG, MG and CG specimens in **Fig. 4.8 (c)**, as a

function of the experimental time. Interestingly, the height of the first peak in the UFG was much

larger than that of the following peaks. The intrinsic difference between PLC band and Lüders

band is still unclear, especially regarding the work-hardening behavior in the stress-strain curves

and the repeatability of the bands. It was reported in the medium Mn steels [54] that the

magnitude of strain localization in the Lüders bands reached to 0.0245, whereas that in the PLC bands was only around 0.0078 at the early stage of deformation. Therefore, the larger strain localization within the duration of the first strain-rate peak in the UFG specimen was considered to result from the Lüders band, not a PLC band. The onset strain determined by the first appearance of the PLC band (ε_c^{PLC}) was plotted as a function of mean grain size in red points in **Fig. 4.8 (d)**. The appearance of Lüders bands, i.e., the first strain-rate peak in the specimens with the mean grain sizes of 0.86 μm and 0.95 μm, were also plotted as blue points. Here, two criterions were concerned to characterize the PLC bands: (1) intensity of the strain-rate peak of the nucleated PLC bands was larger than 0.001, and (2) the nucleated PLC bands should propagate to the neighboring region. It was found that ε_c^{PLC} was always smaller than the ε_c^{ss} (**Fig. 4.8 (b)**) at the identical grain sizes. It was because serration peaks at the very early stage of deformation was so small that some early serration peaks were hard to be detected, and serration peak was naturally followed after the formation and propagation of the PLC bands, as was discussed in the section 2.3.4. Similar to the change of ε_c^{ss} with grain refinement in **Fig. 4.8 (b)**, the ε_c^{PLC} also decreased with grain refinement from 17 μm to 2.0 μm, and the ε_c^{PLC} increased steeply with further grain refinement from 1.4 μm to 0.86 μm. Even counting the first strain-rate peak in the UFG specimens that corresponded to the Lüders bands, the ε_c also increased with grain refinement within the UFG region. In the equation (4.3), $\dot{\varepsilon}$ and C are constant values in the present study, and K and Q_M are assumed not to vary in the same material. Since n is related with the effect of solute

concentration (C) on strain rate ($\dot{\varepsilon}$), it is considered not to vary with the grain size of the specimens, in which the same amount of carbons (0.6 wt.%) was contained. Therefore, m, dislocations multiplication for the alloys having interstitial atoms, is considered to be the only variable that changes with grain size of the material.

Narutani et al. [55] revealed that the dislocation density in pure nickel increased with grain refinement by measuring electrical resistivity of the deformed material, and they considered the increase of dislocation density with grain refinement lead to an increase of flow stress. Therefore, the decrease of ε_c (both ε_c^{ss} and the ε_c^{PLC}) with grain refinement from 17 μm to 1.4 μm was attributed to the increase of dislocation density, which naturally increases the chance of interaction with carbon atoms. Within the range of the grain refinement from 17 μm to 1.4 μm, the tendency in the present study was consistent with the previous report by Charnock [34], in which ε_c also decreased with grain refinement from 200 μm to 4 μm in the Cu-Zn30 alloy. On the other hand, the ε_c steeply increased with further grain refinement from 1.4 μm to 0.86 μm. The inverse grain size dependence on the ε_c (considering both Lüders and PLC bands) in the UFG region can probably be attributed to the lack of dislocation sources in the grain interior. Kitamura et al. [56] found out that extra Hall-Petch hardening occurred in the UFGed TWIP steel (d=0.79 μm), and the authors attributed it to the scarcity of dislocation sources in each UFG grain. In the equation (4.3), dislocation multiplication (m) was regarded to be the only variable that determines the onset strain of serration behavior in the present material. Therefore, the late appearance of serration behavior

(DSA effect) in the present UFG specimens probably resulted from lack of the dislocation sources in the early stage of deformation, naturally lowering the chance of dynamic interaction with carbons.

However, in the present study, experimental verification was not provided regarding the mechanism of dislocation multiplication in the UFG specimens as well as the MG and CG specimens, and further experiments are necessary to clarify the grain size dependence on ε_c of serration behavior.
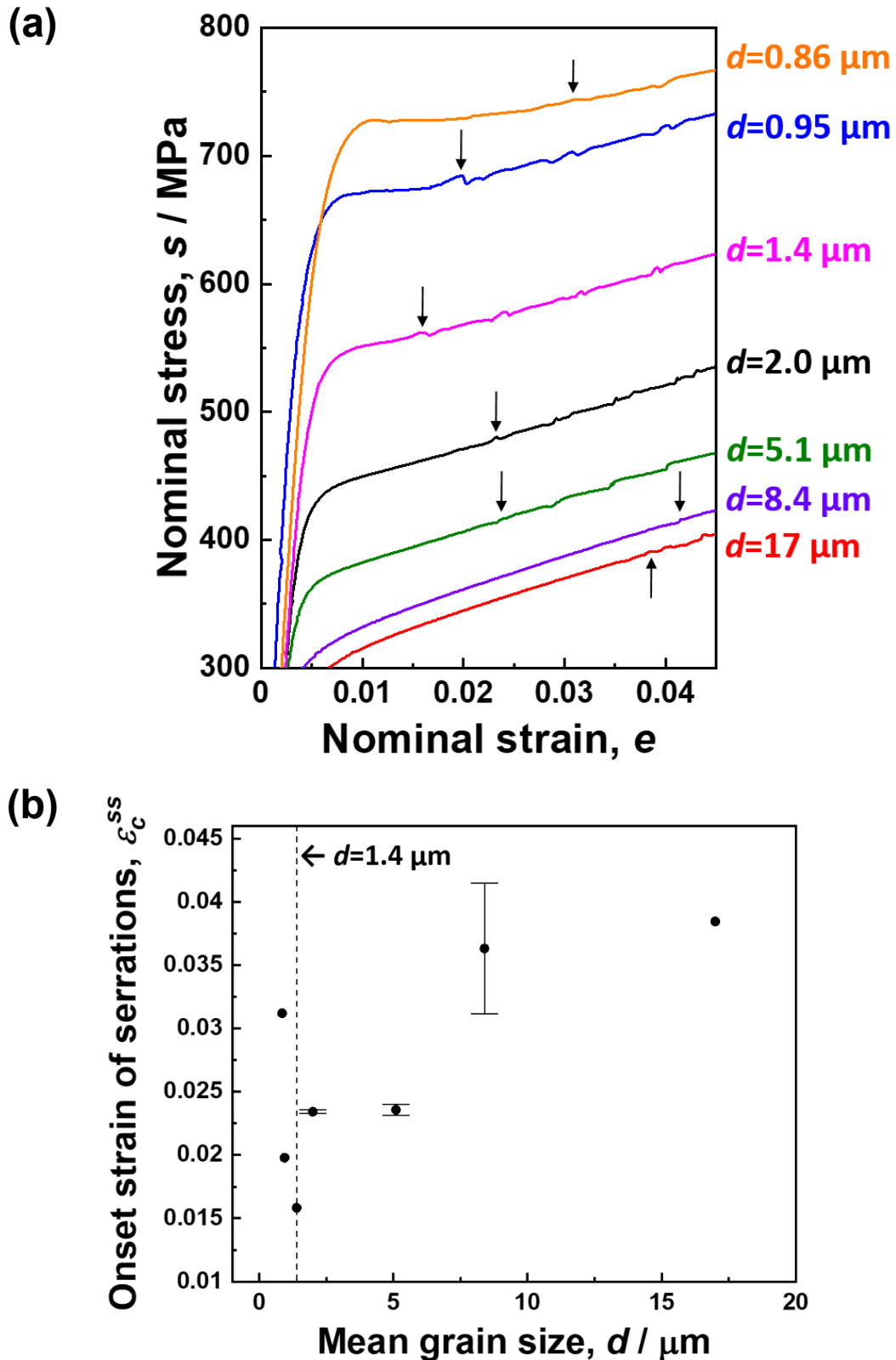
Fig. 4.8 (a) The first serration peaks of the various mean grain-sized specimens, enlarged from **Fig. 4.1**. The first serration peaks are indicated by arrows. (b) The change of onset strain of serration behavior (ε_c^{ss}) as a function of the mean grain size. The vertical dashed line indicates the mean grain size of 1.4 μm.
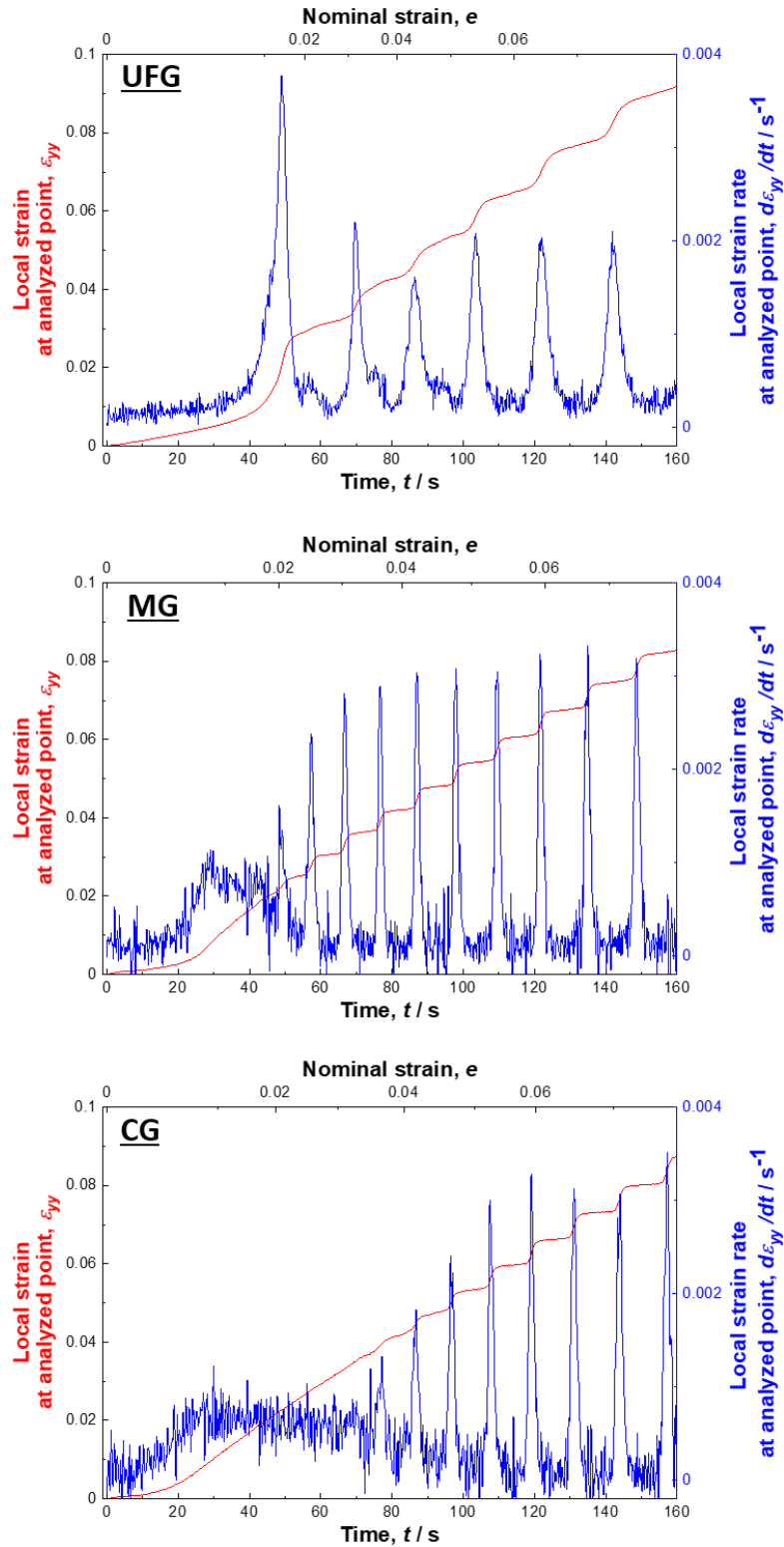
Fig. 4.8 (c) Changes of the local strain (red) and strain rate (blue) at a point set in the gage part of the DIC maps at early stage of deformation ($t \leq 160$ s) in the UFG (d=0.86 μm), MG (d=5.1 μm) and CG (d=17 μm) specimens, respectively, plotted as a function of experimental time. Corresponding global nominal stress is also indicated in the upper x-axis.
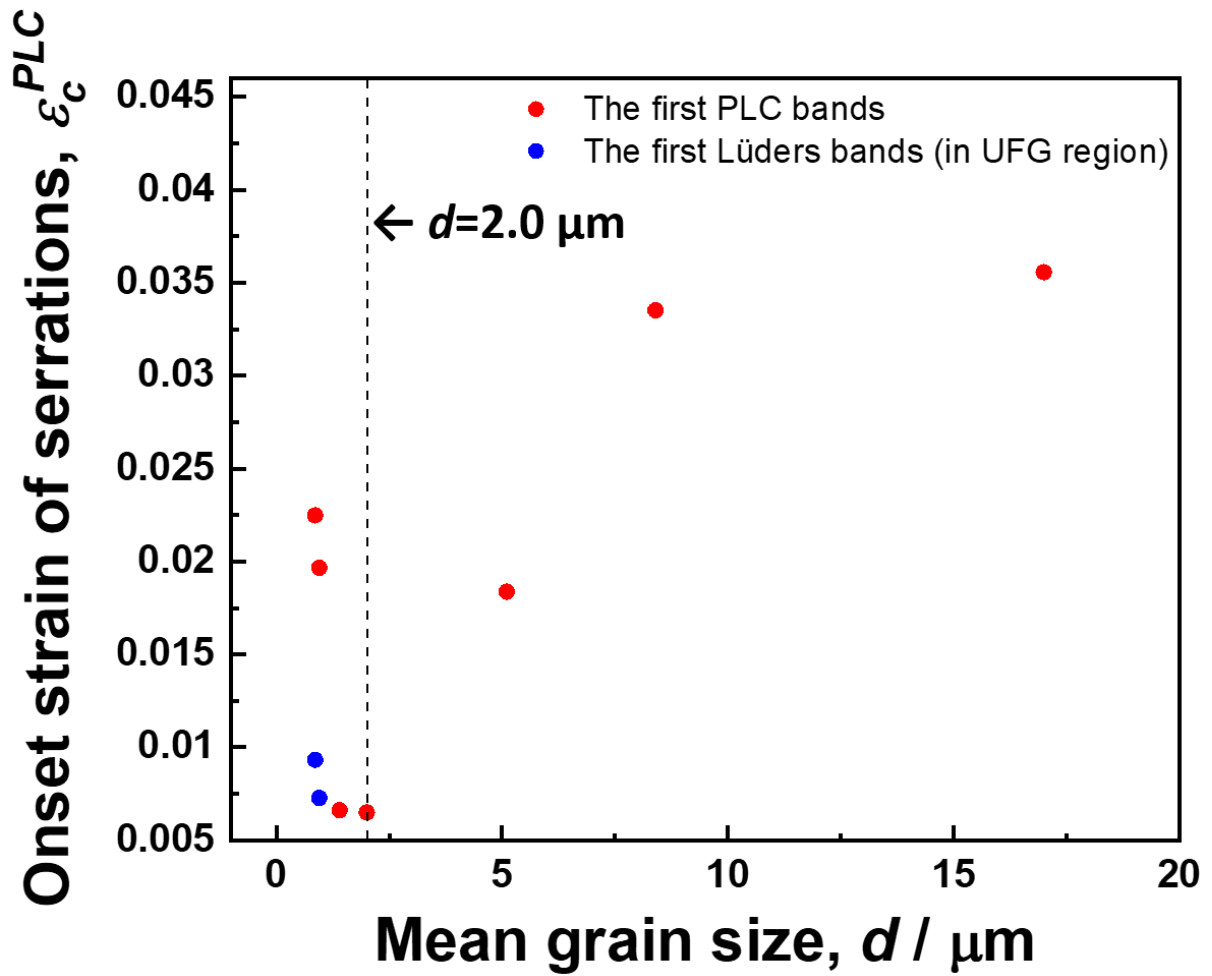
Fig. 4.8 (d) The change of onset strain of serration behavior determined by the first appearance of PLC bands (ε_c^{PLC}), plotted as a function of the mean grain size as red points. The appearance of Lüders bands in the UFG region was also plotted in the graph as blue points. The vertical dashed line indicates the mean grain size of 2.0 μm.

4.3.4 Characterization of the PLC banding in the various grain-sized specimens

It was clarified in the Chapter 2 that plastic deformation was localized in the propagating PLC band, and such sequential deformation, i.e., the PLC banding, lead to the work-hardening of the present material.   In the current section, the effect of grain refinement on the PLC banding would be discussed from the view point of the different work-hardening behavior.

The serration peak was the response of the formation of the PLC band (**Fig. 2.14 (b)**), so the interval strain between serration peaks corresponded to that between the formation of the PLC bands. **Figure 4.9** shows the change of the interval strain between serration peaks of the various grain-sized specimens as a function of global nominal strain. The interval strain between serration peaks was obtained from the stress-strain curves of the various grain-sized specimens (**Fig. 4.6**). The interval strain between serration peaks would be termed period, hereafter. Interestingly, it was clearly found that the period increased with grain refinement, except for the specimen with the mean grain size of 2.0 μm (black dots and line). In addition, the periods increased with deformation for all the specimens. The periods of the various grain-sized specimens were commonly as small as 0.001 ~ 0.01 at early stage of deformation, but they increased to over 0.06 at later stage of deformation. The increase of the period with deformation indicated that it took more time (or global strain) for PLC band to propagate along the tensile specimen. For the detailed investigation, PLC band velocity was investigated on the various grain-sized specimens. **Figure 4.10 (a)** and **(b)** shows the representative analysis performed on the specimen with the mean grain size of 5.1 μm. Two points (P1 and P2) were first set in the DIC strain-rate map in **Fig. 4.10 (a)**, and an imaginary extensometer was set between the two points in the DIC strain-rate map, for obtaining the change of the distance between the two points with deformation. The changes of local strain rate at the two points in **Fig. 4.10 (a)** were investigated in **Fig. 4.10 (b)**, for identifying the PLC band position that appeared as sharp peak, and the time difference between two strain-rate

peaks were measured.   From the distance that PLC band propagated and the time that it took, PLC band velocity was calculated.   Those measurements were performed for all the specimens over the entire deformation, and finally the PLC band velocity of the various grain-sized specimens is plotted as a function of nominal strain in **Fig. 4.10 (c)**.   Contrary to the change of period with the grain refinement in **Fig. 4.9**, the PLC band velocity decreased with deformation for all the specimens.   The specimen with the mean grain size of 2.0 μm also followed the tendency that the PLC band velocity increased with grain refinement.   This was because the PLC band in the specimen with the mean grain size of 2.0 μm nucleated near the gage center and swept the half of the gage part at a time, forming two serration peaks at one cycle of PLC band propagation.   The PLC band velocity of the various grain-sized specimens was as fast as 0.8 ~ 1.6 mm/ s at early stage of deformation, but commonly decreased to 0.1 ~ 0.3 mm/ s at late stage of deformation. The decrease of the PLC band velocity can be attributed to the decrease of the strain hardening capability with deformation, needing more time to accumulate and activate dislocations in the PLC band.   It was also found that the PLC band velocity at identical global nominal strains decreased with grain refinement.   At early stage of deformation (e~0.1), the PLC band velocity in the UFG specimen was 0.61 mm/ s, whereas the PLC band in the CG specimen was 1.0 mm/ s.   At late stage of deformation (e~0.5), the relative difference became widened that the PLC band velocity in the UFG specimen was 0.11 mm/ s and that in the CG specimen was 0.25 mm/ s.   Few studies were reported regarding the change of the PLC band velocity with grain refinement.   Charnock

[34] reported that the period increased, i.e., PLC band velocity decreased, with grain refinement in the Cu-30Zn alloy.   Even concrete experimental verification was not provided in the study, the author considered that a capability to unlock the dislocation pinning or to create a dislocation source should differ depending on the grain size.
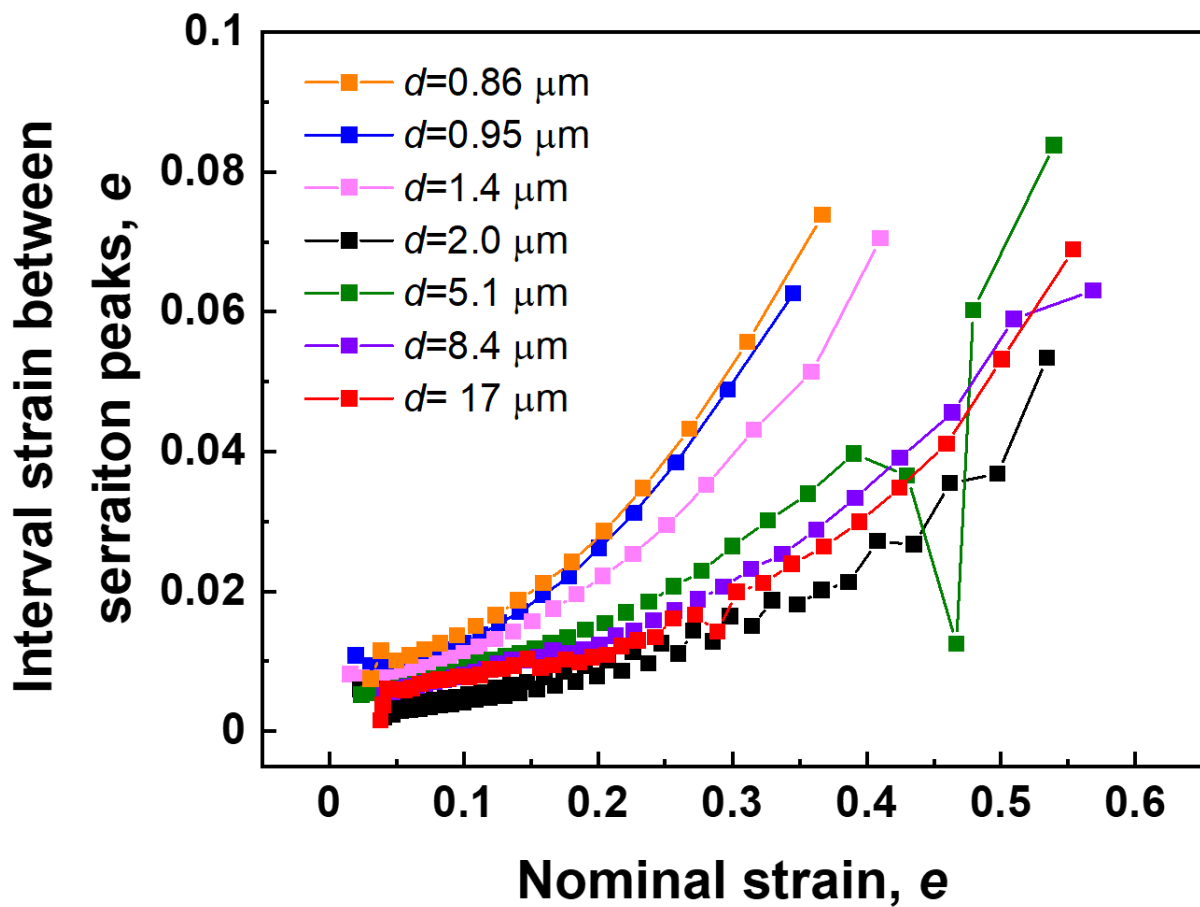
Fig. 4.9 The interval strain between serration peaks (period) of the various grain-sized specimens, plotted as a function of global tensile strain.
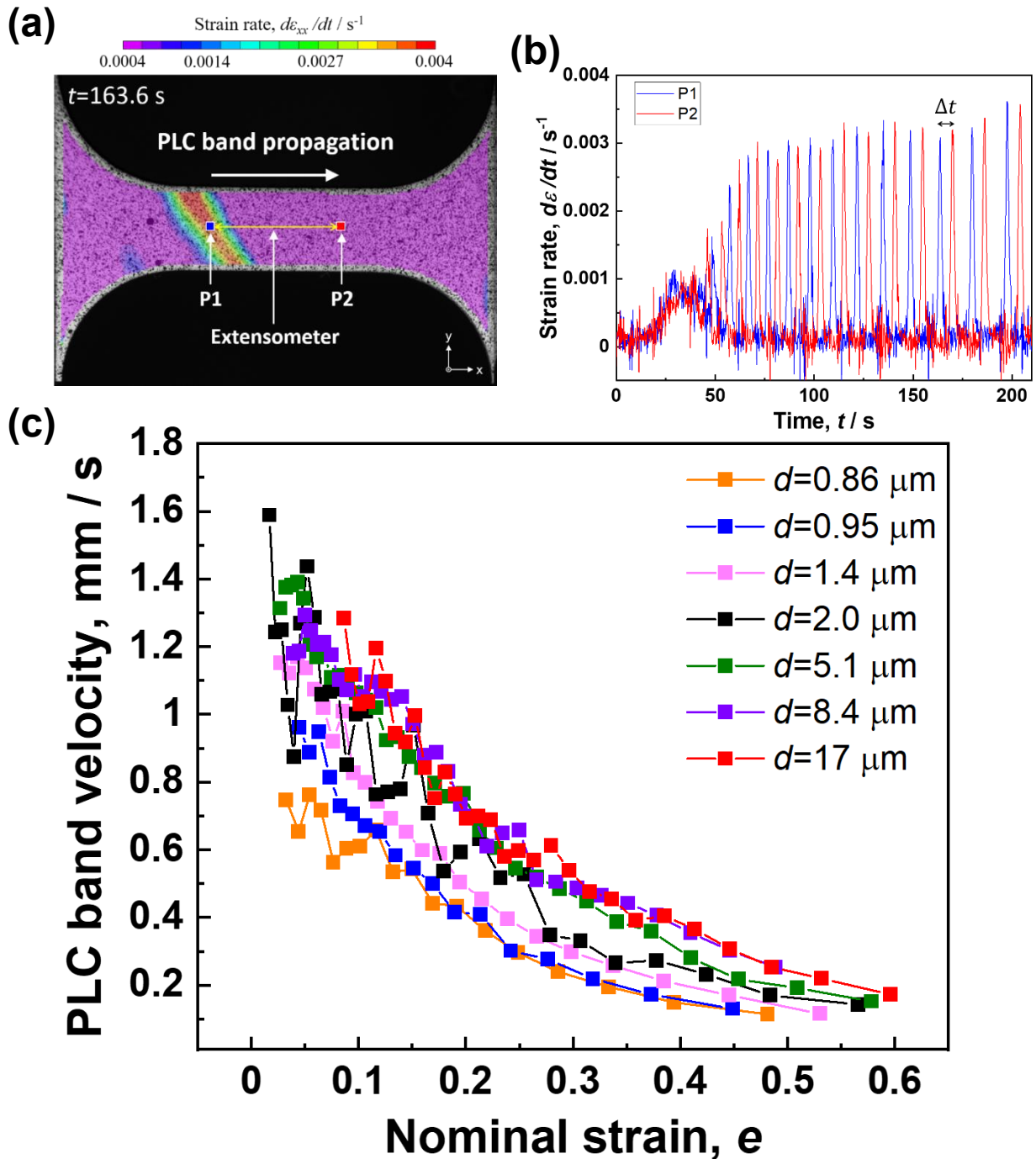
Fig. 4.10 (a) In the DIC strain-rate map of the specimen with the mean grain size of 5.1 μm, two points (P1 and P2) were set in the gage part, and an imaginary extensometer was drawn between the two points. (b) The profile of the local strain rate at the two points from 0 s to 200 s were extracted. The sharp peak corresponded to the passage of PLC band through the two points, and the time difference (Δt) corresponded to the time that PLC band took from point P1 to point P2. (c) The PLC band velocity of the various grain-sized specimens, plotted as a function of global tensile strain.

130

In order to investigate the grain size dependence on the PLC banding in more detail, strain localized in the PLC band in the specimens with the various mean grain sizes was plotted in **Figure 4.11**. The strain localized in the PLC band was obtained by measuring the strain increment during the duration of the local strain-rate peak at an analyzed point, as shown in **Fig. 4.11 (a)**. For all the specimens, the strain localized in the PLC band increased with deformation, which was the opposite tendency that the PLC band velocity decreased with deformation. As was discussed in the section 2.3.9, the PLC band only propagated after the region within the PLC band was sufficiently strain-hardened and the force balance was achieved between the regions within the PLC band and beyond the PLC band. That is, the magnitude of the strain localized in the PLC band indicated how much the strain-hardening should be achieved within the PLC band. Therefore, the increase of the strain localized in the PLC band with deformation indicated that more strain-hardening should be achieved within the PLC band as the deformation proceeded. Interestingly, it was also found that the strain localized in the PLC band generally increased with the grain refinement. The result indicated that more strain-hardening should be achieved within the PLC band with the grain refinement. **Figure 4.12 (a)** and **(b)** shows the change of local strain (ε_{yy}) and the local strain rate ($d\varepsilon_{yy}/dt$) at a point in the gage part, in the same manner shown in **Fig. 2.15**, of the UFG specimen and CG specimens, respectively. As was clarified in the section 2.3.5, the sudden increase of the local strain corresponded to the durations when each PLC band was passing through the point, which appeared as the sharp strain-rate peak. The local strain at

the analyzed point in the CG specimen (**Fig. 4.12 (b)**) increased in stepwise manner, whereas the steps of the local strain in the UFG specimen (**Fig. 4.12 (b)**) was somehow blunt, especially in the early and mid stage of the deformation.   For the detailed investigation, the early stage of deformation (t=60 s ~ 130 s), mid stage of deformation (t=300 s ~ 450 s), late stage of deformation (t=650 s ~ 950 s) of the UFG and CG specimens were enlarged in **Fig. 4.12 (c)** and **(d)**, respectively. Interestingly, the slope of the local strain between neighboring steps in the UFG specimen was larger than that in the CG specimen at every deformation stage.   The slope of the UFG specimen was 3.7×10^{-4} s^{-1} at early stage of deformation (t~95 s), 2.9×10^{-4} s^{-1} at mid stage of deformation (t~375 s) and 2.2×10^{-4} s^{-1} at late stage of deformation (t~754 s), whereas the slope of the CG specimen in each deformation stage was 2.2×10^{-4} s^{-1} (t~91 s), 1.1×10^{-4} s^{-1} (t~366 s) and 1.0×10^{-4} s^{-1} (t~744 s).   The quite large slope between neighboring steps in the UFG specimen indicated that the deformation was still occurring beyond the PLC band. In addition, the local strain rate between neighboring steps of the UFG specimen was far above 0, which was drawn as pink broken line in **Fig. 4.12**, whereas that of the CG specimens was close to 0.   The higher local strain rate in the UFG specimen consistently explained that the deformation was still occurring beyond the PLC band.   The results indicated that the force difference between beyond the PLC band and within the PLC band became widened, and the region within the PLC band should be strain-hardened more to make the force balance with the region beyond PLC band. This explains the increase of the strain localized in the PLC band with the grain refinement, as was

shown in **Fig. 4.11**. The decrease of the PLC band velocity, i.e., more time needed to be strain-hardened, with the grain refinement (**Fig. 4.10 (c)**) was consistently understood in such a way.
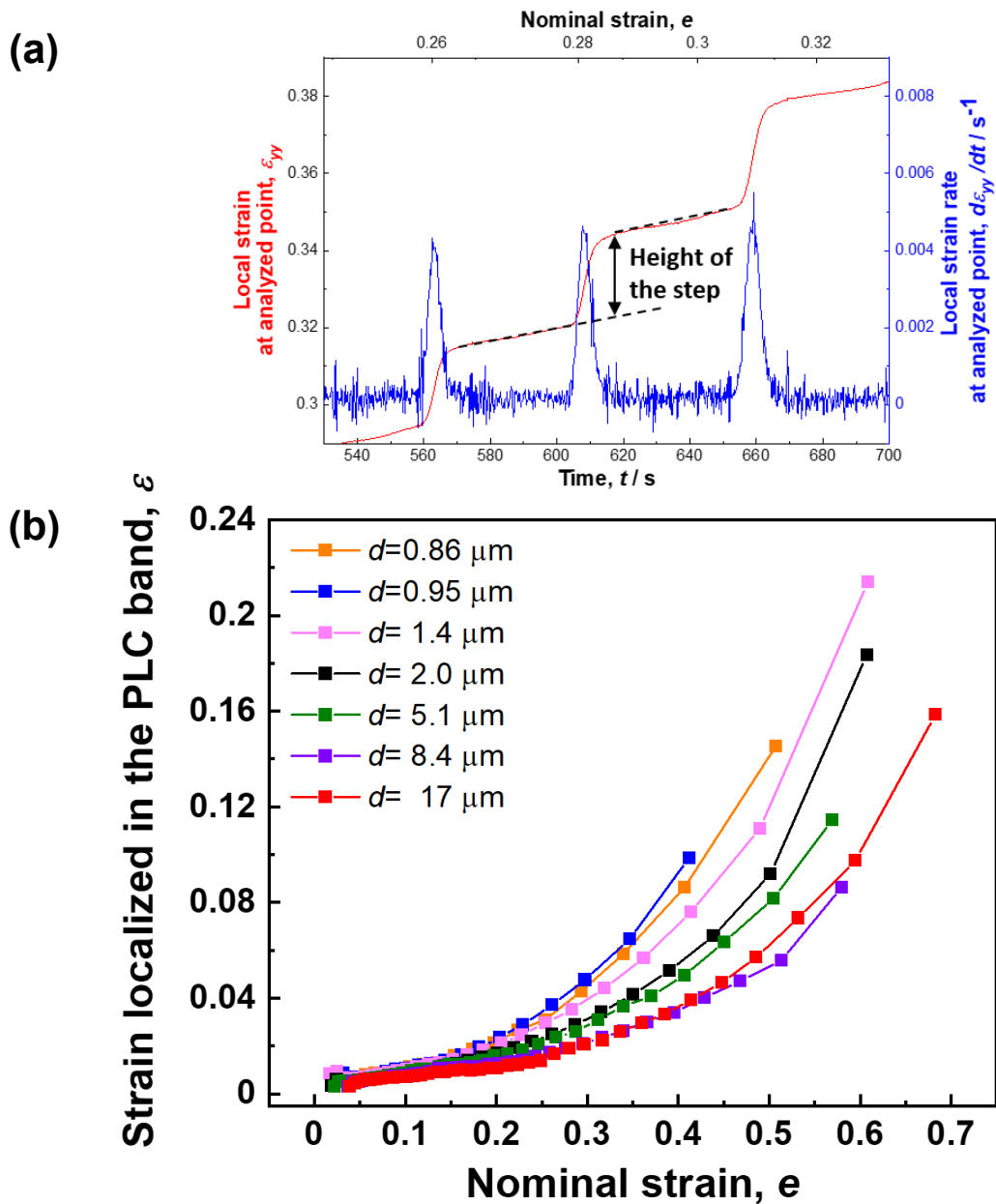
Fig. 4.11 (a) A representative measurement of the strain localized in the PLC band, performed on the profile of the local strain and strain rate of the specimen with the mean grain size of 5.1 μm. The strain localized in the PLC band corresponded to the height of the step. (b) Strain localized in the PLC band of the various grain-sized specimens, plotted as a function of global tensile strain.
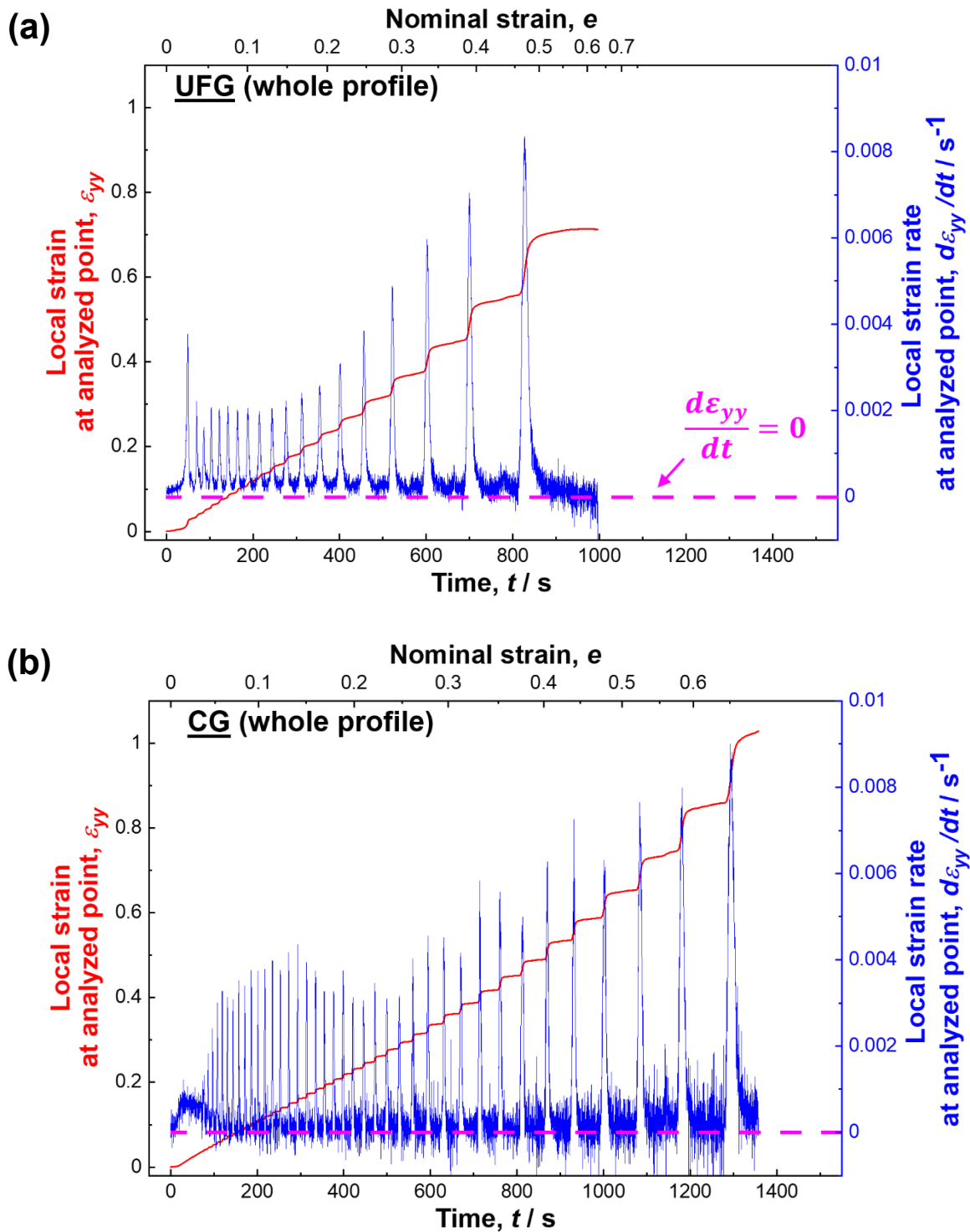
Fig. 4.12 The whole changes of the local strain (red) and strain rate (blue) at a certain point set in the gage part of the DIC maps of (a) the UFG and (b) CG specimens, respectively, plotted as a function of experimental time. Corresponding global nominal strain is also indicated along the upper x-axis. Enlarged profiles of the local strain and strain rate of (c) the UFG and (d) CG specimens at early stage of the deformation from 60 s to 130 s, mid stage of the deformation from 300 s to 450, and late stage of deformation from 650 s to 950 s, respectively. Slopes of the local strain-time curve are indicated by black triangles.

(c)

Nominal strain, *e*

UFG (early stage of deformation)

$$\frac{\Delta \varepsilon_{yy}}{\Delta t} = 3.7 \times 10^{-4} \ s^{-1}$$

Local strain at analyzed point, ε_{yy}

Local strain rate at analyzed point, $d\varepsilon_{yy}/dt$ / s⁻¹

Time, *t* / s

Nominal strain, *e*

UFG (mid stage of deformation)

$$\frac{\Delta \varepsilon_{yy}}{\Delta t} = 2.9 \times 10^{-4} \ s^{-1}$$

Local strain at analyzed point, ε_{yy}

Local strain rate at analyzed point, $d\varepsilon_{yy}/dt$ / s⁻¹

Time, *t* / s

Nominal strain, *e*

UFG (late stage of deformation)

$$\frac{\Delta \varepsilon_{yy}}{\Delta t} = 2.2 \times 10^{-4} \ s^{-1}$$

Local strain at analyzed point, ε_{yy}

Local strain rate at analyzed point, $d\varepsilon_{yy}/dt$ / s⁻¹

Time, *t* / s

Fig. 4.12 (*continued*)

135

(d)

Nominal strain, *e*

CG (early stage of deformation)

$$\frac{\Delta \varepsilon_{yy}}{\Delta t} = 2.2 \times 10^{-4} \, s^{-1}$$

Local strain at analyzed point, ε_{yy}

Local strain rate at analyzed point, $d\varepsilon_{yy}/dt$ / s^{-1}

Time, *t* / s

Nominal strain, *e*

CG (mid stage of deformation)

$$\frac{\Delta \varepsilon_{yy}}{\Delta t} = 1.1 \times 10^{-4} \, s^{-1}$$

Local strain at analyzed point, ε_{yy}

Local strain rate at analyzed point, $d\varepsilon_{yy}/dt$ / s^{-1}

Time, *t* / s

Nominal strain, *e*

CG (late stage of deformation)

$$\frac{\Delta \varepsilon_{yy}}{\Delta t} = 1.0 \times 10^{-4} \, s^{-1}$$

Local strain at analyzed point, ε_{yy}

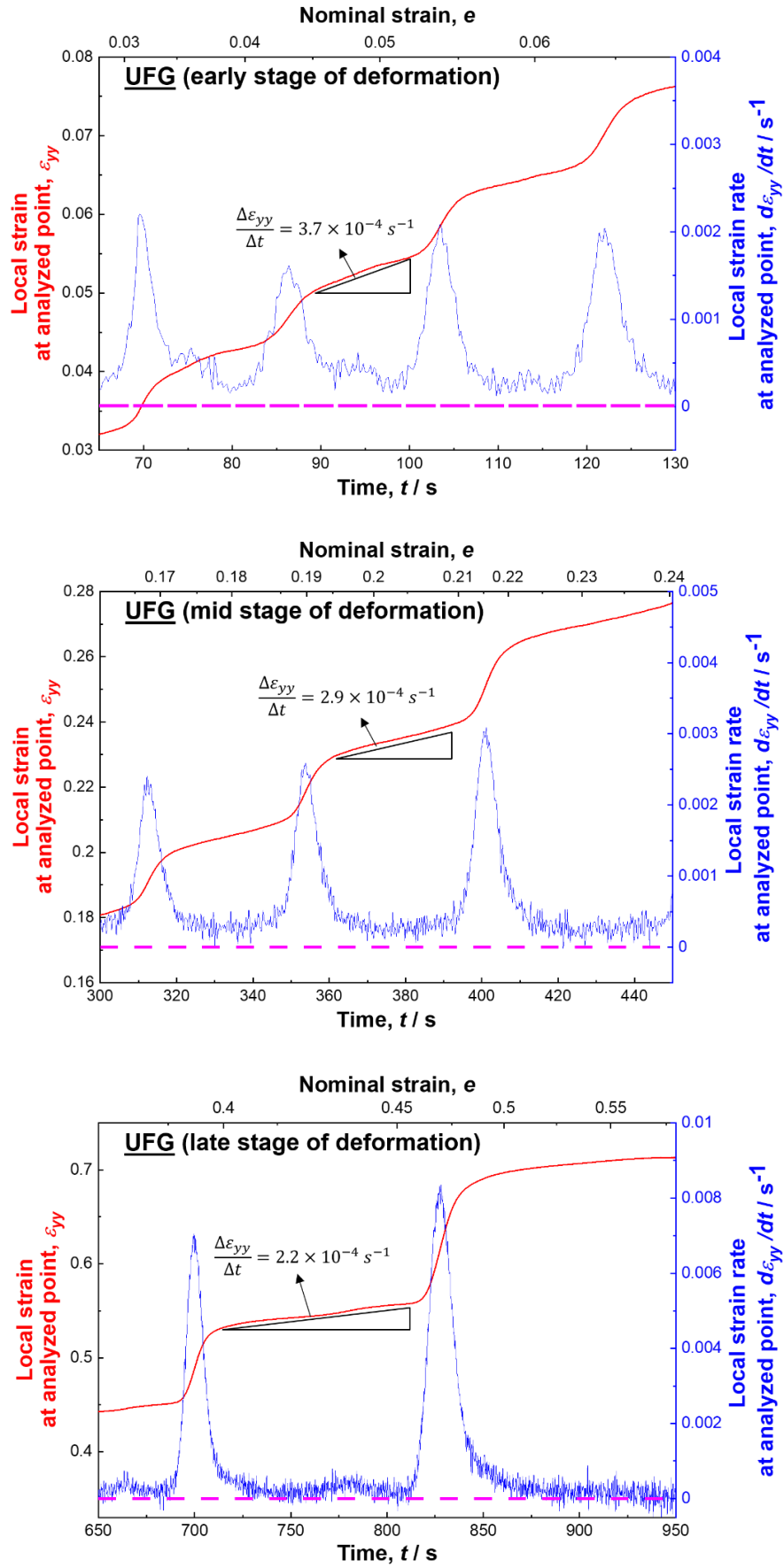Local strain rate at analyzed point, $d\varepsilon_{yy}/dt$ / s^{-1}
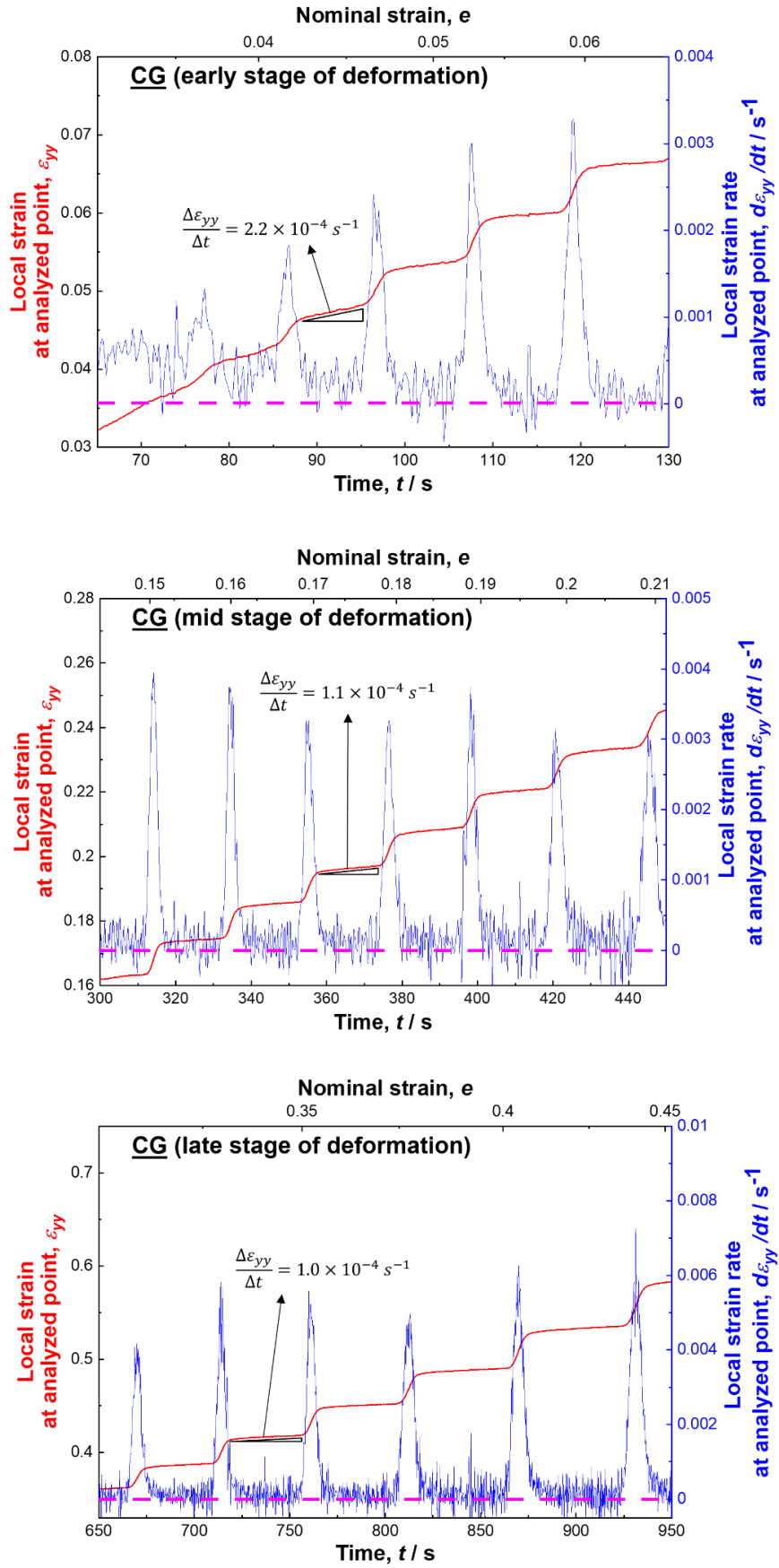
Time, *t* / s

Fig. 4.12 (*continued*)

136

4.4   Conclusion

In this chapter, various grain-sized 22Mn-0.6C steels were fabricated by the repeated cold rolling and subsequent annealing process, and the grain size dependence on the serration behavior was investigated with the aid of DIC technique.   The main results obtained in this chapter are as follows.

1.   After the repeated cold-rolling and subsequent annealing process, the 22Mn-0.6 steel with a fully recrystallized microstructure having a wide range of mean grain sizes from 0. 86 μm to 17 μm was obtained.

2.   With the grain refinement from 17 μm to 0.86 μm, yield strength (0.2% proof stress) increased from 266 MPa to 703 MPa, tensile strength increased from 981 MPa to 1236 MPa, and total elongation decreased from 0.71 to 0.62.   Serration behavior was observed on the stress-strain curves of all the specimens.   The UFG specimen showed a weak serration behavior in the stress-strain curve especially in the early and mid stages of deformation.

3.   The onset strain of serration behavior was investigated on the various grain-sized specimens.   The onset strain of serration behavior (ε_c) was determined by either the first appearance of the serration peak in the stress-strain curves (ε_c^{ss}) or the first appearance of the PLC band (ε_c^{PLC}).   The ε_c (both the ε_c^{ss} and ε_c^{PLC}) decreased with the grain refinement from 17 μm

to 2.0 μm, probably due to the increase of dislocation density.　On the other hand, the ε_c increased steeply with further grain refinement from 1.4 μm to 0.86 μm.　The unique transition of ε_c with the further grain refinement was attributed to the lack of dislocation sources in the grain interior in the UFG region.

4.　　　With the aid of the DIC method, PLC band velocity was investigated for all the specimens over the entire deformation.　The PLC band velocity decreased with the deformation for all the specimens, indicating that more time was needed to accumulate and activate dislocation sources. In addition, the PLC band velocity decreased with the grain refinement.

5.　　　The strain localized in the PLC band increased with deformation, indicating that more strain hardening was achieved within the PLC band for the propagation of the PLC band.　It was also found that the strain localized in the PLC band increased with the grain refinement.　The local strain increment, i.e., strain-hardening, beyond the PLC band was always larger in the UFG specimen than that in the CG specimen at the identical experimental time.　This was because the force difference between the regions within the PLC band and beyond the PLC band became widened with the grain refinement, and it lead to the larger strain localized in the PLC band as well as the slower PLC band velocity.

Chapter 5   Conclusion

In the present thesis, the nature of serration behavior in 22Mn-0.6C steels was systematically investigated with the aid of the *in-situ* DIC technique and the *in-situ* synchrotron XRD measurement during tensile test.   The localized deformation behavior in the form of PLC banding was correlated with the global deformation of the material, and the microscopic DSA was studied in relation to the PLC banding.   Based on the findings related with the PLC banding, grain size dependence on the serration behavior was understood with the aid of the DIC technique.   The results obtained in the present thesis are summarized as follows.

In **Chapter 1**, general use of high-Mn austenitic steel, serration behavior and heterogeneous deformation in high-Mn austenitic steels were introduced, and objective of the present thesis was raised.

In **Chapter 2**, mesoscopic nature of serration behavior in a 22Mn-0.6C steel was clarified with the aid of the *in-situ* DIC technique and the *in-situ* synchrotron XRD measurement during tensile test.   DIC technique during tensile test revealed that serration behavior was the response of the formation, propagation and annihilation of PLC bands (PLC banding) in the tensile specimen. It was clarified that the plastic strain increased drastically only within the PLC band, whereas the plastic strain remained almost constant beyond the PLC band.   The serration peaks corresponded to the suppression of plastic deformation due to the annihilation of PLC band within the gage part. Nucleation of a new PLC band resulted in the quick stress-drop just after the peak.   The *in-situ*

synchrotron XRD measurement at a fixed position during the tensile test revealed that the lattice strain in the X-ray beam position increased at every serration peak, which indicated that the whole specimen was more elastically deformed due to the absence of PLC band within the gage part. The dislocation density suddenly increased when a PLC band was passing through the measurement area because plastic deformation was concentrated and a large number of dislocations were introduced within the PLC band, which corresponded to a drop of the local elastic strain. From the experimentally obtained elastic modulus and elastic strain, local stress at the X-ray beam position was also quantified.   At the late stage of deformation, the stress relaxation within the PLC band was around several megapascals.   The work-hardening by a passage of PLC band reached to 44 ~ 60 MPa, indicating that most of the work-hardening of the present material was achieved by the propagation of PLC bands.   By the repetition of such a cycle of PLC banding (i.e., the nucleation, propagation, and annihilation of PLC bands), plastic deformation of the material gradually proceeded, resulting in the global work-hardening in the present 22Mn-0.6C steel.

In **Chapter 3**, the DSA effect was correlated with the PLC banding, with the aid of the simultaneously applied *in-situ* DIC technique and *in-situ* synchrotron XRD measurement during tensile test.   At the early stage of deformation, the shear strain increased nonlinearly with the dislocation density due to the large MFP of dislocation.   On the other hand, the shear strain increased linearly with the dislocation density at the later stage of deformation due to the small MFP of dislocations.   The average dislocation velocity at the later stage of the deformation was

investigated, considering the PLC band position. The average dislocation velocity beyond the PLC band was in the order of 10^{0} nm/ s, which was much slower than that within the PLC band in the order of 10^{-2} nm/ s. Compared to the dislocation velocity, carbon diffusivity was extremely low that carbon can diffuse only 2.1×10^{-6} nm for 1 second. The obtained results suggested that gliding dislocations became pinned by sweeping the stationary carbons, and such a phenomena was happening beyond the PLC band. On the other hand, dislocations de-pinned again once the local stress sufficiently increased to overcome the pinning by carbons, and such a phenomena was happening within the PLC band. Such localized pinning and de-pinning (the DSA effect) occurred sequentially, and it was shown as the propagation of PLC bands.

In **Chapter 4**, the 22Mn-0.6C steels with the various mean grain sizes ranging from 0.86 μm to 17 μm were fabricated by the repeated cold rolling and subsequent annealing process, and the effect of grain size on the serration behavior was investigated based on the findings in the previous chapters, by using DIC technique. The onset strain of serration behavior (ε_c) was investigated on the various grain-sized specimens. The ε_c was determined by either the first appearance of the serration peak in the stress-strain curves (ε_c^{ss}) or the first appearance of the PLC band (ε_c^{PLC}) in the DIC strain-rate map. The ε_c (both the ε_c^{ss} and ε_c^{PLC}) decreased with the grain refinement from 17 μm to 2.0 μm, probably due to the increase of dislocation density. On the other hand, the ε_c increased steeply with further grain refinement from 1.4 μm to 0.86 μm. The unique transition of ε_c with the further grain refinement was attributed to the lack of

dislocation sources in the grain interior in the UFG region.   However, further studies were necessary to prove the lack of dislocations (or the sources) in the UFG specimens at the early stage of deformation.   With the aid of the DIC method, PLC band velocity was investigated for all the specimens over the entire deformation.   The PLC band velocity of all the specimens decreased as the deformation proceeded, indicating that more time was needed to accumulate and activate dislocations.   Furthermore, the PLC band velocity was found to decrease with the grain refinement. The strain localized in the PLC band increased with deformation, indicating that strain hardening within the PLC band occurred more as the deformation proceeded, for the propagation of the PLC band.   It was also found that the strain localized in the PLC band increased with the grain refinement.   The local strain increment, i.e., the magnitude of the strain-hardening, beyond the PLC band was always larger in the UFG specimen than that in the CG specimen at the identical experimental time.   This was because the force difference between the regions within the PLC band and beyond the PLC band became broadened with the grain refinement, leading to larger strain localization in the PLC band as well as the slower PLC band velocity.

In **Chapter 5**, new findings in the present thesis were concluded.

Acknowledgements

I would like to express my very deepest respect and gratitude to my teacher, Professor Nobuhiro Tsuji, for his excellent scientific guidance, sincere supports and trust through my master and doctoral courses.   I think myself as a very blessed person to be his student, and I would never forget his guidance and trust to me.   I also would like to express my gratitude to my teacher, ESISM assistant professor Myeong-heom Park.   He has kindly taught me fundamental studies in structural materials and guided me to improve myself as a researcher.   I also would like to show my deep gratitude to my teacher, assistant professor Yu Bai.   For past five years, she was always with me even the research did not go well, and patiently guided and helped me.   I also would like to thank to former associate professor Shibata Akinobu, for his strict and sincere guidance.   I am greatly indebted to Ms. Akiko Koike and Ms. Chiaki Ii, for their professional secretarial work, and all my laboratory members for their kind help and support.   At last, I must say thank to my parents and sister, for their constant love and support at all times.

List of publications

1. International journal papers

[1]   S. Hwang, H. Seo, H., Jeong, DC. et al., Growth kinetics of plasma-polymerized films. Sci. Rep. 5, 11201 (2015). https://doi.org/10.1038/srep11201

[2]   S. Hwang, M. Park, Y. Bai, A. Shibata, W. Mao, H. Adachi, M. Sato, and N. Tsuji, Mesoscopic nature of serration behavior in high-Mn austenitic steel, Acta Mater. (2020) In Press. https://doi.org/10.1016/j.actamat.2020.116543

2. International proceeding papers

[1]   S. Hwang, Y. Bai, A. Shibata, and N. Tsuji, Effect of grain size on mechanical properties of silicon-added high-Mn TWIP steel, Proceedings: International symposium on new developments in advanced high-strength sheet steels (AHSS) (2017)

[2]   S. Hwang, Y. Bai, M. Park, A. Shibata, and N. Tsuji, Evaluation of serration behaviors in 22Mn-0.6C steel with various grain sizes, Proceedings: 4th high-Mn steel (HMns) (2019)

3. Presentations in international conference

[1]   S. Hwang, Y. Bai, S. Gao, A. Shibata, and N. Tsuji, Effect of grain size of mechanical properties of silicon-added high-Mn TWIP steel, International symposium on new developments in advanced high-strength sheet steels (AHSS) (2017), Oral presentation

[2]   S. Hwang, Y. Bai, S. Gao, A. Shibata, and N. Tsuji, Microstructure and mechanical properties of 22Mn-3Si-0.6C steel with various grain sizes, The 15th international conference on advanced materials (IUMRS-ICAM) (2017), Poster presentation

[3]   S. Hwang, Y. Bai, S. Gao, A. Shibata, and N. Tsuji, Effect of grain refinement on mechanical properties of Si-added 22Mn-0.6C steel, 18th international conference on the strength of materials (ICSMA 18) (2018), Oral presentation

[4]   S. Hwang, Y. Bai, M. Park, A. Shibata, and N. Tsuji, Evaluation of serration behaviors in 22Mn-0.6C steel with various grain sizes, 4th high-Mn steel (HMns) (2019), Oral presentation

[5]   S. Hwang, M. Park, Y. Bai, A. Shibata, and N. Tsuji, The effect of serration behavior on work hardening and deformation in 22Mn-0.6C steel, Gordon research conferences (GRC) (2019), Poster presentation

[6]   S. Hwang, M. Park, Y. Bai, A. Shibata, and N. Tsuji, Characterization of serration behaviors in 22Mn-0.6C steel, The 10th pacific rim (PRICM) International conference on advanced materials and processing (2019), Oral presentation

[7]   S. Hwang, M. Park, Y. Bai, A. Shibata, and N. Tsuji, Effect of serration on deformation behavior in high-Mn austenitic steel, Materials research meeting (MRM) (2019), Oral presentation

[8]   S. Hwang, M. Park, Y. Bai, A. Shibata, and N. Tsuji, Evaluation of the serration behavior characterized as strain localization in high-Mn austenitic steel, TMS annual meeting and exhibition (2020), Oral presentation

4. Presentations in domestic conference

[1]   S. Hwang, Y. Bai, S. Gao, and N. Tsuji, Microstructure and mechanical properties of 22Mn-3Si-0.6C steel, JIM spring meeting (2017), Poster presentation

[2]   S. Hwang, Y. Bai, S. Gao, A. Shibata, and N. Tsuji, Effect of grain size on mechanical properties of silicon-added high-Mn TWIP steel, ISIJ fall meeting (2017), Oral presentation

[3]   S. Hwang, Y. Bai, M. Park, A. Shibata, and N. Tsuji, Effect of grain refinement on serration behavior in 22Mn-0.6C austenitic steel, ISIJ fall meeting (2018), Poster presentation

[4]   S. Hwang, M. Park, Y. Bai, A. Shibata, H. Adachi, and N. Tsuji, Evaluation of serration behaviors in 22Mn-0.6C steel with various grain sizes, ISIJ spring meeting (2019), Oral presentation

[5]   <u>S. Hwang</u>, M. Park, Y. Bai, A. Shibata, H. Adachi, and N. Tsuji, Understanding serration behavior in high-Mn austenitic steel from a view point of work hardening and plastic deformation, ISIJ fall meeting (2019), Oral presentation

5. Award

[1]   Award for encouragement of research, The 15th international conference on advanced materials (IUMRS-ICAM) (2017)

[2]   Student poster award, ISIJ fall meeting (2018)

References

[1]   O. Grässel, L. Krüger, G. Frommeyer, L.W. Meyer, High strength Fe-Mn-(Al, Si) TRIP/TWIP steels development - properties - application, Int. J. Plast. 16 (2000) 1391–1409. doi:10.1016/S0749-6419(00)00015-2.

[2]   D.R. Steinmetz, T. Jäpel, B. Wietbrock, P. Eisenlohr, I. Gutierrez-Urrutia, A. Saeed-Akbari, T. Hickel, F. Roters, D. Raabe, Revealing the strain-hardening behavior of twinning-induced plasticity steels: Theory, simulations, experiments, Acta Mater. (2013). doi:10.1016/j.actamat.2012.09.064.

[3]   S. Allain, J.P. Chateau, O. Bouaziz, S. Migot, N. Guelton, Correlations between the calculated stacking fault energy and the plasticity mechanisms in Fe-Mn-C alloys, Mater. Sci. Eng. A. 387–389 (2004) 158–162. doi:10.1016/j.msea.2004.01.059.

[4]   A. Dumay, J.P. Chateau, S. Allain, S. Migot, O. Bouaziz, Influence of addition elements on the stacking-fault energy and mechanical properties of an austenitic Fe-Mn-C steel, Mater. Sci. Eng. A. 483–484 (2008) 184–187. doi:10.1016/j.msea.2006.12.170.

[5]   B.C. De Cooman, Y. Estrin, S.K. Kim, Twinning-induced plasticity (TWIP) steels, Acta Mater. (2018). doi:10.1016/j.actamat.2017.06.046.

[6]   O. Bouaziz, S. Allain, C.P. Scott, P. Cugy, D. Barbier, High manganese austenitic twinning induced plasticity steels: A review of the microstructure properties relationships, Curr. Opin. Solid State Mater. Sci. (2011). doi:10.1016/j.cossms.2011.04.002.

[7]   A. van den Beukel, Theory of the effect of dynamic strain aging on mechanical properties, Phys. Status Solidi. (1975). doi:10.1002/pssa.2210300120.

[8]   D. Caillard, Dynamic strain ageing in iron alloys: The shielding effect of carbon, Acta Mater. (2016). doi:10.1016/j.actamat.2016.04.018.

[9]   I.E. Dolzhenkov, The nature of blue brittleness of steel, Met. Sci. Heat Treat. (1971). doi:10.1007/BF00652795.

[10]   A.H. Cottrell, LXXXVI. A note on the Portevin-Le Chatelier effect, London, Edinburgh, Dublin Philos. Mag. J. Sci. (1953). doi:10.1080/14786440808520347.

[11]   A. Yilmaz, The Portevin-Le Chatelier effect: A review of experimental findings, Sci. Technol. Adv. Mater. (2011). doi:10.1088/1468-6996/12/6/063001.

[12]   Z.C. Luo, M.X. Huang, Revisit the role of deformation twins on the work-hardening behaviour of twinning-induced plasticity steels, Scr. Mater. (2018). doi:10.1016/j.scriptamat.2017.08.017.

[13]   K. Renard, S. Ryelandt, P.J. Jacques, Characterisation of the Portevin-Le Châtelier effect affecting an austenitic TWIP steel based on digital image correlation, Mater. Sci. Eng. A. (2010). doi:10.1016/j.msea.2010.01.037.

[14]   A. Saeed-Akbari, A.K. Mishra, J. Mayer, W. Bleck, Characterization and prediction of flow behavior in high-manganese twinning induced plasticity steels: Part II. jerky flow and instantaneous strain rate, Metall. Mater. Trans. A Phys. Metall. Mater. Sci. (2012).

doi:10.1007/s11661-011-1070-8.

[15]   M. Koyama, E. Akiyama, K. Tsuzaki, Factors Affecting Static Strain Aging Under Stress at Room Temperature in a Fe-Mn-C Twinning-Induced Plasticity Steel, Tetsu-to-Hagane. (2014). doi:10.2355/tetsutohagane.100.1123.

[16]   S.Y. Lee, S.I. Lee, B. Hwang, Effect of strain rate on tensile and serration behaviors of an austenitic Fe-22Mn-0.7C twinning-induced plasticity steel, Mater. Sci. Eng. A. (2018). doi:10.1016/j.msea.2017.10.074.

[17]   Z.Y. Liang, X. Wang, W. Huang, M.X. Huang, Strain rate sensitivity and evolution of dislocations and twins in a twinning-induced plasticity steel, Acta Mater. (2015). doi:10.1016/j.actamat.2015.01.013.

[18]   Y. Estrin, L.P. Kubin, Local strain hardening and nonuniformity of plastic deformation, Acta Metall. (1986). doi:10.1016/0001-6160(86)90148-3.

[19]   M. Koyama, T. Sawaguchi, K. Tsuzaki, Deformation Twinning Behavior of Twinning-induced Plasticity Steels with Different Carbon Concentrations – Part 2: Proposal of Dynamic-strain-aging-assisted Deformation Twinning, ISIJ Int. (2015). doi:10.2355/isijinternational.isijint-2015-070.

[20]   S.J. Lee, J. Han, S. Lee, S.H. Kang, S.M. Lee, Y.K. Lee, Design for Fe-high Mn alloy with an improved combination of strength and ductility, Sci. Rep. (2017). doi:10.1038/s41598-017-03862-y.

[21]   S.J. Lee, J. Kim, S.N. Kane, B.C. De Cooman, On the origin of dynamic strain aging in twinning-induced plasticity steels, Acta Mater. (2011). doi:10.1016/j.actamat.2011.07.040.

[22]   L. Chen, H.-S. Kim, S.-K. Kim, B.C. De Cooman, Localized Deformation due to Portevin–LeChatelier Effect in 18Mn–0.6C TWIP Austenitic Steel, ISIJ Int. (2007). doi:10.2355/isijinternational.47.1804.

[23]   D. Canadinc, C. Efstathiou, H. Sehitoglu, On the negative strain rate sensitivity of Hadfield steel, Scr. Mater. (2008). doi:10.1016/j.scriptamat.2008.07.027.

[24]   X. Bian, F. Yuan, X. Wu, Correlation between strain rate sensitivity and characteristics of Portevin-LeChátelier bands in a twinning-induced plasticity steel, Mater. Sci. Eng. A. (2017). doi:10.1016/j.msea.2017.04.078.

[25]   M. Eskandari, M.R. Yadegari-Dehnavi, A. Zarei-Hanzaki, M.A. Mohtadi-Bonab, R. Basu, J.A. Szpunar, In-situ strain localization analysis in low density transformation-twinning induced plasticity steel using digital image correlation, Opt. Lasers Eng. (2015). doi:10.1016/j.optlaseng.2014.10.005.

[26]   H. Halim, D.S. Wilkinson, M. Niewczas, The Portevin-Le Chatelier (PLC) effect and shear band formation in an AA5754 alloy, Acta Mater. (2007). doi:10.1016/j.actamat.2007.03.007.

[27]   S. Gao, Y. Bai, R. Zheng, Y. Tian, W. Mao, A. Shibata, N. Tsuji, Mechanism of huge Lüders-type deformation in ultrafine grained austenitic stainless steel, Scr. Mater. (2019).

doi:10.1016/j.scriptamat.2018.09.007.

[28]   H. Adachi, Y. Miyajima, M. Sato, N. Tsuji, Evaluation of dislocation density for 1100

aluminum with different grain size during tensile deformation by using In-situ X-ray diffraction

technique, J. Japan Inst. Light Met. (2014). doi:10.2464/jilm.64.463.

[29]   M. Zhang, R. Li, J. Ding, H. Chen, J.S. Park, J. Almer, Y.D. Wang, In situ high-energy

X-ray diffraction mapping of Lüders band propagation in medium-Mn transformation-induced

plasticity steels, Mater. Res. Lett. (2018). doi:10.1080/21663831.2018.1530698.

[30]   Y.Z. Tian, Y. Bai, M.C. Chen, A. Shibata, D. Terada, N. Tsuji, Enhanced Strength

and Ductility in an Ultrafine-Grained Fe-22Mn-0.6C Austenitic Steel Having Fully

Recrystallized Structure, Metall. Mater. Trans. A Phys. Metall. Mater. Sci. 45 (2014) 5300–

5304. doi:10.1007/s11661-014-2552-2.

[31]   N. Tsuji, S. Ogata, H. Inui, I. Tanaka, K. Kishida, S. Gao, W. Mao, Y. Bai, R. Zheng,

J.-P. Du, Strategy for managing both high strength and large ductility in structural materials–

sequential nucleation of different deformation modes based on a concept of plaston, Scr. Mater.

181 (2020) 35–42. doi:https://doi.org/10.1016/j.scriptamat.2020.02.001.

[32]   W.Q. Mao, S. Gao, W. Gong, M.H. Park, Y. Bai, A. Shibata, N. Tsuji, Influence of

Grain Size on Work-Hardening Behavior of Fe-24Ni-0.3C Metastable Austenitic Steel, in:

2018. doi:10.1007/978-3-319-76968-4_15.

[33]   B. Wang, X. Huang, A. Fu, Y. Liu, B. Liu, Serration behavior and microstructure of

high entropy alloy CoCrFeMnNi prepared by powder metallurgy, Mater. Sci. Eng. A. (2018). doi:10.1016/j.msea.2018.04.071.

[34]   W. Charnock, The influence of grain size on the nature of Portevin-Lechatelier Yielding, Philos. Mag. (1968). doi:10.1080/14786436808227311.

[35]   B.H. Lee, S.H. Kim, J.H. Park, H.W. Kim, J.C. Lee, Role of Mg in simultaneously improving the strength and ductility of Al-Mg alloys, Mater. Sci. Eng. A. (2016). doi:10.1016/j.msea.2016.01.089.

[36]   M. Wagenhofer, M. Erickson-Natishan, R.W. Armstrong, F.J. Zerilli, Influences of strain rate and grain size on yield and serrated flow in commercial Al-Mg alloy 5086, Scr. Mater. (1999). doi:10.1016/S1359-6462(99)00265-1.

[37]   H. Zhi, C. Zhang, S. Antonov, H. Yu, T. Guo, Y. Su, Investigations of dislocation-type evolution and strain hardening during mechanical twinning in Fe-22Mn-0.6C twinning-induced plasticity steel, Acta Mater. (2020). doi:10.1016/j.actamat.2020.05.062.

[38]   T.H. Simm, Peak broadening anisotropy and the contrast factor in metal alloys, Crystals. (2018). doi:10.3390/cryst8050212.

[39]   L. Balogh, G. Ribárik, T. Ungár, Stacking faults and twin boundaries in fcc crystals determined by x-ray diffraction profile analysis, J. Appl. Phys. (2006). doi:10.1063/1.2216195.

[40]   G.K. Williamson, W.H. Hall, X-Ray broadening from filed aluminium and tungsten, Acta Metall. (1953).

[41]   R. Ueji, N. Tsuchida, D. Terada, N. Tsuji, Y. Tanaka, A. Takemura, K. Kunishige, Tensile properties and twinning behavior of high manganese austenitic steel with fine-grained structure, Scr. Mater. (2008). doi:10.1016/j.scriptamat.2008.06.050.

[42]   H.Y. Yu, S.M. Lee, J.H. Nam, S.J. Lee, D. Fabrègue, M. heom Park, N. Tsuji, Y.K. Lee, Post-uniform elongation and tensile fracture mechanisms of Fe-18Mn-0.6C-xAl twinning-induced plasticity steels, Acta Mater. (2017). doi:10.1016/j.actamat.2017.04.011.

[43]   S.K. Oh, M.E. Kilic, J.B. Seol, J.S. Hong, A. Soon, Y.K. Lee, The mechanism of dynamic strain aging for type A serrations in tensile flow curves of Fe-18Mn-0.55C (wt.%) twinning-induced plasticity steel, Acta Mater. (2020). doi:10.1016/j.actamat.2020.02.020.

[44]   W.G. Johnston, J.J. Gilman, Dislocation velocities, dislocation densities, and plastic flow in lithium fluoride crystals, J. Appl. Phys. (1959). doi:10.1063/1.1735121.

[45]   D. Hull, D.J. Bacon, Introduction to Dislocations, 2011. doi:10.1016/C2009-0-64358-0.

[46]   L. Král, B. Million, J. Čermák, Diffusion of Carbon and Manganese in Fe-C-Mn, Defect Diffus. Forum. (2007). doi:10.4028/www.scientific.net/ddf.263.153.

[47]   E.O. Hall, The deformation and ageing of mild steel: III Discussion of results, Proc. Phys. Soc. Sect. B. 64 (1951) 747–753. doi:10.1088/0370-1301/64/9/303.

[48]   N.J. Petch, The cleavage strength of polycrystals, J. Iron Steel InstInst. 174 (1953) 25–28. doi:10.1007/BF01972547.

[49]   S.Y. Jo, J. Han, J.H. Kang, S. Kang, S. Lee, Y.K. Lee, Relationship between grain size and ductile-to-brittle transition at room temperature in Fe-18Mn-0.6C-1.5Si twinning-induced plasticity steel, J. Alloys Compd. 627 (2015) 374–382. doi:10.1016/j.jallcom.2014.11.232.

[50]   Y.Z. Tian, Y. Bai, L.J. Zhao, S. Gao, H.K. Yang, A. Shibata, Z.F. Zhang, N. Tsuji, A novel ultrafine-grained Fe–22Mn–0.6C TWIP steel with superior strength and ductility, Mater. Charact. 126 (2017) 74–80. doi:10.1016/j.matchar.2016.12.026.

[51]   P.G. Mccormick, Effect of grain size on serrated yielding in an Al-Mg-Si alloy, Philos. Mag. A J. Theor. Exp. Appl. Phys. 23 (1971) 949–956. doi:10.1080/14786437108216997.

[52]   M. Koyama, T. Sawaguchi, K. Tsuzaki, Inverse grain size dependence of critical strain for serrated flow in a Fe-Mn-C twinning-induced plasticity steel, Philos. Mag. Lett. (2012). doi:10.1080/09500839.2011.640645.

[53]   Y. Nakada, A.S. Keh, Serrated flow in Ni-C alloys, Acta Metall. (1970). doi:10.1016/0001-6160(70)90129-X.

[54]   F. Yang, H. Luo, E. Pu, S. Zhang, H. Dong, On the characteristics of Portevin–Le Chatelier bands in cold-rolled 7Mn steel showing transformation-induced plasticity, Int. J. Plast. (2018). doi:10.1016/j.ijplas.2018.01.010.

[55]   T. Narutani, J. Takamura, Grain-size strengthening in terms of dislocation density measured by resistivity, Acta Metall. Mater. (1991). doi:10.1016/0956-7151(91)90173-X.

[56]   H. Kitamura, Y. Bai, Y. Tian, A. Shibata, N. Tsuji, Deformation mechanism of

ultrafine-grained high-Mn austenitic TWO∗ steel, in: Int. Symp. New Dev. Adv. High-Strength

Sheet Steels, 2017.

[57]   Y.Z. Tian, S. Gao, L.J. Zhao, S. Lu, R. Pippan, Z.F. Zhang, N. Tsuji, Remarkable

transitions of yield behavior and Lüders deformation in pure Cu by changing grain sizes, Scr.

Mater. (2018). doi:10.1016/j.scriptamat.2017.08.034.